Universitätsklinikum Hamburg-Eppendorf

Institute of Neuropathpology

Molecular analysis of Small Vessel Disease in Familial Alzheimer's Disease

Presented by:

Jessica Lisa Littau

Dissertation submitted to the
Universität Hamburg – Fachbereich Biologie

Hamburg 2024

Gutachter:

Prüfungsausschuss, der/die Vorsitzende: Prof. Dr. Markus Glatzel

Prüfungsausschuss, 2. Gutachter/in: Prof. Dr. Christian Lohr

Datum der Disputation: 02.10.2024

Dedication

To Leguminosa, Nelson and my family.

Acknowledgments

I would like to thank my supervisor and sponsor of my thesis, Diego Sepulveda-Falla for training and guiding me successfully through the PhD. I would like to thank my supervisors Markus Glatzel and Christian Lohr for supporting and guiding me. I would like to express my gratitude to Rajesh Kalaria for training me in grading vascular pathology which was the basis for my whole thesis. Next, I would like to thank Nelson David Villalba Moreno for his input and guidance, Yassir El Hamdani El Amri and Mohsin Shafiq for the help with the proteomic analyses, and all the kind colleagues of the Institute for Neuropathology for all the support, guidance, and help in the laboratory. Finally, I'd like to express my gratitude to Mark Ellisman and Keunyoung Kim for the collaboration on the mouse serial EM data.

Abstract

Alzheimer's disease (AD) neuropathological hallmarks include the presence of amyloid plaques, neurofibrillary tangles, and other unspecific neurodegenerative changes. Brain vascular pathology in AD has been typically attributed to intramural Amyloid beta (Aβ) deposition. A deeper characterization of vascular pathology in AD was warranted given recent findings highlighting the multifactorial nature of this disorder. The impact of small vessel disease on disease progression was evaluated in familial Alzheimer's disease (FAD), carrying the *PSEN1* E280A mutation. Various histological methods, proteomics analyses and electron microscopy (EM) were used to gain insight into vascular pathology and its association with Aβ and tau deposits. There were no differences in cerebral amyloid angiopathy pathology between FAD and sporadic Alzheimer's disease (SAD). Yet, FAD presented with mural cell pathology and reduced coverage of astrocyte end-feet around vessels. Thus, suggesting the vascular pathology observed in FAD to be Aβ independent. Proteomic analyses revealed distinct pathways to be differently affected in the frontal or occipital cortex in FAD when compared to healthy controls and SAD. Alterations in basement membrane (BM) such as BM thickening, collagen IV deposits and glypican-5 deposits were observed. In fact, tau pathology was present to a higher degree in FAD as shown by the presence of different phosphosites and higher predicted kinase activity. Immunofluorescence analysis of different phosphosites revealed distinct differences between FAD and SAD. FAD presented with less AT8 immunoreactivity and less density than SAD while FAD had a higher density than SAD for Thr231 and Thr217. Finally, a *PSEN1* knock-in mouse model was used carrying the E280A mutation to evaluate early changes caused by the E280A mutation without the presence of protein deposits. These mice presented with more tortuous vessels, abnormal thickening, branching and duplication of the BM. Ultrastructural analyses showed lamellar bodies in the astrocyte end-feet with a higher number and higher area covered of the end-feet. Taken together, the findings indicate different simultaneous mechanism leading to small vessel disease in FAD patients. Further analyses in a murine model indicate that vascular alterations are early changes caused by the *PSEN1* E280A mutation proceeding Aβ and tau deposits. Evidence of astrocytic dysfunction was found in both approaches, suggesting *PSEN1* mutation-dependent dysfunction of the neurovascular unit in FAD.

Zusammenfassung

Die neuropathologischen Merkmale der Alzheimer Krankheit (AK) umfassen die Präsenz von Amyloid-Plaques, neurofibrillären Knäueln und anderen unspezifische Veränderungen. Die vaskulären Pathologien in der AK werden in der Regel auf intramurale Ablagerungen von beta-Amyloid-Peptiden (Aβ) zurückgeführt. Eine detailliertere Untersuchung der vaskulären Pathologie in der AK war angesichts der jüngsten Erkenntnisse, die den multifaktoriellen Charakter der Erkrankung unterstreichen, gerechtfertigt. Der Einfluss der Erkrankung kleiner Gefäße auf das Fortschreiten der Krankheit wurde bei der familiären AK (FAK) untersucht, welche die *PSEN1* E280A-Mutation trägt. Verschiedene histologische Methoden, proteomische Analysen und Elektronenmikroskopie (EM) wurden eingesetzt, um Einblicke in die vaskuläre Pathologie und deren Zusammenhang mit Aβ und Tau-Ablagerungen zu gewinnen. Es gab keine Unterschiede in der zerebralen Amyloidangiopathie zwischen FAK und sporadischer Alzheimer Krankheit (SAK). Allerdings wies FAK eine Pathologie der Wandzellen auf und eine geringere Abdeckung der Gefäße mit Endfüßen der Astrozyten. Dies deutet darauf hin, dass die bei FAK beobachtete Gefäßpathologie unabhängig von Aβ ist. Proteomanalysen ergaben, dass bei FAK im frontalen und okzipitalen Kortex verschiedene Signalwege im Vergleich zu den gesunden Kontrollen und SAK unterschiedlich betroffen sind. Es wurden Veränderungen in der Form von einer Basalmembran-Verdickung, Kollagen-IV-Ablagerungen und Glypican-5-Ablagerungen beobachtet. Die Tau-Pathologie war bei FAK in einem höheren Maße präsent, welches durch das Vorhandensein verschiedener Phosphositen und einer höheren vorhergesagten Kinaseaktivität erklärt werden kann. Die Immunofluoreszenz-Analyse der verschiedenen Phosphositen ergab deutliche Unterschiede zwischen FAK und SAK. FAK wies eine geringere AT8-Immunoreaktivität und eine geringere Dichte als SAK auf und eine höhere Dichte für Thr231 und Thr217 als SAD. Schließlich wurde ein *PSEN1*-knock-in-Mausmodell mit der E280A-Mutation verwendet, um die durch die E280A-Mutation verursachten Veränderungen ohne die Anwesenheit von Proteinablagerungen zu untersuchen. Diese Mäuse wiesen mehr gewundene Gefäße, abnorme Verdickungen, Verzweigungen und Verdopplungen der BM auf. Ultrastrukturelle Analysen zeigten außerdem lamellare Körper in den Endfüßchen von Astrozyten mit einer höheren Anzahl und einer größeren Fläche. Zusammengenommen deuten die Ergebnisse auf verschiedene simultane Mechanismen hin, die bei FAK-Patienten zu einer Erkrankung der kleinen Gefäßen führen. Weitere Analysen in einem Mausmodell deuten darauf

hin, dass es sich bei den vaskulären Veränderungen um eine frühe Veränderung handelt, die durch die *PSEN1* E280A-Mutation verursacht werden, die Aβ und Tau-Ablagerungen vorausgeht. Bei den Ansätzen wurden Hinweise auf eine astrozytäre Dysfunktion gefunden, was auf eine von der *PSEN1*-Mutation abhängige Dysfunktion der neurovaskulären Einheit bei FAK hindeutet.

Table of Contents

1. Introduction

Alzheimer's disease (AD) is the most prevalent neurodegenerative dementia with approximately 46 million affected people worldwide[1]. AD was first described in 1906 by Alois Alzheimer. He described senile plaques and neurofibrillary tangles in the brain of his patient Auguste D. She previously presented with an unusual mental illness 4.5 years prior to her death at 51 years of age with symptoms including disorientation, cognitive disturbance, delusions, and other behavioural changes[2]. Nowadays, the presence of Aβ plaques and hyperphosphorylated tau deposits are required for an AD diagnosis. For the following decades after Alzheimer's original description, the research was focused on the protein aggregates first described histologically by Alzheimer and others. AD was characterised by the presence of Aβ plaques in the extracellular space, neurofibrillary tangles (NFTs) in the intracellular space, and cerebral amyloid angiopathy (CAA), seen as Aβ deposits in the walls of small vessels, together with gliosis and other unspecific degenerative changes. For diagnostic purposes, the extent of AD pathology is evaluated by semi-quantitative scales, such as the Braak stages published in 1991. A case is classified as Braak stage I or II when the tau pathology is limited to the transentorhinal region, stages III and IV include involvement of the limbic regions, and V and VI include extensive neocortical involvement[3,4]. Several physiopathological processes contribute to the development of AD such as the accumulation of misfolded proteins, Aβ and tau, neuroinflammation, cholinergic deficiency and cerebral vascular dysfunction (Fig. 1).

1.1 Aβ pathology

By using whole genome sequencing different genes have been identified either increasing the risk for AD or directly causing it. In the mid-1980s, ultrastructural studies of Aβ and the sequence of Aβ as the main component of the plaques led to the identification of amyloid precursor protein (*APP*). Later, two pathways of processing for Aβ were identified: the non-amyloidogenic and amyloidogenic pathways (Fig. 2).

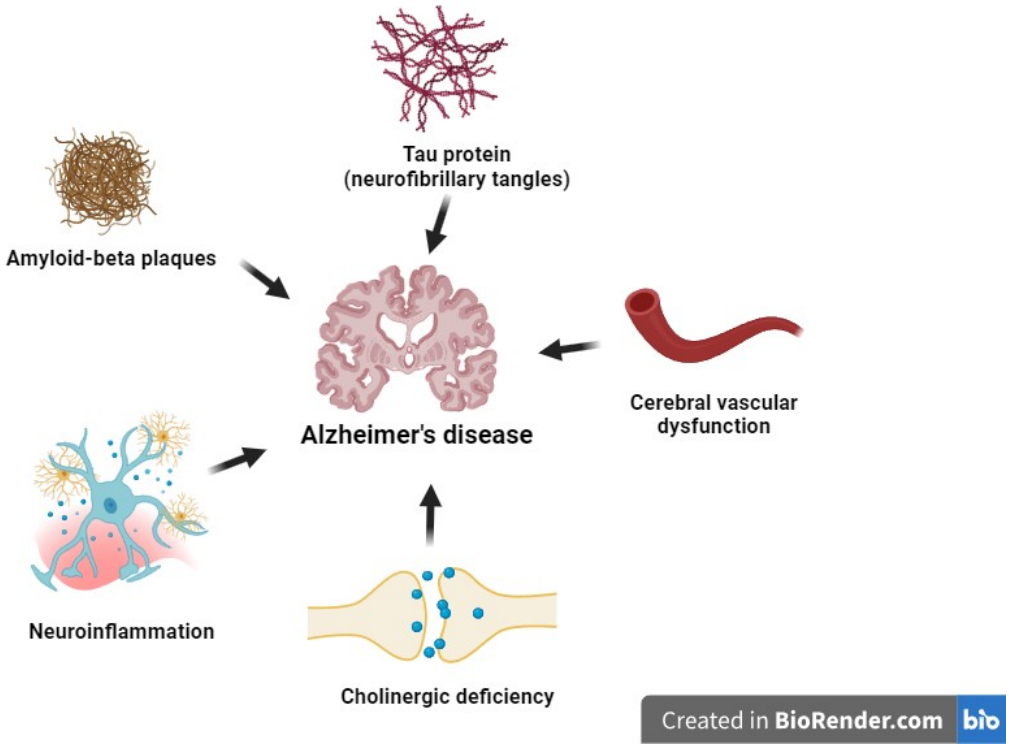

Figure 1: Physiopathologic processes contributing to the development of AD. *Protein aggregates in the form of tau and Aβ, as well as neuroinflammation, cerebral vascular dysfunction and cholinergic deficiency, contribute to the progression of AD.*

In the non-amyloidogenic pathway, APP is cleaved by the α-secretase within the Aβ domain releasing the soluble APP (sAPPα) fragment. The C-terminal fragment (CTF) is cleaved by the γ-secretase releasing the p3 peptide while the remaining APP intracellular domain (AICD) is metabolised in the cytoplasm. In this pathway, the cleavage of APP does not result in the generation of Aβ fragments, as APP is cleaved within the Aβ domain. In the amyloidogenic pathway, APP is cleaved by the β-secretase. This cleavage takes place upstream the Aβ domain, thus, releasing the soluble sAPPβ. The CTF is cleaved by the γ-secretase complex releasing free 40 or 42 amino acid long Aβ peptide. As with the non-amyloidogenic pathway, the AICD is metabolised in the cytoplasm[5] (Fig. 2).

The γ-secretase consists of Nicastrin, Presenilin Enhancer 2 (PEN-2), Anterior PHarynx defective 1 homolog (APH1), and Presenilin-1 (PS1) or Presenilin-2 (PS2) which are the catalytic unit of the γ-secretase[6,7]. The current dominant hypothesis for the cause of AD is the amyloid cascade hypothesis, postulating an imbalance between Aβ clearance and production

with increased production of Aβ42 in FAD and reduced clearance in SAD. Subsequent aggrega-aggregation of Aβ peptides leads to their deposition, increasing oxidative and inflammatory stress, thereby impairing neuronal and synaptic function[5]. Generally, it is postulated that the distribution of Aβ deposition across the brain follows an anterograde pattern into regions that receive neuronal projections from regions already affected by Aβ pathology. Thal staging is used to describe the stages of Aβ deposition. During phase 1, Aβ deposits can be found in the frontal, temporal, parietal, or occipital neocortex in small groups of diffuse plaques in layers II-V. Next, the entorhinal region, CA1, and the insular cortex are affected during phase 2. Thereafter, in phase 3, Aβ plaques occur in the diencephalic nuclei, the striatum, and the cholinergic nuclei of the basal forebrain. In phase 4 more Aβ deposits can be found in the inferior olivary nucleus, the reticular formation of the medulla oblongata, and the substantia nigra. Additionally, CA4, the superior and inferior colliculi, and the red nucleus consistently present with Aβ plaques during phase 4. During phase 5, the cerebellum becomes involved and presents with Aβ deposits[8].

In addition, Aβ deposits building up in the media and adventitia of small and medium calibre cerebral arterial vessels and venous vessels of the cerebral cortex and pia mater are referred to as cerebral amyloid angiopathy (CAA). Approximately, 80% of AD patients are affected by CAA as well[9]. CAA is also detrimental in AD, because it causes vessel wall stiffness making vessels vulnerable to rupture or aneurysms formation. CAA has been shown to cause changes in the morphology of vascular cells and basement membrane composition. Aβ deposits had been linked to mural cell degeneration and abnormal thickening of capillary basement membranes[10]. The thickening was associated with increased expression of collagen IV, fibronectin, agrin, and perlecan[11].

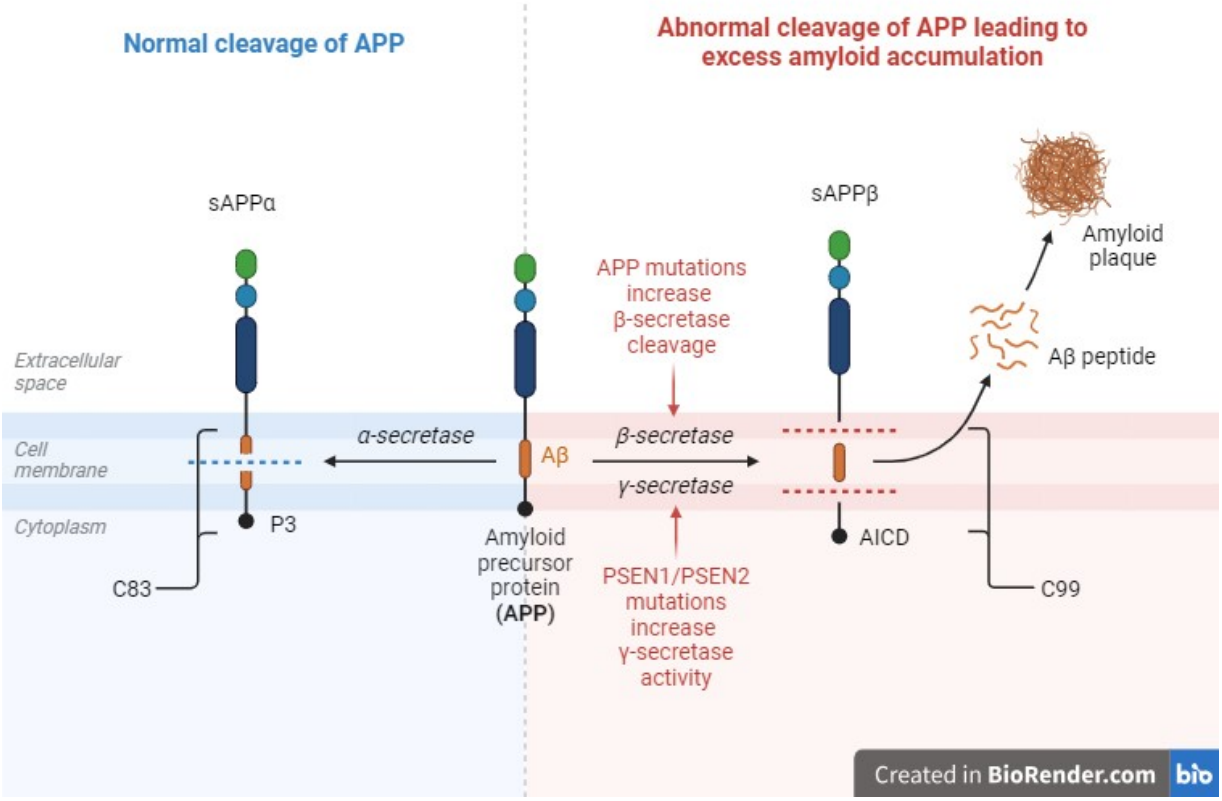

Figure 2: Amyloidogenic pathway. *The α-secretase cleavage of APP (non-amyloidogenic pathway) is shown on the left, while cleavage by the β- and γ-secretase (amyloidogenic pathway) is shown on the right. In FAD, mutations in PSEN1 or PSEN2 increase γ-secretase activity, resulting in more Aβ being released into the extracellular space.*

1.2 Tau

AD patients present with tau aggregates in the form of tangles: pre-tangles, mature tangles and ghost tangles and neuritic pathology: neuropil threads, neuritic plaques and tangle-associated neuritic clusters, making AD a prototypical tauopathy. However, since Aβ is considered necessary to drive neurodegeneration in AD, it is considered a secondary tauopathy and not a primary one. Tauopathies are neurodegenerative disorders characterized by abnormal tau deposits in the brain[12]. There are six isoforms of tau which are derived from the differential splicing of exons of the microtubule-associated protein tau (MAPT) gene on chromosome 17q21[13]. Tau has an amino (N) and carboxyl (C) terminal end, a central proline-rich domain, and a repeat domain, with either three or four repeats (3R or 4R) and differing numbers of N-terminal inserts (0 N, 1 N, or 2 N). The repeat domains are crucial for regulating microtubule stability and axonal transport. Under normal conditions, tau is a "natively unfolded" protein with a low tendency for misfolding or self-aggregation. Tau function is regulated by post-translational

modifications (PTM), namely phosphorylation, dephosphorylation, acetylation, glycation, or ubiquitination. Phosphorylation and dephosphorylation are modified by protein kinases including glycogen synthase kinase-3 (GSK3), cyclin-dependent kinase-5 (cdk5), or C-Jun amino-terminal kinase (JNK). Tau contains 85 potential serine (S), threonine (T), and tyrosine (Y) phosphorylation sites, most of which can be found in the proline-rich domain of tau[14]. It has been shown that phosphorylation of Ser262 or Ser214 leads to the detachment of tau from microtubules[15]. An increase of phosphorylation leads to more self-aggregated and hyperphosphorylated tau which alters the conformation and charge of the tau protein. Causing the microtubule-binding domain to be exposed allowing for self-aggregation and oligomerisation of tau up to the formation of neurofibrillary tangles (NFTs). Further, paired helical filaments (PHFs) are assembled due to hyperphosphorylation of the c-terminus inducing self-assembly of tau. Taken together, aggregation of tau leads to the loss of axonal transport and paves the way for microtubule destabilization[16] (Fig. 3). Previously, Wesseling et al. showed different phosphorylations of tau to be associated with disease progression. They demonstrated that increasing phosphorylations in the proline-rich-region were followed by acetylation and ubiquitination in the microtubule-binding region[17].

Tau aggregates in the brain can be visualised immunohistochemically with different antibodies, but not all recognise all their maturity levels. There are different stages of tau aggregation that can be found in the brain which can be visualised immunohistochemically from pre-tangle to ghost tangle. Small granular accumulations deposit outside the nucleus of the neuron turn into pre-tangles. Once the granular accumulations turn into fibres that fill the neuron it then develops into a mature tangle, also known as neurofibrillary tangles (NFTs). These then displace and shrink the nuclei until the neuron dies and only the tau fibres remain as a ghost tangle (Fig. 4)[4]. The different stages of tau tangles do not only differ in their morphology but their post-translational modifications and tau isoform predilection. On the other hand, the neuritic pathologies affect the processes of the neurons in contrast to the soma and include neuropil threads, neuritic plaques, and tangle-associated neuritic clusters (TANCs) (Fig. 4). Primarily, these consist of PHFs and straight filaments replacing neurofilament in the neurites[18]. Bulbous and thread-like dystrophic neurites alongside extracellular Aβ deposits build neuritic plaques which commonly form around the microvasculature[19–21].

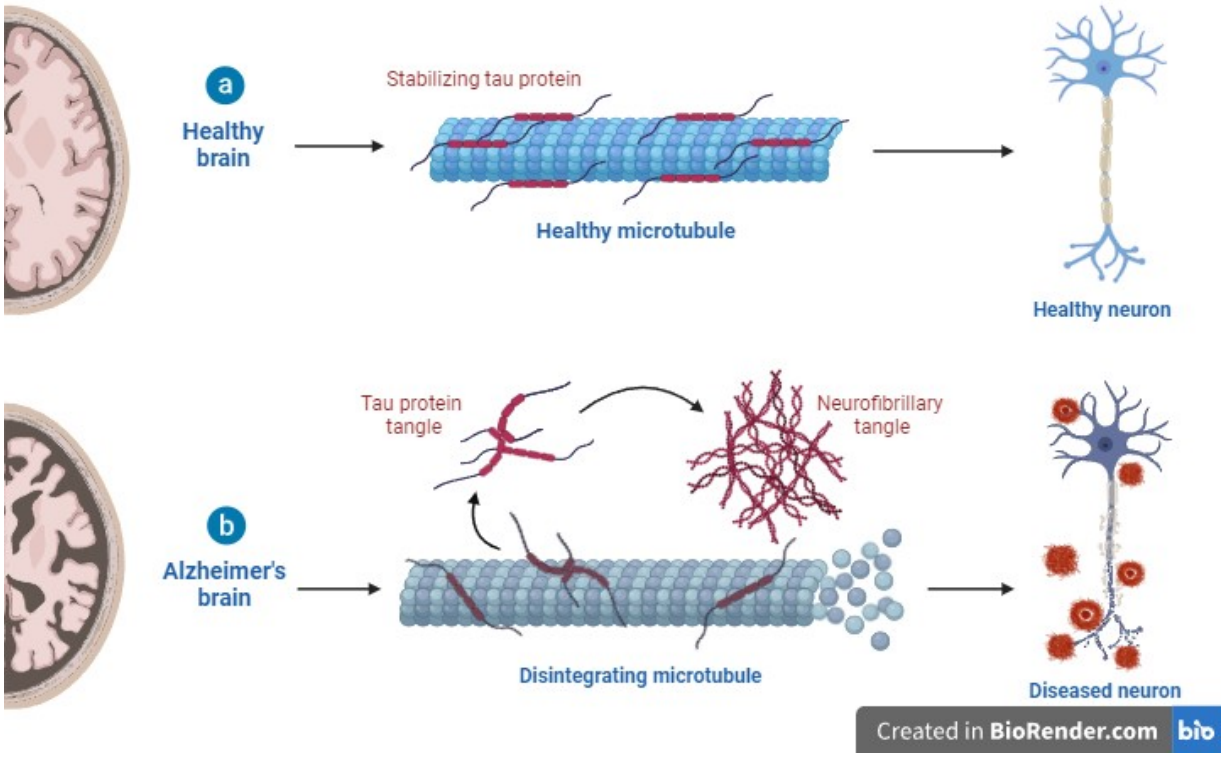

Figure 3: Tau protein in a healthy brain and an AD brain. *In a healthy brain, tau stabilises microtubules and participates in axonal transport. In an AD brain, the formation of NFTs leads to tau aggregation and loss of microtubules stabilisation.*

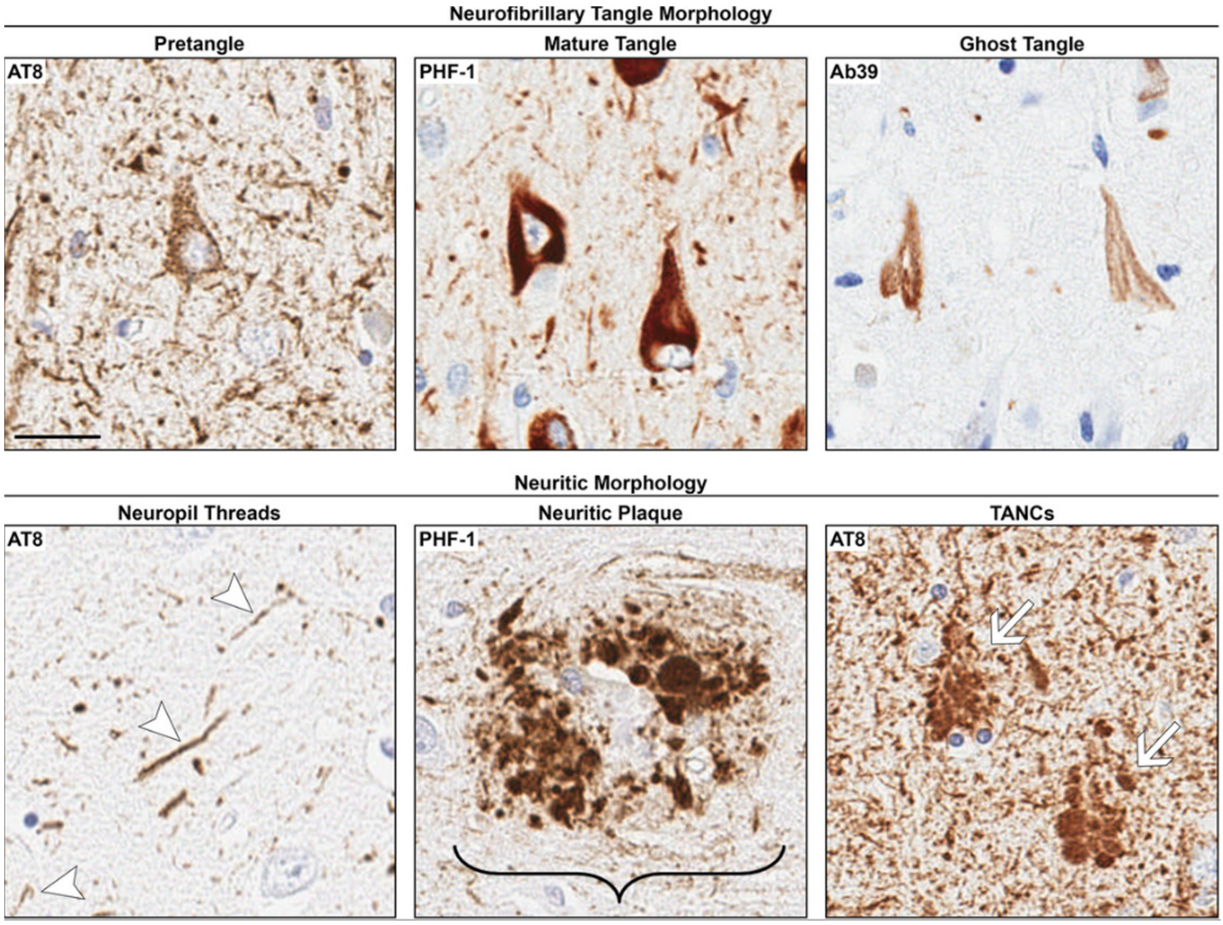

Figure 4: Stages of tau pathology. *NFTs are present in three main stages, pre-tangle, mature tangle, and ghost tangles. Neuritic morphology includes neuropil threads, neuritic plaques, and tangle-associated neuritic clusters (TANCs), scale bar = 25µm (from Moloney et al. 2021).*

1.3 Familial Alzheimer's Disease

There are two main variants of AD, sporadic Alzheimer's disease (SAD) and familial Alzheimer's disease (FAD). The majority of AD cases, over 95-99%, are sporadic in nature. SAD is a multifactorial and polygenic disease and it is characterised by a late age of onset (AoO) over 60-65 years[22]. There are different risk factors for the development of SAD, such as rare genetic variants and environmental causes. The genetic variants are for example polymorphisms in Apolipoprotein E (ApoE) ε4 allele (*APOE4*), ApoE neuronal receptor (SORL1), or glycogen synthase kinase 3 beta (GSK3β). Environmental factors include high-fat diets, exposure to heavy metals, and exposure to pesticides[23]. FAD only represents a small subset of all AD cases (approx. 1% of all cases), and it is caused by mutations in the amyloid precursor protein (*APP*), or in the

presenilins (*PSEN1/2*) genes. The average AoO is lower for FAD, commonly in the fourth dec-decade of life. Brains from FAD affected individuals usually display a higher number of Aβ deposits and are more prone to develop cerebral amyloid angiopathy (CAA), possibly due to the production of more Aβ peptides. Currently, there are over 400 mutations in *APP* and *PSEN1/2* identified[24], and about 90% of all FAD cases are caused by mutations in *PSEN1*[25,26].

Another example is deletions in exon 9 of PSEN1 which lead to AD/spastic paraparesis pedigrees[27]. Mutations within any of the nine transmembrane domains of PSEN1 were shown to cause a more rapid clinical, cognitive, and neurodegenerative progression of FAD than mutations outside of the transmembrane domains[28]. Generally, individuals carrying mutations after codon 200 present with severe CAA and higher Aβ plaque burden, often in the form of cotton wool plaques (CWP)[27,29]. Higher cortical and striatal Aβ burden was described for individuals carrying PSEN1 mutations pre-codon 200[30].In some cases, PSEN1 mutations do not result in classical early-onset AD (EOAD) phenotypes but in other neurodegenerative diseases or mixed presentations. These phenotypes include the absence of typical diagnostic AD symptoms and presentations of different disease phenotypes within the frontotemporal dementia (FTD) spectrum such as behavioural variant frontotemporal dementia (formerly Pick`s disease), Primary progressive aphasia, movement disorders, or dementia with Lewy bodies (DLB)[31].

The p.Glu280Ala, hereafter referred to as E280A, mutation in *PSEN1* is the most common causative mutation[32] of FAD with more than 600 confirmed mutation carriers in the Colombian kindred alone[33]. The E280A carriers present with neuropsychological symptoms such as memory and language impairment and behavioural changes. Recently, Sepulveda-Falla et al. suggested multiple factors are responsible for the age of onset heterogeneity in FAD caused by mutations in *PSEN1* gene[34]. In short, the neuropathological landscape of E280A carriers includes severe brain atrophy, severe Aβ pathology, distinct hyperphosphorylated tau-related pathology, and cerebellar damage[32,35]. Therefore, E280A mutation carriers regularly present with high Thal, CERAD (Consortium to Establish a Registry for Alzheimer's Disease), and Braak scores[36,35] and an increased prevalence of CAA compared to other PSEN1 mutations and SAD[35]. The amyloid burden is similarly high in individuals with an early-onset (EOAD) when compared with average and late-onset patients and SAD. Major cortical areas, namely the frontal, temporal, and parietal cortex, were spared of hyperphosphorylated tau in late-onset E280A carriers, while their

occipital cortex was similarly affected as in both, EOAD and SAD patients[34]. There is a consid-considerable involvement of the cerebellum in FAD neuropathology, which is evident in clinical symptoms such as discoordination, intention tremor, ataxic gait, and dysdiadochokinesis. However, it was shown that motor deficits, as well as dementia, precede Aβ aggregation. Likewise, there was no correlation between amyloid burden and the extent of Purkinje cell loss or the presence of abnormal mitochondria in the cerebellum of E280A carriers[37]. Furthermore, a shift towards Aβ peptides 1-38, 1-42, and 1-43 has been identified in E280A carriers in comparison to SAD[38]. Additionally, *PSEN1* mutation carriers often present with comorbidities such as cerebrovascular disease, LBD, and TDP-43 proteinopathy which are commonly observed between different dementias and additional pathologies[35]. The frequency of comorbid diagnoses increases with advanced age, leading to more severe clinical phenotypes. Cerebrovascular disease is a common comorbidity in late-onset AD (LOAD) cases, but CAA was shown to be similarly present in EOAD and LOAD. DLB, on the other hand, is strongly associated with autosomal dominant AD (ADAD) and Spina et al. showed that DLB co-pathology is confined to the amygdala in EOAD[36,39,40].

Recently, the evidence for vascular pathologic mechanisms contributing to AD has increased[41]. FAD mutation carriers presented with greater total white matter (WM) degeneration and white matter hyperintensities (WMH) in a study from the Dominantly Inherited Alzheimer Network (DIAN)[42]. Traditional cardiovascular risk factors such as high BMI, high blood pressure, and diabetes have been identified in AD, as well as pre-existing vascular disease in form of WM abnormalities. Thus, accumulating evidence suggests that vascular factors modify disease onset proportional to the severity and the threshold for dementia[43–45].Over the years, the focus has shifted from protein deposits to other contributing factors modifying the disease presentation. Several risk factors have been associated with disease progression and severity, such as age, environmental factors, or pre-existing vascular disease, to name a few. As mentioned above *APOE4* was identified as the genetic risk factor in SAD, modifying the age of onset. The risk of developing SAD is three times higher when the *APOE4* allele presents a heterozygous, and 15 times higher when it presents as homozygous[5]. Further, BBB breakdown contributes to cognitive decline independent of Aβ-pathology in *APOE4* carriers[46].

1.4 Cerebral Small Vessel Disease

Small vessel disease (SVD) is an umbrella term for pathological changes to small end arteries, arterioles, venules and brain capillaries resulting in reduced or interrupted perfusion of the affected organ[47]. A major risk factor for SVD is high blood pressure (HBP), which is a systemic condition leading to end organ damage in several organs like the brain, the retina and the vascular system among others. Other risk factors include diabetes mellitus, hyperlipidaemia, smoking or cardiovascular disease[48]. SVD is thought to be the cause of vascular cognitive impairment and dementia (VICD) when it affects the brain[49]. Cerebral SVD (CSVD) is a common neurological disease with higher prevalence associating with ageing. It causes stroke, dementia, mood disturbances, and gait problems[50]. CSVD is the leading cause of vascular dementia (VaD)[41] and is responsible for 20% of all strokes[9]. The presence of SVD can be shown by CT scans, FLAIR, T1 and T2-weighted MRI. Those neuroimaging tools can reveal subcortical infarcts, white matter hyperintensities (WMH), lacunes, microbleeds, and enlarged perivascular spacing in the basal ganglia and subcortical white matter[47]. White matter lesions include myelin loss, scattered small infarcts, and astrogliosis[51]. Acute CSVD presents as lacunar strokes or intracerebral haemorrhages while chronic CSVD presents with progressive cognitive impairment, posture, and gait disorders caused by white matter damage as well as depression[9]. When associated with CSVD, hypertension leads to the deposition of eosinophilic material in the connective tissue of the vessel wall causing infarctions. Pathologically, this causes proliferation of the connective tissue fibres, dilatation of the perivascular space (PVS), and blood-brain barrier impairment due to vascular endothelial cell dysfunction[9].

CAA is a form of CSVD and the 2nd most common cause of cerebral hemorrhage[52,53]. CAA, alongside arteriosclerosis, is the earliest change in CSVD. Lacunar infarcts, microinfarcts, and microbleeds occur independently or in the final phases of the disease[54]. Microemboli or microthrombi artery-to-artery thromboembolism are possible independent causes for lacunar infarcts[55]. Further, microaneurysms caused by a disruption in blood flow due to arteriolar stiffening and tortuosity alongside can cause CSVD[54]. Vascular alterations such as cerebrovascular resistance and hypoperfusion were shown to precede amyloid deposition[56,57]. The reduction of cerebral blood flow caused by constricting capillaries has been identified in some studies as the earliest event in AD, and reduction of cerebral blood flow (CBF) was suggested to start the amyloid cascade with BACE1 and hyperphosphorylation of tau being

upregulated as a result[58]. Ante-mortem vascular disease often stays undiscovered in AD patients, while post-mortem studies show a higher degree of vascular pathology in AD patients than in healthy individuals[54]. Furthermore, there are ethnoracial differences, whether patients present with pure AD pathology or mixed pathologies. Presentation of pure AD pathology was observed in a majority of non-Hispanic white populations while in black and Hispanic populations mixed pathologies were more commonly observed (Fig. 5)[59].

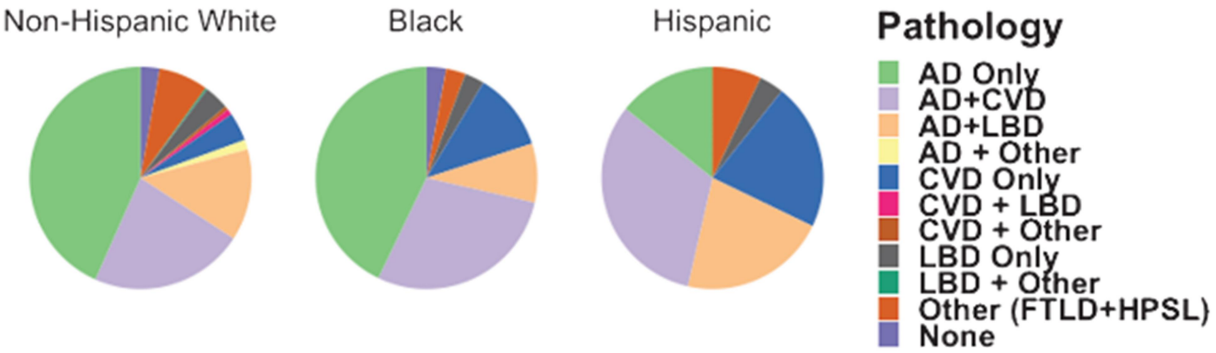

Figure 5: Ethnoracial differences in mixed pathology *(from Filshtein et al. 2019)*

1.5 Notch3 signalling in mural cells in AD

Notch proteins are transmembrane proteins important for cell-cell communication and cell fate decisions. There are four different Notch proteins (1-4) which can bind to delta or jagged ligands for activation. Notch3 signalling plays an important role in the maturation, maintenance, and function of the vasculature. Further, it promotes growth and homeostasis of vascular smooth muscle cells (VSMC)[60]. Notch3 is cleaved by furin-like convertase resulting in an active, ligand-accessible form. Upon ligand-binding Notch is cleaved by TNF-alpha converting enzyme, resulting in the notch extracellular truncation (NEXT) fragment, which is cleaved by the γ-secretase. Cleavage by the γ-secretase results in the release of the Notch intracellular domain (NICD) which translocates to the nucleus and acts as a transcription promotor element[61]. Being responsible for the final cleavage of Notch3, the γ-secretase takes an important role in Notch3 processing. The canonical downstream targets of Notch signalling are Hairy and enhancer of split (Hes) and Hairy/enhance-of-split related with YRPW motif (Hey). However, only the expression of Hes1, Hes5, Hes7, and the Hey genes are activated by classical Notch signalling, while Hes2, Hes3, and are induced independently from Notch signalling. Additionally, Notch

signalling induces the expression of c-Myc, cyclins and (Platelet Derived Growth Factor Recep-Receptor β) PDGFRβ[62]. Non-canonical Notch signalling independent of ligand/transcription has been described. Here the NICD interacts with proteins in the cytoplasm or with non-Notch targets in the nucleus. Further Notch-associated signalling without Notch receptor activation is described as non-canonical Notch signalling. However, this is poorly studied, especially in the vasculature[62]. The *NOTCH3* gene differs from the other Notches by having 34 instead of 36 epidermal growth factor (EGF)-like repeats (EGFR) and a shorter cytoplasmic domain.

Known *NOTCH3* mutations often occur within the exons 2 to 24 of the gene, which encodes the extracellular domain of Notrch3 (NE3XT). The EGFR of NE3XT normally contains six cysteine residues that form three disulphide bonds stabilising the NE3XT. *NOTCH3* mutations are single-base substitutions or missense mutations resulting in an odd number of cysteine residues[63]. This alters the formation of disulphide bridges which affects the stability of NE3XT. Thus, possibly promoting misfolding, aggregation, and aberrant function of the receptor. In conclusion, each distinct *NOTCH3* mutation affects Notch3 signalling differently[60]. Finally, *NOTCH3* is mainly expressed in mural cells such as VSMC and pericytes[64,60], highlighting the importance of N3 in the context of the neurovascular unit. N3 loss of function was shown to induce mural cell degeneration and CSVD[65].

1.6 Neurovascular unit and mural cell pathology

The neurovascular unit (NVU) is comprised of different cell types, including endothelial cells, pericytes, and astrocyte end-feet. These form an endothelial cell layer, a smooth muscle cell layer, and an outer layer of leptomeningeal cells, termed adventitia, which is separated from the brain by the Virchow-Robin space. As the arterioles penetrate deeper into the brain, this space disappears, and the vascular basement membrane comes into direct contact with the astrocytic end-feet (intracerebral arterioles and capillaries)[66]. In capillaries, smooth muscle cells are replaced by pericytes, contractile cells that are particularly abundant in brain vessels and are involved in the development and maintenance of the BBB[67]. Endothelial cells and pericytes are encased in the basement membrane (BM), thin layers of highly specialised extracellular matrix (ECM) that are giving endothelial cells a supporting structure to grow[68]. Perineuronal nets (PNN) contain ECM structures and assemble around neurons. The vascular BM consists of laminin, collagen IV, fibronectin, and heparan sulfate proteoglycans (HSPGs)[69]. Proteoglycans are glycoproteins with attached glycosaminoglycans (GAGs), which give the proteoglycan a

negative charge, giving those lubricant and space-filling functions[70]. Cell migration, prolifera- proliferation, and differentiation can be controlled by BM components through growth factor signalling[71]. The remodelling of ECM is a constant process to maintain tissue homeostasis and it is achieved by cleavage of ECM components. The ECM can be cleaved by matrix metalloproteinases (MMPs), adamalysins (ADAMs and ADAMTS), meprins, or metalloproteinase inhibitors. MMPs are the main enzymes cleaving all ECM components taking an important role in organogenesis and branching morphogenesis. ADAMs cleave transmembrane protein ectodomains adjacent to the cell membrane. This releases growth factors, receptors, adhesion molecules, and the complete ectodomain of cytokines. Meprins can cleave collagen IV, nidogen, and fibronectin and activate the other metalloproteinases to regulate ECM remodelling indirectly. To avoid excessive tissue degradation, inhibitors are needed for the metalloproteinases. The tissue inhibitor of metalloproteinases (TIMP) family consists of four members inhibiting the activity of MMPs, ADAMs, and ADAMTS but not meprins[72]. Astrocytes express different glycoproteins such as GPC5[73] and tenascin-C (TNC)[74] whereas endothelial cells were shown to produce versican (VCAN) or perlecan[75]. Further, astrocyte end-feet covers the entire vascular tree facilitating brain homeostasis[76].

Astrocyte and vascular development were shown to be highly connected. During the formation of new blood vessels endothelial cells and astrocytes secret extracellular matrix proteins which form the basement membrane that encapsulates endothelial cells and smooth muscle cells or pericytes[77] (Fig. 6). Depending on the position of the pericyte, different subtypes of pericytes have been identified; mesh pericytes, thin-stranded pericytes and ensheathing pericytes. Ensheathing pericytes are thought to be transitional mural cells displaying both characteristics of pericytes and VSMC. Further, these are located on precapillary arterioles with shorter cell lengths and express α-smooth muscle actin (SMA) while mesh and thin-stranded pericytes are located on smaller diameter capillaries with longer cell lengths and no detectable α-SMA[41]. Additionally, pericytes express cell surface antigens such as Neural/glial antigen 2 (NG2), PDGFRβ, and CD13 and contractile and cytoskeletal proteins such as α-SMA and desmin[78]. However, also fibroblast-like cells and others were found to express PDGFRβ[79]. This leads to conflicting results about for example pericytes coverage in health and disease[80–82] where the loss of pericytes results in BBB breakdown and associated leakage of neurotoxic molecules into the

brain parenchyma[83]. Endothelial cells line the blood vessels, and through gap junctions and ad-adhesion plaques, endothelial cells and pericytes are in direct contact, allowing ionic currents to pass between their cytoplasms. Further, the pericytes are tethered to the endothelial cells via the adhesion plaques. The direct connections are further enabled through peg-and-socket junctions providing a form of pericyte-endothelial anchorage[41,84].

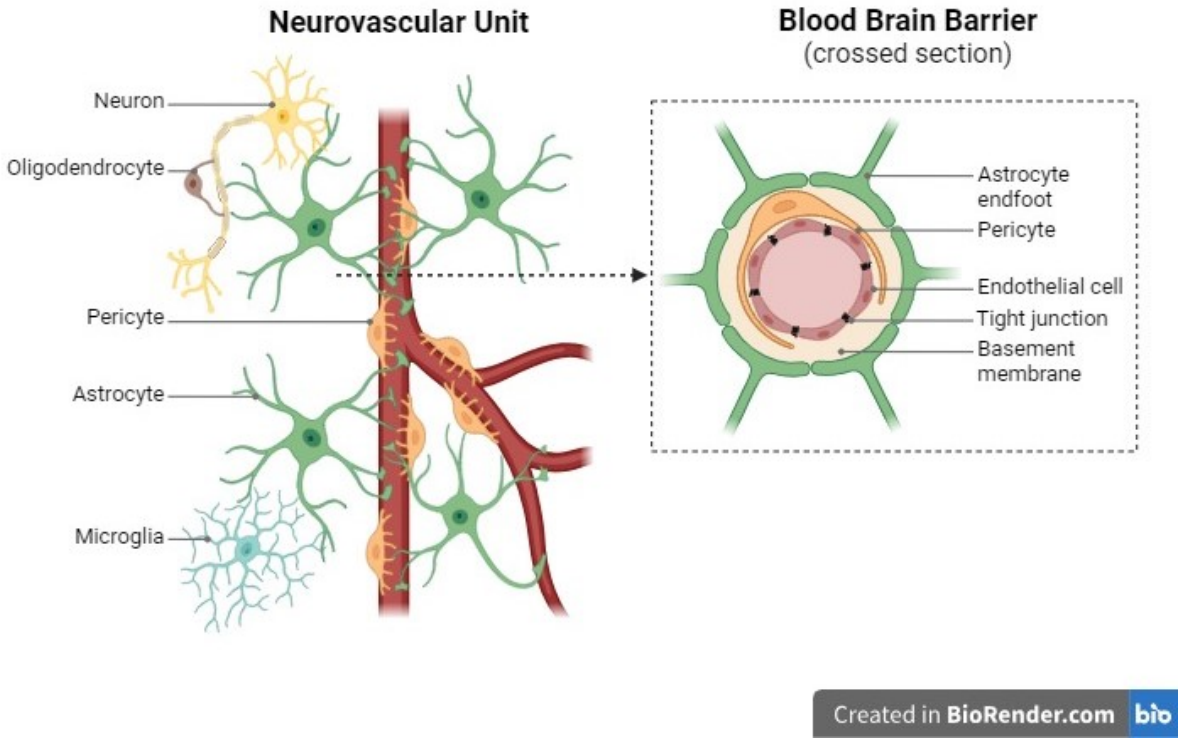

Figure 6: Neurovascular Unit and Blood Brain Barrier. *Astrocytes, pericytes, and the vessel build the neurovascular unit. Microglia, neurons, and oligodendrocytes are adjacent. The cross-section illustrates how endothelial cells form a tight barrier with tight junctions embedded in the basement membrane while pericytes cover endothelial cells. Astrocytes surround the whole vessel.*

Endothelial cells express three types of junctional proteins forming junctional complexes: adherens junctions (e.g. vascular endothelial cadherin), gap junctions (connexins), and tight junctions (e.g. claudin-5 (CLDN-5) and occludin). Paracellular permeability is limited by the junctional proteins expressed by brain endothelial cells. These cells show, for instance, a higher expression of claudin-5 (CLDN-5) which is imperative for limiting the movement of small molecules across the BBB[85]. Next, it was shown that endothelial cell-pericyte communication is important for the barrier strength and depends on pericyte coverage[41]. Loss of the endothelial cell-pericyte signalling leads to various changes including pericyte loss, endothelial cell

activation and extravasation of immune cells, loss of balanced Aβ transport, and breakdown of the extracellular matrix/basement membrane due to reduced inhibition of the cyclophilin A-matrix metalloproteinase pathway. The following transcriptional changes lead to a more venous phenotype with an increased transcytosis and uptake of neurotoxic substances. The dysregulation of vasoactive substances such as nitric oxide leads to reduced cerebral blood flow. Finally, there are morphological changes with aberrant angiogenesis[41] and for example, degenerated appearing pericytes with clusters of collagen fibres between lamellae of basement membranes[54]. Crosstalk of pericytes and endothelial cells is essential to maintain a functional BBB because the loss of pericytes results in BBB breakdown. One of these crosstalk points it the endothelial sphingosine-1-phosphate (S1P) receptor is involved in regulating pericyte vessel coverage by controlling N-cadherin trafficking to the membrane. S1P receptors were shown to be reduced in AD brain tissue[86] and dysregulation of S1P is implicated in neuroinflammation. Additionally, S1P possesses neuroprotective agencies by reducing Aβ-induced neuronal apoptosis[87]. Thus, S1P and the S1P receptor are involved in the pathophysiological mechanisms of dementia.

Both, endothelial cells and pericytes have been implicated in disease[81,78,83]. However, there are more mechanistic studies needed, to clearly identify pericyte subtypes and pericytes of different origins and their role in BBB dysfunction[88,89]. Lastly, vessel stability requires Notch for the adhesion of endothelial cells and VSMC to the basement membrane and astrocyte end-feet for the vessel homeostasis.

2. Objectives

Vascular dysfunction is pivotal in the pathogenesis of AD, this project cynosure is the relation between protein aggregates, Aβ and tau, and vascular abnormalities. For that the following aims were set:

a) To evaluate the presence and degree of vascular pathology in FAD.
b) To determine the Aβ composition in and around brain vessels.
c) To identify molecular changes and key pathways of vascular pathology in FAD, SAD, and healthy controls.
d) To determine whether tau dysregulation influences or is influenced by vascular pathology.
e) To evaluate early vascular changes caused by the E280A mutation in a knock-in mouse model.

3. Material and Methods

2.1 Human Subjects

The following domains were evaluated in the patients: cognitive/affective symptoms, motor symptoms, language (table 1), and cardiovascular risk factors which were evaluated as absent (0) or present (1) (Fig. 7). In total six healthy controls (HC), ten SAD and 32 FAD cases, carrying the E280A mutation, were assessed. While there was no clinical data available for the HC or SAD cases, they were chosen based on the neuropathological assessment by lack or presence of AD pathological findings, respectively. Table 2 shows the clinical data and the demographics of 32 FAD subjects studied. The *PSEN1* E280A FAD family was first identified over 30 years ago and had regular follow-ups since then using the CERAD protocol, NINCDS-ADRA, and DSM-IV criteria[90,91]. The FAD cases were chosen to be representative for this population. The SAD cases were severity-matched to the FAD cases, and the healthy controls were age-matched. The SAD cases presented with no history of AD in their genealogy. Informed consent from patients or family members was given, and brain donations were performed in accordance with the ethical guidelines of Universidad de Antioquia, Medellín, Colombia.

2.2 Histological and immuno-histochemical analysis

In this thesis brain tissue from Brodman areas 10 (frontal cortex, FC), 20/21 (temporal cortex, TC), 7 (parietal, PC), 17 (occipital, OC), basal ganglia (caudate- putamen at the level of anterior commissure) and the anterior hippocampal formation was assessed using 4µm thick sections from formalin-fixed paraffin-embedded tissue. These were stained for haematoxylin and eosin (H&E) and luxol fast blue. Additionally, immunohistochemical staining was performed for amyloid beta (Aβ), phospho-Tau Ser202, Thr205 (AT8), platelet derived growth factor receptor beta (PDGFRβ), aquaporin-4 (AQP4), fibrinogen, glial fibrillary acidic protein (GFAP) and laminin. Detailed antibody information can be found in table 3. The immunostaining was performed as described before[36]. Briefly, the sections were dewaxed, and endogenous peroxidases (PBS/3% hydrogen peroxide) were inactivated, followed by antibody-specific antigen retrieval, blocking and incubation of primary antibodies. The Ultra View Universal 3,3'-Diaminobenzidine (DAB) Detection Kit (Ventana, Roche) was used to identify specific binding. In order to detect PDGFRβ, sections were additionally blocked with rabbit serum and the anti-goat Histofine Simple Stain MAX PO immune-enzyme polymer (medac GmbH, 414161F) was used as the secondary antibody. The Hamamatsu NanoZoomer automatic digital slide scanner

(Hamamatsu Photonics, Hamamatsu, Japan) was used to obtain High-resolution scans of the stained sections with a resolution of at least 1 pixel per µm. Total area measurements were done with the ImageJ Software (version 1.52p, NIH, Bethesda, MA, USA.).

2.3 Assessment of vascular pathology

The presence of vascular pathology was graded based on the methods published by Deramecourt et al.[92] and Skrobot et al.[93]. Single scores for arteriosclerosis, CAA, perivascular hemosiderin leakage, PVS dilatation, and myelin loss were given. The final vascular score takes the presence of cortical microinfarcts, large or lacunar infarcts, and haemorrhages into account.

2.4 Quantification of CAA

Leptomeningeal vessels, cortical microvessels, and capillaries were evaluated for Aβ reactivity as described by Love et al.[94]. The scores for leptomeningeal vessels and cortical microvessels ranged from zero (no CAA present) to three (severe CAA present). In the case of capillary CAA only presence was evaluated, with a score of zero meaning no capillary CAA was present and one that capillary CAA was present. For a subset of FAD cases all non-CAA, CAA, and partial CAA vessels in frontal and occipital cortices were counted.

2.5 PVS quantification

The perivascular space dilatation was quantified for 15 CAA and non-CAA vessels in the occipital cortices of 32 FAD and 10 SAD. Aβ stained sections were used for PS1 FAD cases to differentiate between CAA and nonCAA vessels. PVS was measured also in the frontal cortices of 20 FAD cases. Images at 5X magnification were exported from the whole-image scan file, using the NDP.view2 software (Hamamatsu Photonics, Hamamatsu, Japan). Then, ImageJ Software (version 1.52p, NIH, Bethesda, MA, USA) was used to measure the longest distance between the parenchyma and the vessel to determine the exact size of the perivascular spaces. The PVS ratio was calculated by dividing this distance by the diameter of the measured vessel. To exclude vessel size as the determinant for larger perivascular spaces, the caliber of the vessels <50µm, 50-90µm and >90µm diameters were measured in the same manner as the perivascular space dilatation.

Table :1 Domains evaluated in the FAD patients. *The scores and their meaning are given for the domains evaluated.*

Cognitive/Affective Symptoms	Memory impairment	0	Absent
		1	Anterograde
		2	Retrograde
		3	Mixed
	Spatial disorientation	0	Absent
		1	Present
	Agnosia	0	Absent
		1	Prosopagnosia
		2	Visual agnosia
		3	Auditory
		4	Astereognosis
		5	two or more of the above
	Apraxia	0	Absent
		1	Present
	Insomnia	0	Absent
		1	Present
	Hallucinations	0	Absent
		1	Visual
		2	Auditory
		3	Mixed
	Seizures	0	Absent
		1	Present
	Depression	0	Absent
		1	Present
Motor Symptoms	Tremor	0	No tremor
		1	Slight/Moderate
		2	Severe
	Rigidity	0	No rigidity
		1	Present, full range of motion achieved
		2	Present, full range of motion not achieved
	Gait	0	Independent walking
		1	Requires an assistance device for safe walking or another person´s assistance
		2	Cannot walk at all / Bedridden
	Bradykinesia	0	Absent
		1	Slight/Mild global slowness and poverty of spontaneous movements
		2	Moderate/Severe global slowness and poverty of spontaneous movements
Language	Speech	0	Absent
		1	Dysarthria
		2	Anarthria
	Aphasia	0	Absent
		1	Broca´s aphasia
		2	Wernicke´s aphasia
		3	Mixed
	Alexia	0	Absent
		1	Present
	Agraphia	0	Absent
		1	Present
	Anomia	0	Absent
		1	Present
	Echolalia/Perseveration	0	Absent
		1	Present

Table 2: Clinical History of FAD cases. *Sex (1=male, 2=female), AoO, AoD, DD, PMI, Apoe Genotype, Cognitive/Affective symptoms, Motor symptoms, Language and Cardiovascular Risk Factors are shown. Abbreviations: AoO: age of onset, AoD: age of death, DD: disease duration, PMI: post-mortem intervall, MI: memory impiarment, SD: spatial disorientation, AGn: agnosia, Apr: apraxia, IN: insomnia, HA: hallucinations, SE: Seizures, DE: depression, TR: tremor, RI: rigidity, GA: gait, BR: bradykinesia, SP, speech, APh: aphasia, Ale: alexia, AGr: apraphia, ANo: anomia, EC/PE: echolalia/perseveration, HPB: high blood pressure, BMI: body mass index, NG: no genotype, ND: no data*

Sex	AoO	AoD	DD	PMI	ApoE	i. Cognitive / Affective symptoms.								ii. Motor symptoms				iii. Language					
						MI	SD	AGn	APr	IN	HA	SE	DE	TR	RI	GA	BR	SP	APh	ALe	AGr	ANo	EC/PE
2	55	64	9	ND	NG	1	1	5	1	1	1	1	1	0	2	2	1	2	0	1	1	1	1
1	57	60	3	4.33	33	1	0	0	0	1	0	1	1	0	1	2	1	0	1	1	1	1	1
2	51	54	3	13.00	34	1	1	1	1	1	1	1	0	0	2	2	1	1	0	0	1	1	1
2	45	50	5	7.33	33	1	1	1	1	0	0	0	1	1	0	1	2	2	1	0	1	1	0
1	46	52	6	4.75	33	1	0	5	1	0	1	1	0	0	1	2	1	1	1	0	0	0	1
2	55	64	9	3.00	33	1	1	5	1	1	1	1	1	0	1	2	1	2	0	0	0	1	0
2	40	42	2	5.50	33	1	1	0	1	1	1	1	1	1	0	1	1	2	3	0	2	1	0
1	47	55	8	4.33	33	1	1	1	1	1	1	1	1	1	1	0	1	0	1	1	1	1	1
2	57	62	5	4.16	33	1	1	1	1	0	1	1	1	0	1	2	2	2	0	0	0	1	1
2	45	48	3	4.00	33	3	0	1	1	0	1	1	1	0	1	1	1	1	0	0	0	0	0
2	41	47	6	3.33	33	1	1	1	1	1	0	1	1	1	1	1	1	2	0	1	1	1	1
2	52	60	8	2.08	33	3	1	1	1	1	0	1	1	1	1	2	1	2	0	1	1	1	1
2	48	52	4	2.50	23	1	1	1	1	1	1	1	1	0	0	2	0	2	0	0	0	0	0
2	62	74	12	5.50	33	1	1	ND	1	1	1	1	ND	ND	ND	2	ND	2	3	ND	ND	ND	ND
1	56	63	7	4.25	33	1	1	1	1	1	1	1	1	0	1	1	0	1	0	0	0	0	0
1	44	51	7	3.55	33	1	1	1	1	1	1	1	1	0	1	1	1	1	3	1	1	1	1
2	47	52	5	8.50	33	1	0	0	1	1	1	1	1	0	2	2	0	1	0	1	1	1	1
2	58	64	6	3.58	34	1	1	1	1	1	1	1	1	0	2	2	1	1	1	0	1	1	0
2	49	61	12	15.50	33	1	1	1	1	1	2	1	0	1	1	2	1	2	3	1	1	1	1
1	44	48	4	11.66	NG	1	0	0	1	0	0	0	0	1	1	1	1	1	1	ND	ND	ND	ND
1	45	53	8	7.16	NG	1	1	1	1	1	0	1	0	0	1	1	0	1	1	1	1	1	0
1	55	61	6	7.33	33	1	1	1	1	1	1	1	1	0	1	1	1	1	3	0	0	0	0
2	49	57	8	7.75	NG	1	1	0	1	1	2	0	1	0	1	1	1	2	1	0	0	1	0
1	58	64	6	4.00	NG	1	ND	ND	ND	ND	ND	ND	1	ND	1	1	ND	ND	ND	ND	ND	ND	ND
2	50	57	7	10.75	33	1	1	1	1	1	0	0	1	0	1	0	1	2	0	0	0	0	1
1	57	64	7	5.00	NG	1	1	0	1	1	1	1	1	1	1	1	0	2	1	ND	ND	1	1
1	42	47	5	3.32	NG	1	1	0	1	1	1	0	1	1	1	2	0	2	2	0	0	1	0
1	52	61	9	4.00	34	1	1	1	1	1	0	0	1	0	1	2	1	1	1	1	1	1	1
1	47	54	7	14.33	NG	1	1	1	1	1	0	0	1	1	1	1	1	2	0	0	0	1	0
2	45	51	6	16.66	33	1	0	0	1	1	0	1	1	0	2	2	1	2	1	0	0	1	0
2	52	60	8	5.08	33	1	0	0	1	1	0	1	1	1	1	2	0	2	0	0	0	0	1
1	51	62	11	4.25	33	1	1	0	1	1	3	1	1	1	0	2	1	2	0	0	1	1	1

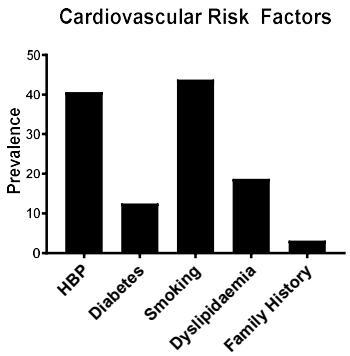

Figure 7: Prevalence of Cardiovascular Risk Factors in the FAD Cohort.

Table 3: Primary and secondary antibodies used.

Name	Article #	Company	Species	Dilution
Amyloid β	BAM-10	DBS Emergo Europe	Mouse	1/100
Amyloid β 1-16	803003	Biolegend	Mouse	1/200
Amyloid β 17-24	800703	Biolegend	Mouse	1/200
Aquaporin-4	HPA014784	Merck KGaA	Rabbit	1/2000
Aquaporin-4	429 006	Synaptic Systems	Guinea Pig	1/200
pTau Ser202, Thr205 (AT8)	MN1020	ThermoFisher Scientific	Mouse	1/200
Collagen IV	462 004	Synaptic Systems	Guinea-Pig	1/500
Fibrinogen	A0080	DAKO	Rabbit	1/2000
Glial fibrillary acidic protein	M0761	DAKO	Mouse	1/100
Glial fibrillary acidic protein	173 308	Synaptic Systems	Guinea-Pig	1/200
Glypican-5	PA5-83490	ThermoFisher Scientific	Rabbit	1/200
Laminin	NBP2-44751	Novus Biologicals	Rat	1/200
Laminin	L9393	Sigma-Aldrich	Rabbit	1/30
Lectin-488	L21415	ThermoFisher Scientific	-	1/200
PDGFRβ	AF385	R&D Systems	Goat	1/50
pTau 205	ab254410	Abcam	Rabbit	1/200
pTau 217	produced in house by Lei Liu at Harvard University		Rabbit	1/1000
pTau 231			Rabbit	1/1000
α-smooth muscle actin	MOB001-05	Diagnostic Biosystems	Mouse	1/1000
Secreted modular calcium-binding protein 1	PA5-31392	ThermoFisher Scientific	Rabbit	1/100
Tenascin C	NB110-68136	Novus Biologicals	Mouse	1/50
Versican	NPB3-15841	Novus Biologicals	Rabbit	1/50
Goat anti-Rat 488	A-11006	ThermoFisher Scientific	Rat	1/200
Donkey anti-Mouse 488	A21202	ThermoFisher Scientific	Mouse	1/200
Donkey anti-Rabbit 555	A31572	ThermoFisher Scientific	Rabbit	1/200
Goat anti-Guinea-Pig 647	A21450	ThermoFisher Scientific	Guinea Pig	1/200

2.6 PDGFRβ Immunoreactivity

In order to assess mural cell integrity periarteriolar PDGFRβ immunoreactivity was quantified for 100 cortical vessels in 21 FAD and 10 SAD cases. Briefly, colour deconvolution[95] was performed using ImageJ Software (version 1.52p, NIH, Bethesda, MA, USA). The H&E vectors were used to separate the channels. The brown channel, which contains the PDGFRβ immunoreactivity, was used for quantification. The automatic threshold was applied and PDGFRβ-positive objects were measured. Particles smaller than 100 μm^2 were excluded from this analysis. Larger artefacts were excluded by subtracting the top 1% of each dataset. Additionally, PDGFRβ signal restricted to vessels was assessed in vessels with thickened walls and perivascular space dilatation.

2.7 AQP4 Immunoreactivity

In order to assess astrocyte end-feet, sections were stained for AQP4. In 21 FAD and 10 SAD cases the AQP4 immunoreactivity was quantified, for each, 15 vessels with dilated and undilated perivascular spacing. Images of vessels were exported at 80X magnification from the high-resolution scan with 1280x1032 pixels. For the quantification, colour deconvolution was used as described above, followed by applying a threshold and measuring the total AQP4 signal.

2.8 Ultrastructural analysis of human postmortem manterial

As described before, three FAD cases were further studied using ultrastructural analysis. Briefly, formalin-fixed temporal cortices of three FAD cases were fixed in glutaraldehyde and chrome-osmium, dehydrated in ethanol, and embedded in Epon 812 (Serva Electrophoresis GmbH, Heidelberg, Germany). Following the polymerisation, 1-mm thick sections were cut, stained with toluidine blue, and checked for the presence of arterioles. Selected areas were cut for electron microscopy by cutting 100 nm-thick sections and contrasted with uranyl replacement stain (22405, Electron Microscopy Sciences, Hatfiled, PA, USA) and lead citrate solution. Stained sections were assessed and representative images were taken using a LEO EM 912AB electron microscope (Zeiss, Oberkochen, Germany).

2.9 Serial block-face scanning electron microscopy of murine samples

The serial EM was performed by Mark Ellisman et al. at the National Center for Microscopy and Imaging Research, UCSD, San Diego CA, as previously described[96,97]. Briefly, Mice were perfused with PBS, followed by perfusion with 2% formaldehyde / 2.5% glutaraldehyde in 0.15 M sodium cacodylate buffer (CB) with 2 mM $CaCl_2$. Perfused brains were kept in the perfusion solution at 4°C until processing. The brains were cut into 100µm thick coronal sections. underwent several chemical treatments, including osmication, thiocarbohydrazide treatment, uranyl acetate staining, and en bloc lead aspartate staining, before dehydration and embedding in Durcupan resin. Subsequently, flat-embedding between glass slides coated with mold-release compound was performed, and the samples were polymerized in an oven at 60°C for 72 hours. A Gemini SEM (Zeiss, Oberkochen, Germany) equipped with a Gatan 3 View system and a focal nitrogen gas injection setup was used to perform serial block-face scanning electron microscopy (SBEMs). This setup facilitated precise nitrogen gas application over the block-face of the region of interest (ROI) during imaging under high vacuum conditions to maximize SEM image resolution. Imaging parameters included a 2.5 kV accelerating voltage, 1 µs dwell time, XY pixel

sizes of 4 or 5 nm, 60 nm Z steps, and a raster size of 15 k × 15 k in x and y dimensions. Volumes were collected with a 65% nitrogen gas injection under high vacuum conditions. Post-acquisition, histograms for slices throughout the volume stack were normalized to correct for image intensity drift, followed by volume alignment using cross-correlation, segmentation, analysis, and visualization using IMOD software[98].

2.10 Murine vascular measurements

10X magnification images of hippocampus and basal ganglia were exported from high-resolution scans of laminin and SMA stained sections. Following the image pre-processing as described above (PDGFRβ Immunoreactivity) images were skeletonized and the skeleton was analysed using the parameter shortest branch. Results are displayed as tortuosity which is the branch length divided by Euclidian distance. Further, %Area covered (capillary density) by laminin and SMA and the signal intensity were quantified for the same images.

2.11 Clarity

300µm thick mouse brain sections were incubated in hydrogel monomer solution (4% paraformaldehyde / 2% Acrylamide/Bisacrylamide (40%) / 0.05% Acrylamide powder / 0.25% VA-044) for seven days at 4°C. After seven days, the tissue was transferred to a new monomer solution, covered with olive oil, and sealed for four-hour incubation at 37°C. The tissue sections were removed and placed in Sodium dodecyl sulphate (SDS) clearing solution (0.25M boric acid / 4% SDS in ddH_2O) at RT for 48 hours. After this, samples were incubated in SDS clearing solution at 50°C until the tissue was cleared, with the solution being changed every two days. Once cleared, samples were washed with washing solution (0.10% Triton-X 100 / 0.01% sodium azide in PBS) and incubated with primary antibodies (dilution 1:50, in washing solution) for five days. Samples were washed for two days before incubation of secondary antibodies (dilution 1:50, in washing solution) for another 5 days. Samples were washed a final time before incubating the samples in 63% TDE for imaging with the Leica TCS SP8 confocal laser scanning microscope with a 63X immersion oil lens objective.

2.12 Multiplex of tau phosphosites

4µm thick sections of frontal and occipital cortices were deparaffinised and treated against auto-fluorescence by exposure to UV light and immersion in 50mM NH_4Cl. Heat-induced antigen retrieval was performed using 1X R-Universal buffer (AP0530-500; Aptum Biologics, Southampton, UK) in a pressure cooker for 15min. After washing with PBS, slides were

permeabilised in 0.25% Triton/PBS before blocking with MAXblock^{TM}-Blocking medium for 1 hour at RT. Antibodies were incubated in MAXbind^{TM} staining medium overnight at 4°C. Sections were washed in 1X PBS twice and 30min in MaxWashTM washing solution before incubating with secondary antibodies for 1 hour at RT (for antibody information see table 3). This was followed by the same washing steps and incubation with 0.3% sudan black for 15min. Sections were mounted using DAPI Fluoromount-G (SouthernBiotech, #0100-20). Images were taken with a Leica SP8 microscope within 48 hours of mounting the sections. In order to strip the slides of the antibodies, slides were placed into water at RT to loosen the coverslips. The stripping solution was prepared as published in Gendusa et al.[99]. In short, 100mL 10% SDS with 62.5mL 0.5M Tris-HCl (pH 6.8), 337.5mL deionised water and 4mL β-ME were mixed, and preheated to 56°C and sections were incubated for 45min. To completely remove the stripping solution, sections were washed with water four times for 15min and once with 1X TBS + 0.01 % Tween 20 for 5min. After this, the sections were blocked and stained again. Images at 20X for quantification purposes were obtained using the Leica TCS SP8 confocal laser scanning microscope while representative images were taken with the 20X immersion oil lens objective.

2.13 Vessel isolation human – IP Aβ & IF

Approximately 400mg of cortical tissue was homogenized and centrifuged (4°C) at 2000 xg for 5min. For the proteomics samples, 100µL of the homogenate were transferred to a clean tube before centrifugation for phosphoTau proteomics. The pellet was resuspended in 15% (wt/vol) 70-kDa dextran and centrifuged (4°C) for 15min at 10.000 xg. Isolated microvessels were further processed for proteomics or immunofluorescence staining. For the proteomics samples, the microvessel containing pellet was retrieved and resolved in 300µL lysis buffer, sonicated, and centrifuged (4°C) at 14000 xg for 15min. 40µL of the vessel lysate were transferred to a new tube for the total vessel proteomics. The rest of the supernatant was used for immunoprecipitation of Aβ using the Dynabeads Protein G (Thermofisher Scientific, 10003D), alongside two antibodies recognising the amyloid peptide 1-16, 6E10, antibody and the amyloid peptide 17-24, 4G8, were used. All samples were stored at -80°C until analysis.

Isolated microvessels processed for immunofluorescence staining were retrieved in PBS, washed with PBS in a 40µm filter, and retrieved in 0.5% BSA/PBS. After centrifugation for 10min at 2000 xg the microvessels are resuspended in 1X PBS and transferred to slides for air drying. For immunofluorescence staining microvessels were wet with 1X PBS, permeabilised with 0.25%

Triton X-100/PBS, and blocked with MAXblock^{TM}-Blocking medium (Active Motif, #15252). Primary antibodies were prepared in MAXbind^{TM} staining medium (Active Motif, #15253) and incubated overnight at 4°C. The slides were washed three times with MaxWashTM washing solution (Active Motif, #15254) before incubation of secondary antibodies. The slides were washed again before mounting with DAPI Fluoromount-G (SouthernBiotech, #0100-20). High-resolution images were taken with a Leica TCS SP8 confocal laser scanning microscope (Leica Microsystems, Mannheim, Germany) using a 63X immersion oil lens objective.

2.14 Aβ peptidomics

Bottom-up proteomics was performed by Biogenity ApS, Denmark. Shortly, the immunoprecipitated samples were eluted with 100µL 0.5% formic acid and desalted on SOLAµ SPE plate^{100} and 500ng were loaded onto EvoStep stagetips according to the manufacturer's protocol. The peptides of each sample were analysed using the pre-set '30 samples per day' method on the EvoSep One instrument. Peptides were eluted over a 44-min gradient and analysed with the Orbitrap Exploris instrument (ThermoFisher Scientific), which was run in DDA mode with FAIMS ProTM Interface (ThermoFisher Scientific) cycling between CVs of -50 V and -70 V every 28 scans. Full MS spectra were collected at a resolution of 60.000, with an automatic gain control (AGC) target of 300% or maximum injection time set to 'auto' and a scan range of 375–1500 m/z. MS1 precursors with an intensity of $>5\times10^3$ and a charge state of 2-6 were selected for MS2 analysis. Dynamic exclusion was set to 60 s, the exclusion list was shared between CV values and Advanced Peak Determination was on. Precursors selected for MS2 were isolated in the quadrupole with a 1.6 m/z window. Ions were collected to a normalized AGC target set to 75% and maximum injection time was set to 'auto'. Fragmentation was performed with Higher-energy collisional dissociation normalised collision energy of 30% and MS2 spectra were acquired in the orbitrap at a resolution of 15,000. MS performance was verified for consistency by running complex cell lysate quality control standards, and chromatography was monitored to check for reproducibility. Proteome Discoverer 2.4 (ThermoFisher Scientific) was used to process the raw files with Label-free quantification (LFQ) being enabled in the processing and consensus steps. The spectra were matched against the Uniprot Homosapiens database including reviewed and unreviewed proteins. The enzyme was set to "No enzyme (unspecific)". Dynamic modifications were set as Oxidation (M) and Acetyl

on protein N-termini. All results were filtered to a 1% FDR, and protein quantitation was done using the built-in Minora Feature Detector.

The peptide information was analysed using Protti[101], an R package for the analysis of peptide bottom-up proteomics data. First, the intensities were log2 transformed and normalised to the median value of all runs. The peptide intensities were filtered for those related to APP. Technical peptides were summarised to the biological peptides, for example Aβ37 contains all peptides ending at position 37. To test if there is a difference between the peptide abundances in the paired comparisons, differential analysis on peptide level was performed using moderated t-test based on the limma R package[102]. A comparison was considered significant if the adjusted *p* (BH correction method) was lower than 0.05. Additionally, the Aβ42/Aβ40 ratio was calculated based on the intensities and significance was tested using a Welch's t-test. The comparison was considered significant if the *p* was lower than 0.05.

Finally, a functional enrichment analysis was conducted for the peptide co-immunoprecipitated alongside Aβ using EnrichR[103–105]. A clustergram was generated using the top 20 significant Gene Ontology (GO) biological process (BP) terms and the top 60 related proteins.

2.15 Total vessel proteomics

The vessel lysate was cleaned up by acetone precipitation by mixing it with 100% acetone to an acetone concentration of 80% and incubated overnight at 20°C. The samples were centrifuged and the pellet was lysed in lysis buffer (6 M Guanidinium Hydrochloride, 10mM TCEP, 40mM CAA, 50mM HEPES, pH8.5) and boiled at 95°C for 5min. Finally, the samples were sonicated on high for 5x 30 seconds in a Bioruptor sonication water bath (Diagenode) at 4°C. Next, samples were diluted 1:3 with 10% acetonitrile, 50mM HEPES pH8.5, and LysC (MS grade, Wako) was added in a 1:50 (enzyme to protein) ratio. Samples were incubated at 37°C for 4 hours. Samples were diluted further 1:10 with 10% acetonitrile, 50mM HEPES pH8.5 and trypsin (MS grade, Promega) was added 1:100 (enzyme to protein) ratio. Samples were incubated at 37°C overnight. All enzyme activity was quenched by adding 2% trifluoroacetic acid (TFA) to a final concentration of 1%. Samples were speedvac'ed for 30min at 50°C before being acidified and desalted on SOLAμ SPE plate (HRP, Thermo), as described above. Dried peptides were reconstituted in 12 µL 2% acetonitrile, 1% TFA/20µL HEPES 50mM pH8.5. TMT labelling with 16 plex tags (ThermoFisher Scientific) was performed with part of the digested

sample. To acidify and reduce acetonitrile concentration down to <5%, TFA was added. Peptide fractioning was performed using high pH fractionation (5 mM ammonium bicarbonate, pH10, flowrate µL/min) in an offline ThermoFisher Ultimate3000 liquid chromatography system. 15µg of peptides were separated over a 120min gradient (5% to 25% acetonitrile) and fractions were collected every 130 sec. The resulting 60 fractions were pooled into 15 final fractions, acidified to pH < 2 with 1% TFA and loaded onto EvoSep stagetips according to the manufacturer's protocol. Peptides were eluted over a 44-min gradient and analysed with an Orbitrap EclipseTM TribridTM instrument (ThermoFisher Scientific) with FAIMS ProTM Interface (ThermoFisher Scientific) switched between CVs of -50 V and -70 V with cycle times of 2 s and 1.5 s respectively. Full MS spectra were collected at a resolution of 120.000, with normalized AGC target set to 100% or maximum injection time of 50ms and a scan range of 375–1500m/z. MS1 precursors with an intensity of >5×103 and charge state of 2-7 were selected for MS2 analysis. Dynamic exclusion was set to 120 s and the exclusion list was shared between CV values. Advanced Peak Determination was set to 'off'. The precursor fit threshold was set to 70% with a fit window of 0.7m/z for MS2. Precursors selected for MS2 were isolated in the quadrupole with a 0.7m/z window. Ions were collected for a maximum injection time of 35ms and normalized AGC target set to 300%. Fragmentation was performed with HCD normalized collision energy of 30% and MS2 spectra were acquired in the IT at a scan rate rapid. The MS2 spectra were subjected to RTS using the Uniprot protein database Homo sapiens and trypsin set as enzyme. Static modifications were TMTpro on Lysine (K) and N-terminus and carbamidomethyl on Cysteine (C). Oxidation of methionine (M) was set as variable modification. Maximum missed cleavages was set to 1 and maximum variable modifications to 2. FDR filtering enabled, maximum search time was set to 35ms, and the scoring threshold was set to 1 Xcorr, 0 dCn, and 5 ppm precursor tolerance. Use as trigger only was disabled and close-out was enabled with maximum number of peptides per protein set to 4. Precursors were subsequently filtered with an isobaric tag loss exclusion of TMT and precursor mass exclusion set to 25 ppm low and 25 ppm high. Precursors identified by RTS were isolated for an MS3 scan using the quadrupole with a 2 m/z window, and ions were collected for a maximum injection time of 86 ms and normalized AGC target of 300%. Turbo TMT was deactivated and the number of dependent scans set to 10. Isolated precursors were fragmented again with 50% normalised HCD collision energy, and MS3 spectra were acquired in the orbitrap at 50000 resolution with a scan range of 100-500m/z. MS

performance was verified for consistency by running complex cell lysate quality control stand-standard. The raw files were analysed as described above with minor modifications. Shortly, MaxQuant[106] was used but with TMT reporter ion quantification enabled instead of LFQ. The spectra were matched against Uniprot as before. Dynamic modifications were set as Oxidation (M) and Acetyl on protein N-termini. Cysteine carbamidomethyl (on C residues) and TMT 16-plex (on peptide N-termini and K residues) were set as static modifications. All results were filtered to a 1% FDR, and protein quantitation was done using the built-in Minora Feature Detector. Intensities were extracted from the MaxQuant output and used as input data for the next steps. The proteins were log2 transformed and normalised based on the Peptide spectrum match (PSMs) by using MSstatsTMT[107]. The intensity column was logarithmically transformed and a global median normalisation between the channels was done. To receive protein data out of the peptide data a protein summarization per MS run and channel was done. Finally, local protein-level normalisation was performed against the TMT pool channel. For the differential expression analysis, the normalised protein summaries were used as input to empirical Bayes moderated t-statistics using limma[102]. The results were considered significant if $p < 0.05$. To gain more biological insight into the differentially expressed proteins (DEPs), a Gene Set Enrichment Analysis (GSEA) was run using clusterProfiler package[108] and Gene Ontology database (GO). The multiple tests were corrected with the BH method. Next, Weighted Gene Co-Expression Network Analysis (WGCNA) was performed to study biological networks based on pairwise correlations. The WGCNA R package[109] was used. Briefly, a network analysis for each cortex was performed using the proteins which presented with valid values among all cases. The following parameters were used: soft threshold power beta=8, deepSplit=4, minimum module size=20, merge cut height=0.25, and a signed network in the blockwiseModules() function. To gain more insights into the protein expression between cortices in FAD, an additional network analysis taking FC and OC of FAD cases into account. For this network the following parameters were used: soft threshold power beta=12, deepSplit=4, minimum module size=20, merge cut height=0.25, and a signed network was used to run this analysis. Module-trait relationships were determined to calculate the correlations between each module eigenprotein and a clinical or neuropathological trait and the corresponding *p*. Heatmaps that show the correlation analysis were made with pheatmap package[110]. Those module proteins that showed a significant

correlation and significance with the traits were analysed using functional enrichment with the clusterProfiler package.

2.16 phosphoTau proteomics

SysQuant® phosphoproteomic analyses were performed by Proteome Sciences. 34 OC samples, 20 FAD, 8 SAD and 6 HC, and 17 FC samples, 10 FAD, 4 SAD and 3 HC, were provided. The provided homogenates were diluted in SysQuant® lysis buffer, sonicated, and equal amounts from all lysates were taken off and mixed to produce a reference pool sample. There was one reference pool for OC samples and a separate one for FC samples. The 34 individual OC lysates and two reference pool aliquots were trypsinated, the resulting peptides were labelled with one of 18 isobaric TMTpro™ reagents and then mixed to generate two TMTpro™ 18plex analytical samples. These TMTpro™ 18plex samples were split into an aliquot for total proteome analysis (non-enriched) and an aliquot for phosphopeptide-enrichment. Basic reversed-phase fractionation was applied to generate 6 phosphopeptide-enriched and 6 non-enriched fractions per each 18plex. Each fraction was subjected to LC-MS/MS analysis on an Orbitrap Fusion™ Tribrid™ mass spectrometer using a data-dependent acquisition method. The FC homogenates were processed in the same manner with a single 18plex sample. The MS data files were processed in Proteome Discoverer v2.5 (ThermoFisher Scientific). Since the samples were run in 3 batches due to the size of the study cohort, harmonizR[111,112] was used to integrate the batches. Peptide abundances before and after batch integration were plotted using the ggplot2 R package[113]. Phosphopeptide level analysis was conducted using the R package PhosR[114]. Shortly, phosphopeptides were filtered to be present in at least 60% of the samples from one group and imputation was performed. This was followed by quantile normalisation of the imputed data using limma and differential phosphopeptide expression analysis using moderated empirical Bayes statistics was conducted. In order to understand the behaviour of all unique peptides related to pTau, a heatmap per each brain region was generated by using z-score transformed relative peptide abundances. Next, the different phosphosites of MAPT were assigned to the 2N4R isoform (441 amino acids) and bar diagrams representing these were generated. Finally, to compare the different detected phosphosites, phosphosites intensities were determined by summing all normalised peptides intensities that contain that specific phosphosite. To identify kinases that preferentially target MAPT, PhosR was used to perform kinase enrichment on the common upregulated MAPT phosphosites (logFC >= 0.5) between the comparisons FAD vs HC

and FAD vs SAD per each cortex. Briefly, this kinase-substrate relationship scoring is based on a multi-step kinase-substrate scoring where the likelihood of a kinase to regulate a phosphosite is scored by combining both kinase recognition motifs and the dynamic phosphorylation profiles of sites. In order to understand the difference between FC and OC in FAD, a kinase-substrate ratio score (FC/OC) of common phosphosites and kinases was calculated and plotted as a heatmap. Additionally, the batches had to be integrated using harmonizR[111,112]. The batches before (Annex Fig. 1A) and after (Annex Fig. 1B) harmonizR application are shown. The medians of the batches are brought together. The normalised TMT data (Annex Fig. 1C) was plotted for each case. To determine that the batch correction did not affect the data distribution, PCA was used for the FC and OC samples separately. In both cases, FC (Annex Fig. 1D) and OC (Annex Fig. 1E), the HC are clustered together off to one side, while FAD and SAD cases were partially mixed.

4. Results

Chapter 1: Evaluation of vascular pathology in Alzheimer's disease

3.1 Vascular pathology

Vascular pathology was evaluated in a total of 32 familial Alzheimer's disease (FAD) individuals and 10 sporadic Alzheimer's disease (SAD) individuals. The grading system established by Deramecourt et al.[92] was used. It allows summarizing the presence of vascular pathologies such as arteriosclerosis (Fig. 8A, B), perivascular spacing (Fig. 8C, D), microinfarcts (Fig. 8E, F), myelin loss (Fig. 8G, H), and cerebral amyloid angiopathy (CAA) (Fig. 8C), into a single score. First, vascular pathology was compared to healthy controls (HC) in FC. There was significantly more vascular pathology in the Frontal Cortex (FC) of FAD versus HC and SAD (Fig. 8I). Generally, vascular pathology was present in both FAD and SAD in FC, TC, PC, and OC albeit FAD showed a significantly higher score for the FC in comparison to SAD (Fig. 8J). Arteriosclerosis could be observed across regions without significant differences between FAD and SAD (Fig. 8A, B, J). A similar trend could be observed for perivascular spacing (PVS) where no significant differences could be observed between FAD and SAD (Fig. 8C, D, K). Taken together, these findings show the presence of vascular pathology in FAD, undetected ante mortem by neuroimaging. A more detailed description of these findings can be seen in one of the publications derived from this project, in Littau et al.[36].

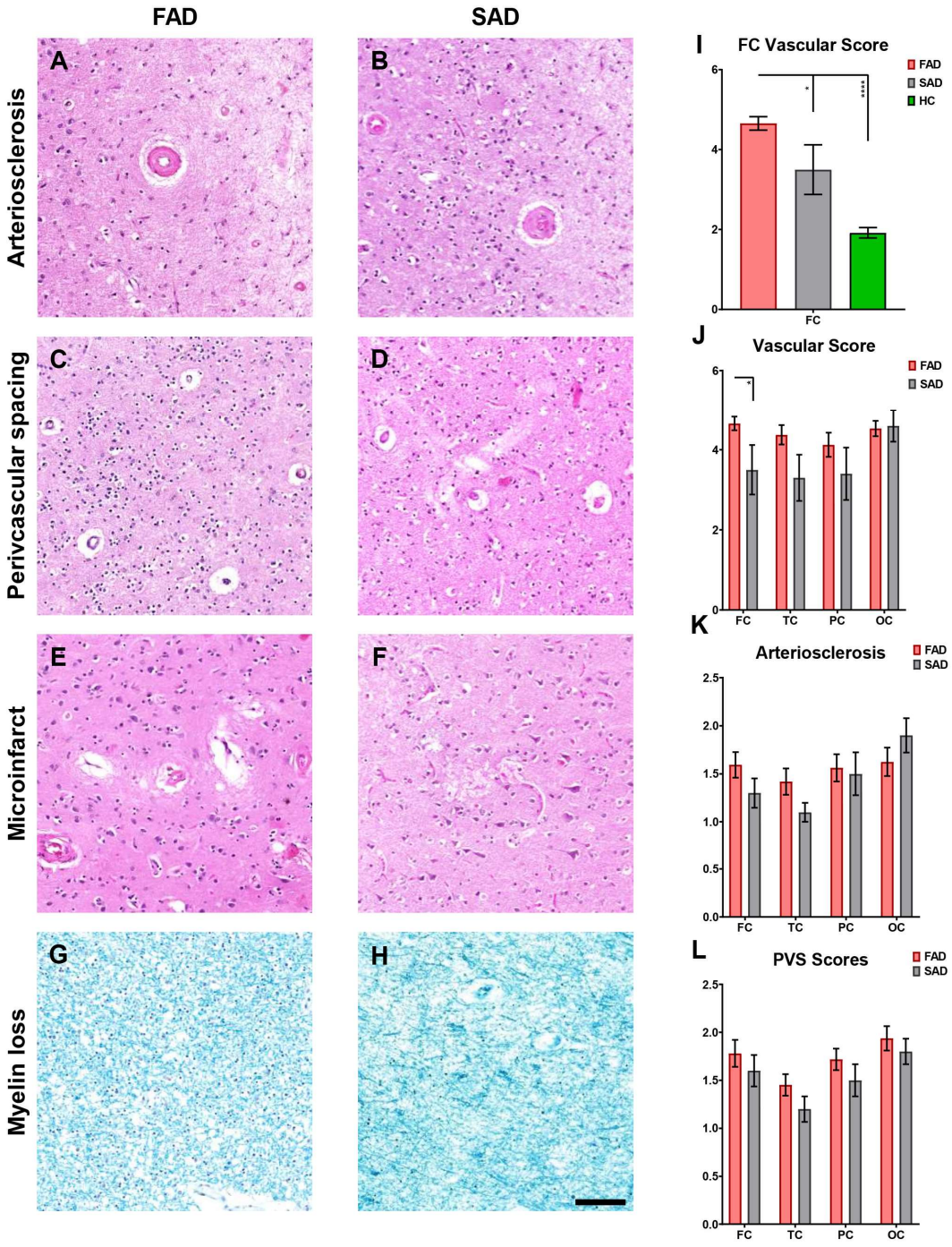

Figure 8: Vascular pathology in FAD and SAD. *Representative images of arteriosclerosis (A-B), perivascular spacing (C-D), microinfarcts (E-F) are shown for the OC in H&E staining and myelin loss (G-H) is shown in Luxol Fast Blue staining from the OC for FAD and SAD, scale bar = 100µm. The average vascular score for frontal cortex (FC), temporal cortex (TC), parietal cortex (PC) and occipital cortex (OC) are shown for FAD (n=32) and SAD (n=10). FAD presented with a significantly higher score for frontal cortex in comparison to SAD (p: *=0.0197) (I). Arteriosclerosis did not present with significant differences between PS1 FAD and SAD (J) neither did perivascular spacing scores (K).*

3.2 CAA pathology and perivascular spacing

To determine whether the observed difference of vascular pathology in FC versus the other cortices in FAD and SAD is associated with amyloid pathology, cerebral amyloid angiopathy (CAA) was evaluated. The CAA VCING scale[93] was used to evaluate the presence of leptomeningeal, cortical, and capillary CAA. There was significantly less CAA in the PC of SAD in comparison to FAD while the other cortices did not show significant differences (Fig. 9D). To obtain a better understanding of the CAA distribution in the cortices, all unaffected (Fig. 9A); partially affected by CAA (Fig. 9B), and fully covered by CAA (Fig. 9C) vessels were counted in FC and OC, from 20 FAD and 10 SAD cases.

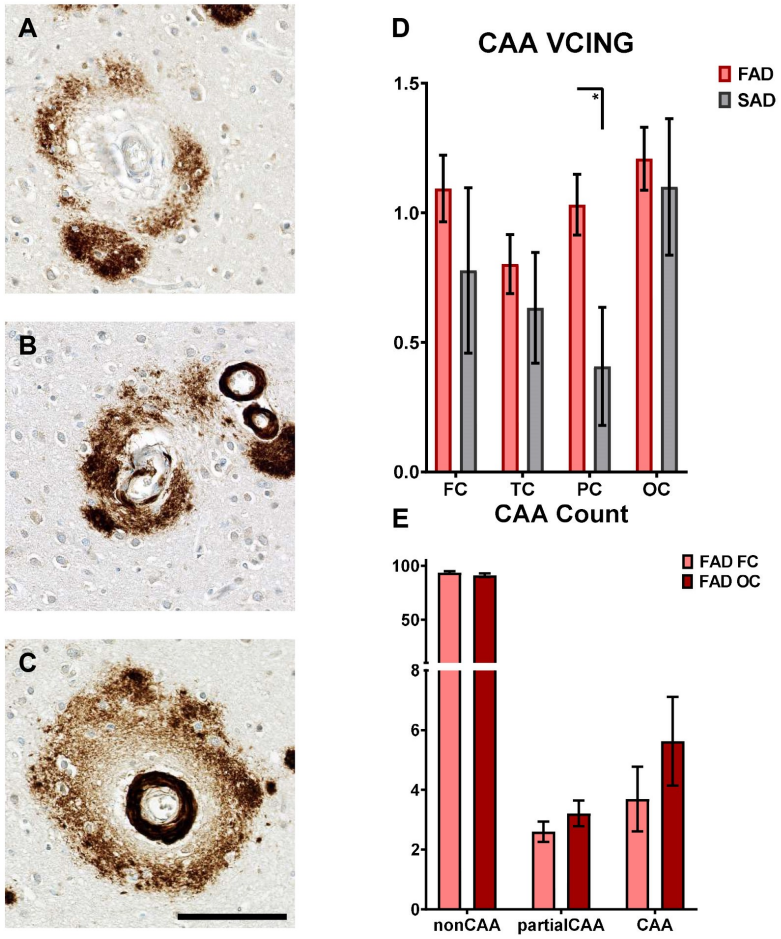

Figure 9: CAA pathology in FAD and SAD. *Representative images of the OC of FAD are shown for CAA unaffected vessels (A), partial CAA vessels (B) and CAA Vessels (C), scale bar = 100µm. CAA VCING was scored for PS1 FAD (n=32) and SAD (n=10) and showed a significant difference between PS1 FAD and SAD in PC (p: *= 0.0103) (D). Further, all vessels in PS1 FAD were counted (n=20) in the frontal and occipital cortices revealing no significant differences (E).*

The percentage of vessels affected by CAA was less than 15% in both areas, in both FAD and SAD, and there were no significant differences in the percentage of vessels affected by CAA or partial CAA between FC and OC (Fig. 8E). Thus, CAA pathology was similar between FAD and SAD from a morphological point of view.

Subsequently, the composition of Aβ in and around vessels was studied in FAD and SAD by using Aβ immunoprecipitation, followed by peptidomics.

The Aβ peptides were compared in FC FAD versus SAD, OC FAD versus SAD as well as within groups, frontal FAD versus occipital FAD, and frontal SAD versus occipital SAD. In the FC of FAD patients significantly less Aβ37 and Aβ38 was found in comparison to FC SAD (Fig. 10A). Differences in Aβ40 and Aβ42 were not significantly different. The ratio of Aβ42/Aβ40 was significantly higher in the FC of FAD versus SAD (Fig. 10B). The comparison between OC FAD and OC SAD did not yield any significant differences, either for the individual peptides levels or the Aβ42/Aβ40 ratio (Fig. 10C, D). When comparing within groups the frontal and occipital cortex, neither in FAD nor in SAD, differ in peptide composition (Fig. 10E, G). The Aβ42/Aβ40 was significantly higher for FC FAD versus OC FAD (Fig. 10F). This ratio was not significantly different when comparing the FC of SAD versus the OC in SAD (Fig. 10H). The Aβ peptidomics showed differences in FC of FAD which drove the significant differences compared to FC SAD and OC FAD.

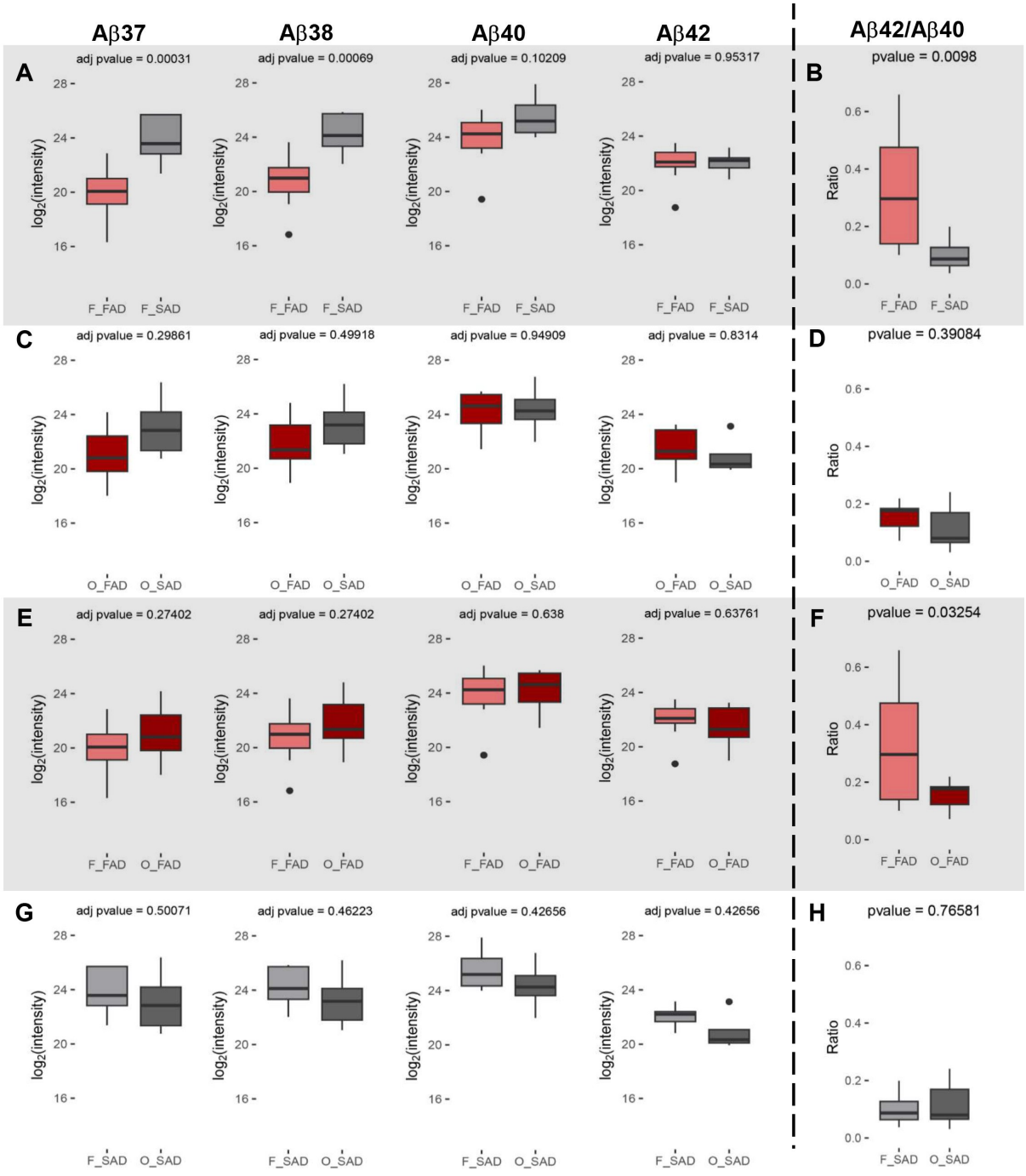

Figure 10: Aβ peptidomics in FAD and SAD. *Log2 abundances are shown for all comparisons. First, Ab peptides Aβ37 and Aβ38 are significantly higher in frontal cortices of SAD (n=4) versus FAD (n=10), while Aβ40 and Aβ42 were not significantly different in frontal FAD versus frontal SAD (A). Further, the ratio of Aβ42/Aβ40 was significantly different between frontal FAD and SAD (B). Next, in occipital cortices, no significant differences were observed between FAD and SAD for the peptides (C) or the ratio (D). Additionally, differences between frontal and occipital within FAD or SAD were studied. The peptides did not differ in frontal and occipital cortices for FAD (E) or SAD (G). The Aβ42/Aβ40 ratio was significantly higher in FAD FC than in FAD OC (F) while this could not be observed for SAD (H).*

The next pathological feature evaluated was the enlargement of perivascular spacing (PVS), in CAA affected and unaffected vessels (nonCAA). The perivascular space of nonCAA and CAA vessels (15 vessels each per case) was measured in the OC of FAD and SAD (Fig. 11A-D). For FAD, the PVS of nonCAA and CAA vessels was measured in the FC due to differences observed in the Aβ peptidomics, and to see if there is a difference between FC and OC in FAD. Vessels were analysed according to size, to exclude a possible influence of size over PVS dilatation. There was significantly enlarged PVS for nonCAA vessels in FAD for vessels with a calibre <50μM and 50-90μM in comparison to all other vessels measured. Additionally, CAA FAD vessels with a calibre <50μM presented with significantly enlarged PVS in comparison to CAA SAD and nonCAA SAD vessels (Fig. 11E). For 50-90μM calibre-sized vessels, CAA FAD vessels showed significantly larger PVS in comparison to CAA SAD vessels (Fig. 11F). However, both regions behave similarly in their distribution of nonCAA and CAA-enlarged PVS. Vessels in the FC with a calibre <50μM affected by CAA were found to have significantly enlarged PVS compared to FC and OC CAA vessels with a calibre of 50-90μM (Fig. 11G). In sum, these analyses showed enlarged PVS for nonCAA vessels in FAD, suggesting Aβ independent vascular pathology in FAD.

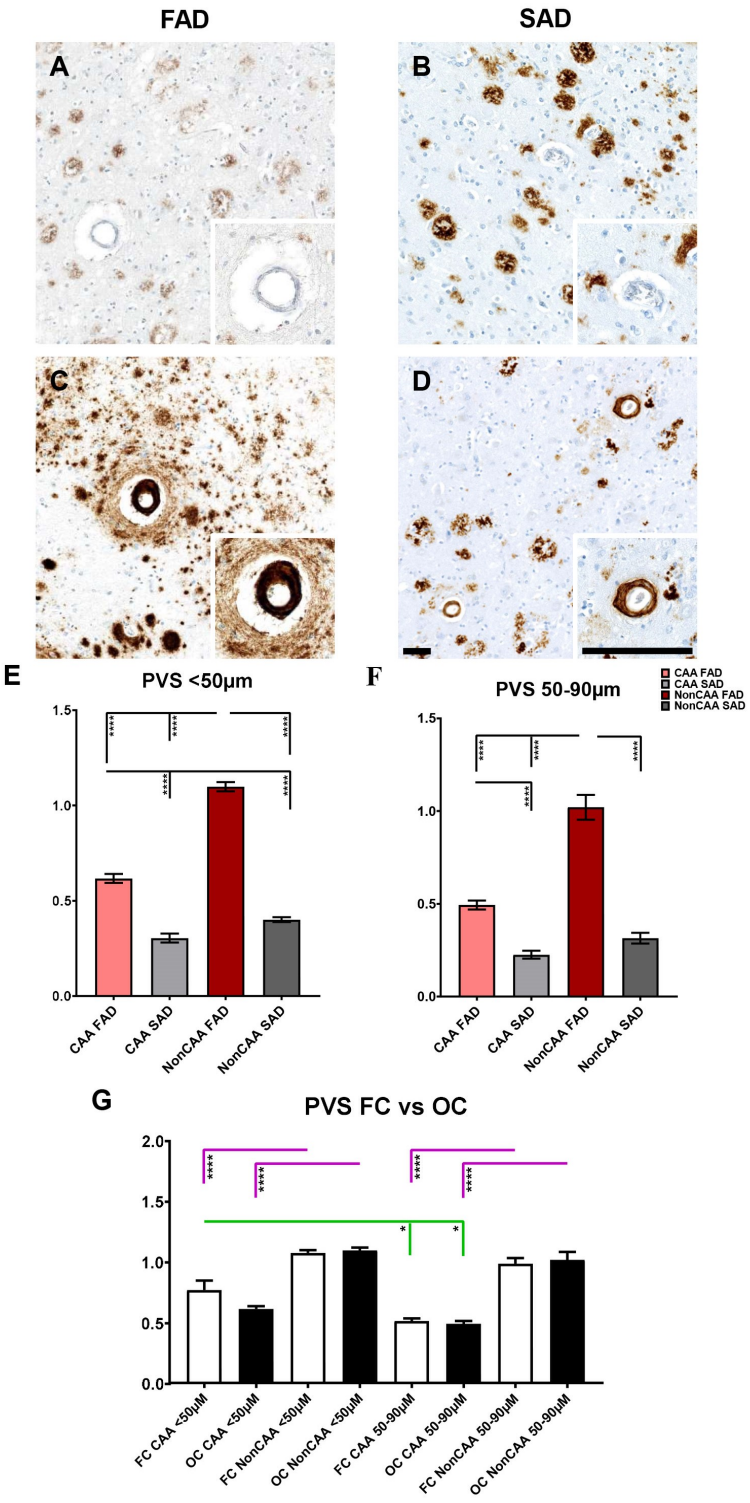

Figure 11: Perivascular spacing in FAD and SAD. *Representative images are shown for nonCAA and CAA vessels in FAD (n=32) and SAD (n=10), scale bar = 100µM (A-D). FAD CAA and nonCAA Vessels with a calibre <50µm presented with significantly enlarged PVS in comparison to SAD (p: ****<0.0001). NonCAA FAD vessels further had significantly enlarged PVS compared to all other vessels types evaluated (p: ****<0.0001) (E). Similarly, was*

*observed for vessels with a calibre of 50-90µm in size (F). In FAD (n=20) the enlargement of PVS in frontal cortex (FC) and occipital cortex (OC) was quantified. Within the cortices, nonCAA vessels had significantly enlarged PVS in comparison to CAA vessels for both vessels <50µm and vessels with a size of 50-90µm (pink significant bars, p: ****<0.0001). Additionally, CAA vessels in FC with a calibre <50µm had significantly enlarged PVS in comparison to FC CAA and OC CAA vessels of 50-90µm calibre (green significance bars, p: *=0.0106) (G).*

3.3 Changes in the gliovascular unit

To see if the pathological changes in the vasculature had an effect on the integrity to the gliovascular unit, different components of the gliovascular unit were evaluated. First, OC sections were stained with PDGFRβ to gain insight into mural cell pathology as pericytes take a big part in vessel homeostasis and integrity. Overall, FAD presented with less PDGFRβ immunoreactivity. The perivascular signal was measured for vessels with dilated PVS and non-dilated PVS. Per case 15 vessels were analysed each. Dilated (Fig. 12A) and non-dilated (Fig. 12B) vessels in FAD had significantly less perivascular signal/area than the dilated (Fig. 12C) and non-dilated (Fig. 12D) SAD vessels. Additionally, non-dilated FAD vessels had significantly less perivascular PDGFRβ signal in comparison to dilated FAD vessels (Fig. 12E). Thus, vessels with enlarged PVS, independent of Aβ pathology, additionally presented with less pericyte coverage of the vessel. To see if this was connected to changes in the gliovascular unit, astrocyte end-feet were evaluated by quantifying perivascular AQP4 immunoreactivity surrounding both, dilated and non-dilated vessels in FAD and SAD (Fig. 12F-I). There were no significant differences between FAD and SAD in perivascular AQP4 signal; however, dilated FAD vessels had significantly less perivascular AQP4 signal than non-dilated FAD vessels (Fig. 12J). Ultrastructural studies were conducted in human post mortem brain tissue, to evaluate the structure of the gliovascular unit at a higher resolution. The loss of pericytes was evident with EM in Healthy Controls (HC) and FAD tissue. The analysis revealed pericytes undergoing apoptosis as well as a thickening of the basement membrane without a disruption of tight junctions in the endothelial cells (Fig. 12K).

In summary, FAD cases presented with a high degree of vascular pathology which was unrelated to Aβ pathology and similar to the vascular pathology observed in SAD. The evaluation of the gliovascular unit implicated dysregulation in FAD in the form of less pericyte coverage of vessels, the loss of astrocyte end-feet, and thickening of the basement membrane. These changes, together with morphological evidence of vascular pathology regardless of presence of CAA, suggest additional SVD mechanisms besides CAA deposition in the vessels.

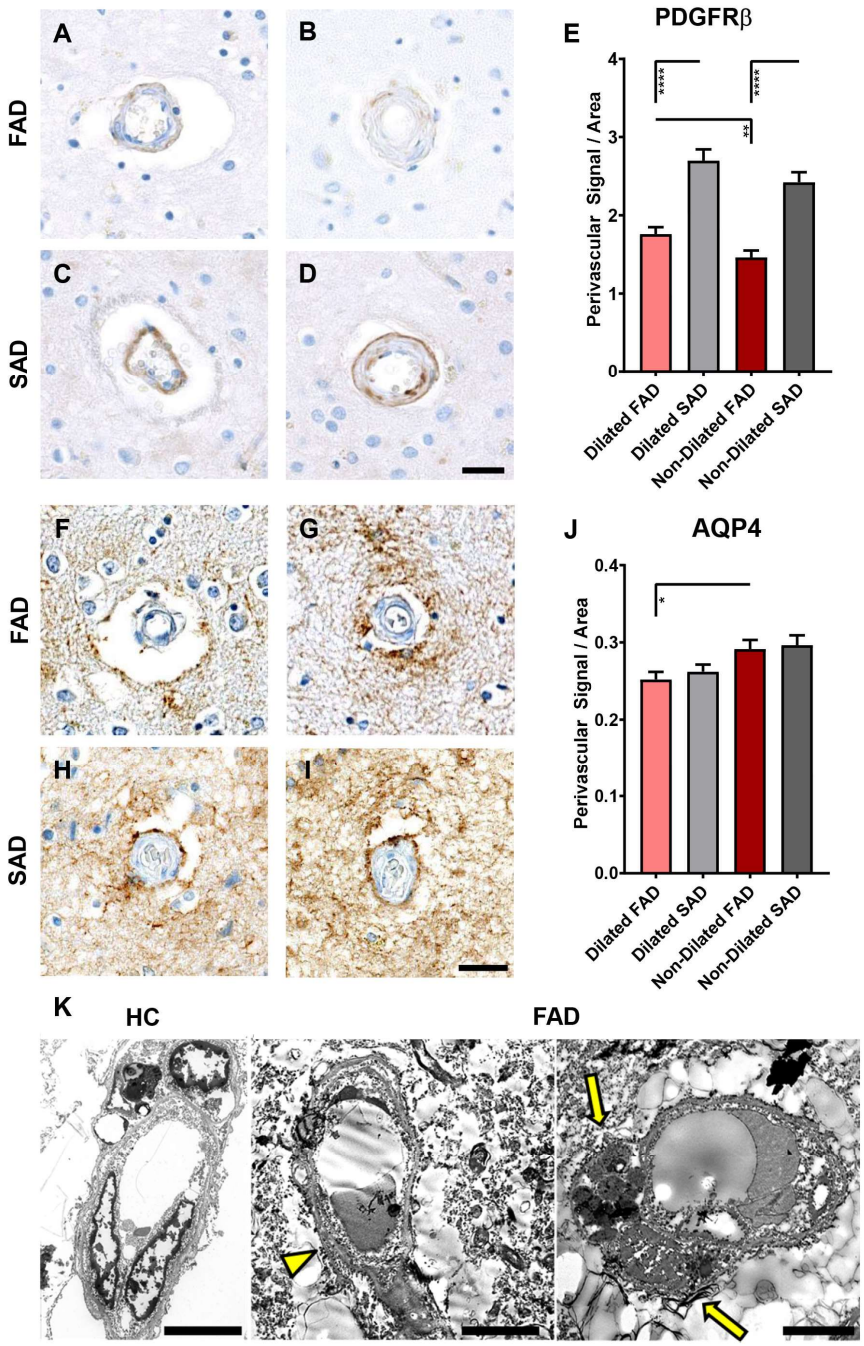

Figure 12: Mural Cell pathology in FAD and SAD. *Representative images of perivascular PDGFRβ immunohistochemistry are shown (Fig. 8A-D), scale bar = 25µm. FAD (n=21) vessels presented with significantly less perivascular PDGFRβ signal than those of SAD (n=10) (p: ****<0.0001). The non-dilated vessels presented with significantly less perivascular PDGFRβ signal than dilated FAD vessels (p: **=0.0024) (Fig. 8E). Representative images are shown for perivascular AQP4 signal in dilated and non-dilated vessels in FAD (Fig. 8F-G) and SAD (Fig. 8H-I), scale bar = 25µm. Dilated FAD Vessels had significantly less perivascular AQP4 immunoreactivity than non-dilated FAD vessels (p =0.0146) (Fig. 8J). Representative EM images are shown for one HC (n=1) and a FAD (n=3) case (Fig. 8K), scale bar = 5µm. In FAD the thickening of basement membrane (yellow arrowhead) and apoptosis of a pericyte (yellow arrows) can be observed.*

Chapter 2: Proteomic heterogeneity in purified vessels from Alzheimer's disease

3.4 Proteomic profile of purified vessels

To assess possible causes of Aβ independent vascular pathology and associated structural changes in the vessels of FAD, the proteomes of purified vessels from the FC of 10 FAD, four SAD and 3 HC, and the occipital cortex of 20 FAD, 10 SAD and six HC cases were analysed. Representative images of isolated vessels in FAD and SAD demonstrate the presence of Aβ plaques in the isolates (Fig. 13A) which were lysed for total vessel proteomics.

In total 5615 proteins were identified. When conducting differentially expressed proteins (DEPs) analyses in purified vessels from the FC and the OC of both, FAD or SAD versus HC, a different number of up- and downregulated proteins were observed (Fig. 13B-E). The top 10 up- and downregulated proteins are shown for all comparisons in the volcano plots of this figure. For example, in FC of FAD (Fig. 13B) and SAD (Fig. 13D) NTN1 and SQSTM1 were upregulated in both groups when compared to HC. Further, DEPs analyses from FC and OC, between FAD and SAD were performed (Fig. 13F, G) identifying different top 10 upregulated proteins for both comparisons. Commonly and uniquely upregulated proteins between the groups were compared.

When FC of FAD or SAD were contrasted versus FC of HC 43 commonly upregulated proteins were found, while 144 uniquely upregulated proteins were found for FAD and 128 for SAD. In the comparison of FC SAD versus FC FAD and FC FAD versus FC HC, 21 commonly upregulated proteins were found, 134 uniquely upregulated proteins for FAD versus HC, and 143 uniquely upregulated proteins for FAD versus SAD were found. When FC SAD was compared to FC HC, 64 commonly upregulated proteins were found. Between all three comparisons only two commonly upregulated proteins were found (Fig. 14A). The common upregulated proteins in FC were PDK2 and PDK3, which are essential pyruvate dehydrogenase kinase isoforms that regulate glycolysis/carbohydrate oxidation and produce metabolites for the electron transport chain and oxidative phosphorylation. The same comparisons were done in the OC of all the groups (Fig. 14B). Six proteins were common between all comparisons in OC and these proteins were GPHN, CTTNBP2, DPP7, NEXN, TAP1, and DSP. GPHN, CTTNBP2, NEXN, and DSP are related to cell junction processes. There were large differences in the number of DEPs in the AD groups versus HC in both cortices, FC and OC.

In order to determine a biological function to the up and downregulated proteins identified via DEPs analyses, a gene set enrichment analysis (GSEA) was run. The GSEA was run for the same DEPs comparisons shown in the volcano plots. When comparing FC of SAD versus HC, the significant biological processes (BPs) are related to nucleotide biosynthetic processes, viral processes, and regulation of cell activation (Fig. 14C). Organelle inner membrane, collagen-containing extracellular matrix and extracellular matrix were the significant cellular compartment (CC) ontology terms in this comparison. There was no significant molecular function (MF) in the comparison of FC SAD and HC.

In the OC of SAD versus HC, Nuclear protein-containing complex showed up as the only CC ontology term and RNA processing as the only BP. These were very generic terms with more than 1200 genes participating. In this comparison less than 30 genes showed up for the terms in which 1200 genes were participating in, which is why no plot was generated.

In FC of FAD versus HC, BPs such as the regulation of cytoskeleton organisation or regulation of actin filament-based processes showed up (Fig. 14D). Further, CC ontology showed collagen-containing extracellular matrix and extracellular matrix as significant. The MFs associated with this comparison were sulphur compound binding and peptidase activity. When comparing OC of FAD versus HC mainly RNA processing showed up as significant BP. CC ontology showed, for example, cell cortex or exocytic vesicles. There were more significant MFs in the OC comparison such as cadherin binding, ubiquitin protein ligase binding, or also sulphur compound binding (Fig. 14E).

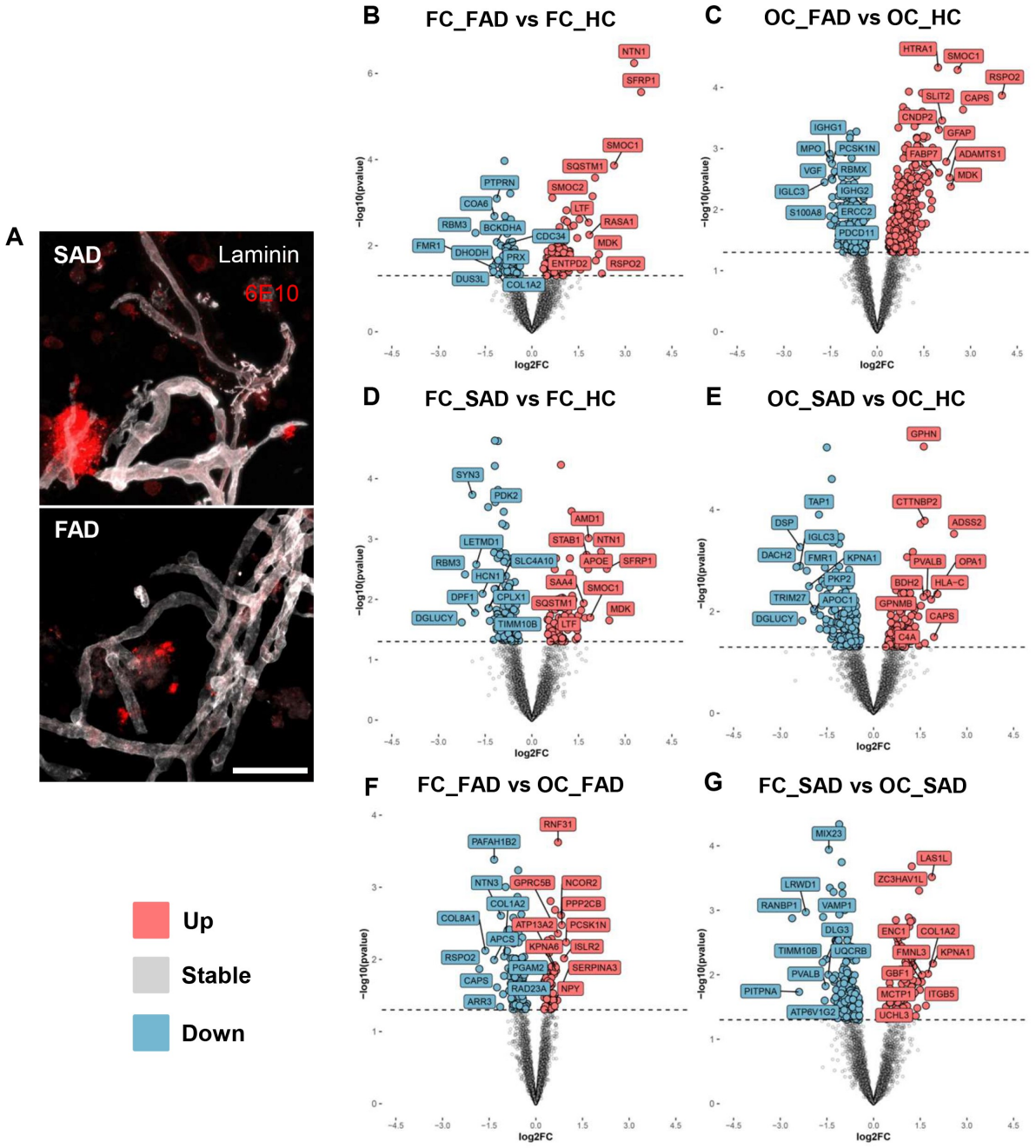

Figure 13: Proteomics of purified vessels. *Representative images of isolated vessels stained for laminin and Aβ (6E10) are shown for SAD and FAD, scale bar = 50µm (A). Volcano plots are shown for differentially expressed proteins (DEPs) for different comparisons; the named proteins were the top 10 up- or downregulated proteins. First, FC between FAD (n=10) and healthy controls (HC) (n=5) (B) and OC comparisons between FAD (n=20) and HC (n=5) are shown (C). Similarly, DEPs were compared for FC (D) (n=4) and OC (E) between SAD (n=5) and HC (n=5). Finally, regional differences within FAD (F) and SAD (G) were evaluated.*

Next, the FC versus OC in FAD and SAD, respectively, were compared. Within FAD, there were three CC ontology terms: collagen-containing extracellular matrix, extracellular matrix, and external encapsulating structure (Fig. 14F), while the nuclear body was the only CC ontology term that showed up in the FC versus OC comparison in SAD (Fig. 14G). The CC ontology terms showing up in FAD are also in the comparison of FC in FAD versus HC. Taken together, the pathology observed in OC of FAD resembled the pathology seen in SAD, while the FC of FAD presented with a more unique proteomic signature. The pathological changes observed in OC were mainly related to RNA processing which was previously shown to be affected[115]. In FC of FAD processes related to arteriogenesis and extracellular remodelling showed up consistently in the comparisons.

Subsequently, a weighted gene co-expression network analysis (WGCNA) was performed to study the relationship between the proteins present in all samples. Three WGCNA were performed, one for FC with 3751 proteins, one for OC with 3859 proteins, and one including only FAD cases with 4102 proteins. The proteins were clustered into modules which are correlated to the groups. The significant modules found for FC and OC from all groups were correlated with sex, age of death (AoD), together with the groups themselves: FAD, SAD, and HC (Fig. 15A). Module 20 (ME20) was significantly positively correlated with sex, and SAD, and significantly negatively correlated with FAD. ME3 was significantly negatively correlated with AoD and contained BPs such as cellular respiration and oxidative phosphorylation. In the CC ontology terms, the mitochondrial membrane protein complex, mitochondrial matrix, and glutamatergic synapse showed up as some of the significant CCs. Significant MFs included, for example, NADH dehydrogenase activity or electron transfer activity (Annex Fig. 2A). ME17 and ME21 were significantly negatively correlated with HC and significantly positively correlated with FAD. ME17 was further significantly negatively correlated with sex. ME17 of the FC WGCNA presented with proteins related to BPs such as regulation and canonical Wnt signalling, and regulation of epithelial cell proliferation. The CC ontology terms were related to lipoprotein particles and extracellular matrix, while the MFs included a variety of binding functions such as extracellular matrix binding, heparin-binding, or sulfur compound binding (Annex Fig. 2B).

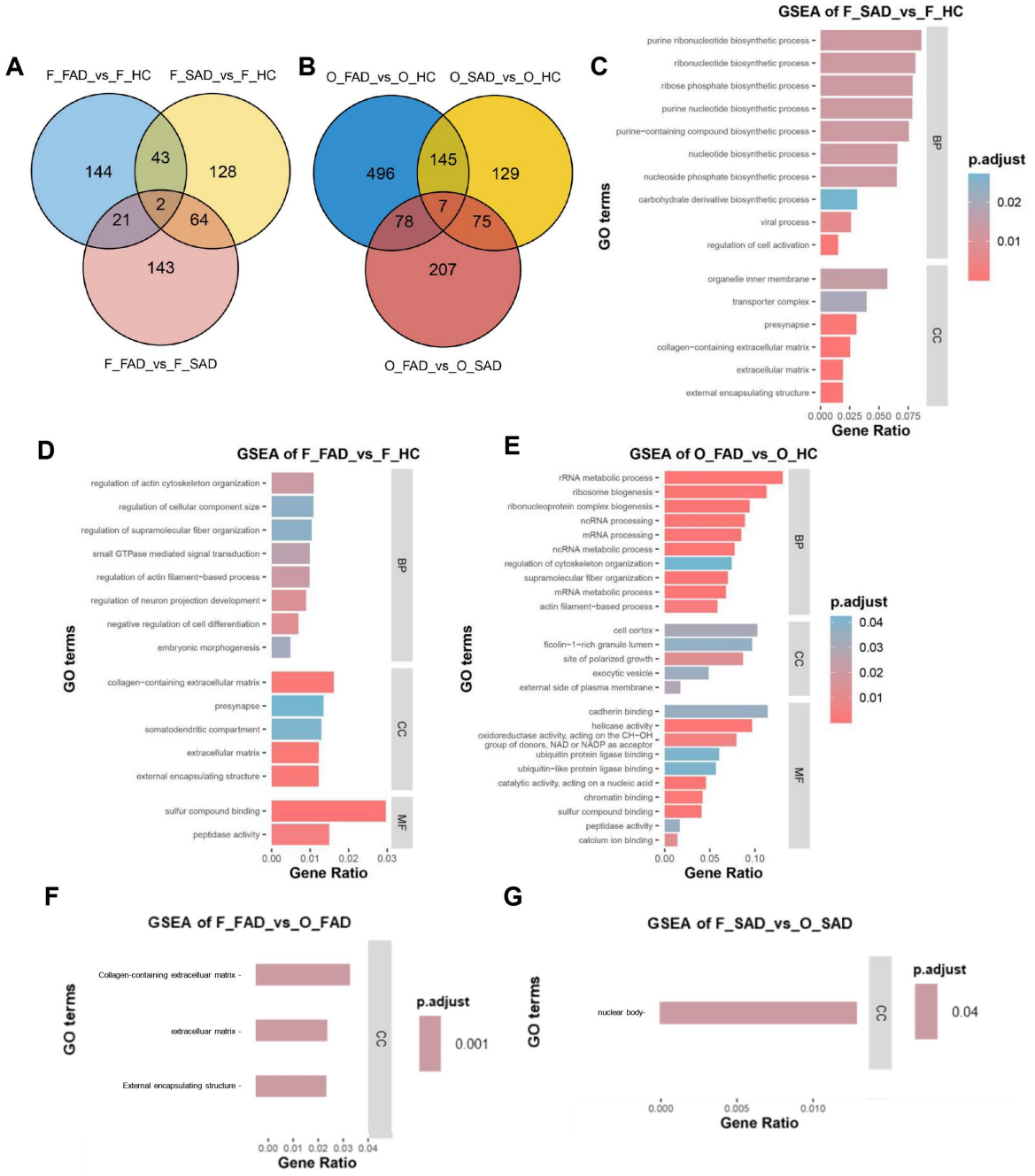

Figure 14: Gene set enrichment analysis (GSEA) in purified vessels. *Venn diagrams are shown for the FC (A) and OC (B) illustrating the common upregulated proteins between FAD, SAD and HC. The GSEA is shown for FC SAD versus HC with the top 10 significant biological processes (BPs) and top six cellular component (CC) ontology terms (C). When comparing the FC of FAD versus HC, there were eight significant BPs, five significant CC ontology terms and two significant molecular functions (D). In the OC of FAD versus HC, there were 10 significant BPs, five significant CC ontology terms and 10 significant MFs (E). Again, FC versus OC in FAD and SAD were evaluated. In FAD there were no significant BPs or MFs between FC and OC but three significant CC ontology terms (F). In SAD only nuclear body showed up as a significant CC ontology term when comparing FC and OC (G).*

ME20 and ME21 were modules with 21 proteins each which did not result in any significant terms or pathways in the analyses. To name some examples, in ME20 proteins were located in the mitochondrion (OPA3) or participating in citrate transport across the inner mitochondria membrane (SLC25A1) or directly related to mitochondrial respiration (COA6). However, the other proteins in this module were related to various cell types and functions, such as regulation of endothelial cell proliferation (EDF1), molecular chaperone of nicotinic acetylcholine receptors (RIC3) or GTP binding activity (ARL15). In ME21 a few proteins were related to the immune response and immune system (IGKV3D-11, MNDA, RFTN1). Two proteins were further involved in axon guidance (SPON1) and the positive regulation of axon extension (ISLR2). Nonetheless, no larger terms could be identified for these two modules.

In OC, ME1 and ME9 have a significant negative correlation with FAD, while both had positive correlations with SAD and HC. ME1 contained significant BPs related to RNA processing and DNA repair. For the CC ontology catalytic step 2 spliceosome or preribosome showed up, and the MFs were related to DNA and mRNA binding (Annex Fig. 3A). ME2 showed a significant positive correlation with FAD and significant negative correlations with sex, AoD, SAD, and HC, as illustrated in Figure 14A. ME2 presented as a mainly structural module with BPs such as synapse organisation, actin filament organisation, and neuron projection morphogenesis. The CC ontology terms were related to the cell cortex, microtubule, and the actin cytoskeleton and significant MFs included cadherin binding and actin filament binding (Annex Fig. 3B).

ME7 correlated significantly positively with FAD and negatively with sex, AoD, SAD, and HC, the latter was significant. This module contained BPs related to morphogenesis and cell migration. Accordingly, in the CC ontology collagen trimer, collagen-containing extracellular matrix and extracellular matrix showed up. The MFs were binding related such as extracellular matrix binding and heparin binding (Annex Fig. 3C).

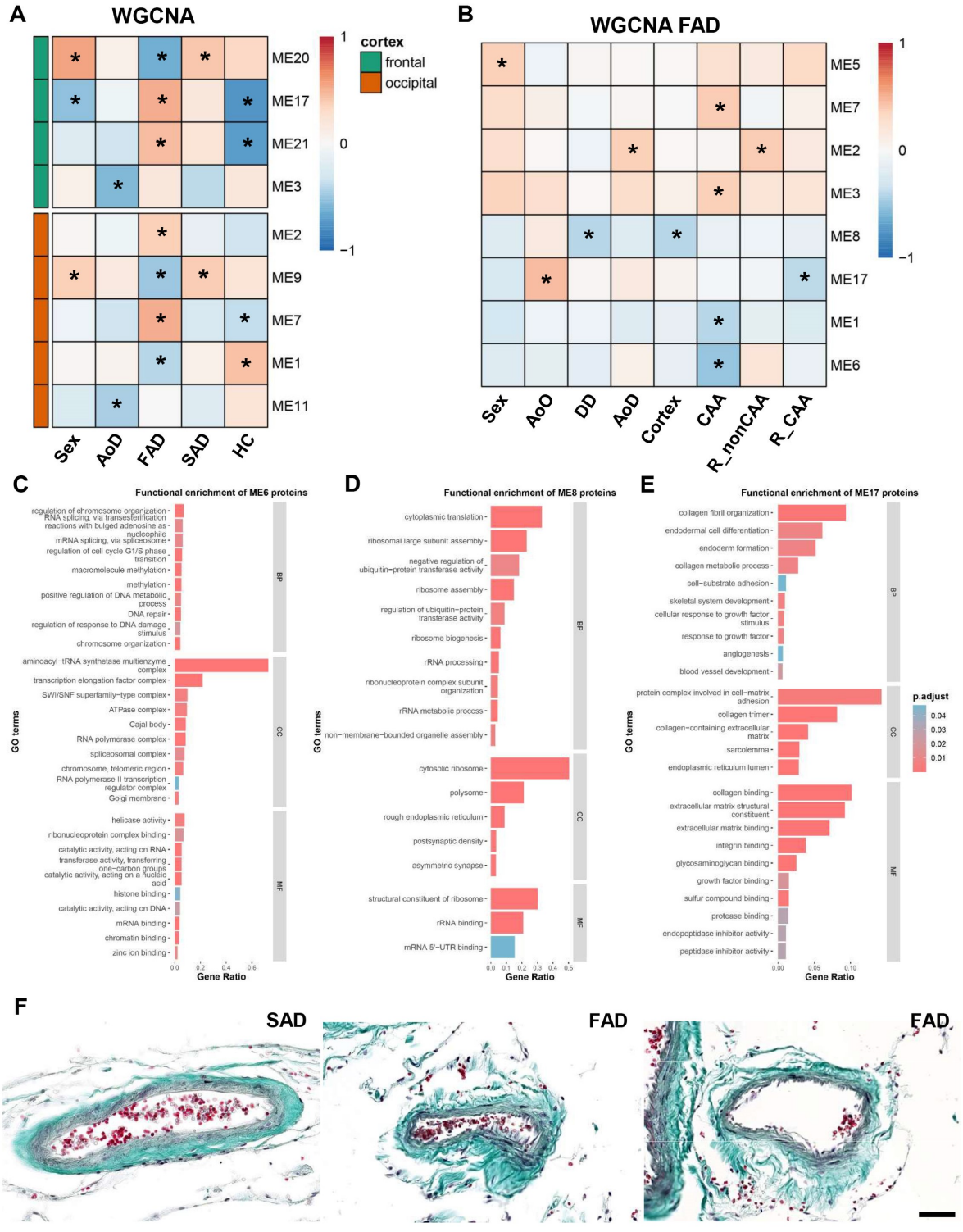

Figure 15: Weighted gene co-expression network analysis (WGCNA) performed for the proteins present in all samples. *The significant modules for FC and OC are shown related to sex, age of death (AoD), FAD, SAD and HC (A). A second WGCNA was performed taking only FC and OC of FAD into account and including features such as sex, age of onset (AoO), disease duration (DD), AoD, cortex, cerebral amyloid angiopathy VCING score (CAA), the*

ratio of perivascular dilatation to vessel calibre size for nonCAA vessels (R_nonCAA) and CAA (R_CAA) vessels. The significant modules are shown (B). Next, functional enrichment analyses were performed on the genes clustered in the formed modules. Module 6 (ME6) from the WGCNA only taking FAD into account (B) was negatively correlated to CAA and revealed RNA and DNA processing (C). ME8 was negatively correlated to DD and the cortex and was related to ribosomal activity and RNA processing (D). ME17 was significantly positively correlated with AoO and negatively with R_CAA. The functional enrichment of ME17 showed BPs, CCs, and MFs related to collagen and angiogenesis (E). Additionally, representative images of a Masson's Goldner stain is shown, illustrating the disorganisation of collagen in meningeal vessels in FAD, scale bar = 50µm (F).

ME9 exhibited a significant negative correlation with FAD, while being negatively correlated to sex and SAD, also significantly. ME9 presented with the regulation of response to ER stress and protein folding as the top two significant BPS and pigment granule and melanosome as the top two significant CC ontology terms. The MFs were protein disulphide isomerase activity or intramolecular oxidoreductase activity (Annex Fig. 3D). ME11 was only significantly negatively correlated to AoD while being negatively correlated to sex, FAD, and SAD, the correlation with HC was positive. The significant BP with the highest gene ratio was collagen fibre organisation in ME11 with CC ontology terms such as collagen trimer and collagen-containing extracellular matrix. The significant MFs were collagen binding, extracellular matrix structural constituent, and extracellular matrix binding (Annex Fig. 3E). These results underlined the heterogeneity of molecular and cellular mechanisms involved in vascular pathology of both AD variants.

Previously, we have identified a degree of pathological heterogeneity in PSEN1 E280A FAD cases, both in general[34] and specifically for vascular pathology[38,36]. To gain more insight into the disparities between FC and OC in biological terms within the FAD group, a Weighted Gene Co-Expression Network Analysis (WGCNA) was carried out exclusively using all FAD samples, including both FC and OC, along with all valid proteins specific to these groups. 3751 and 3589 proteins were used for the FC and OC networks, respectively.

The resulting modules were correlated to sex, age of onset (AoO), DD, AoD, cortex, CAA, the ratio of PVS in nonCAA vessels (R_nonCAA), and the ratio of PVS in CAA vessels (R_CAA) (Fig. 15B). ME1 was found to be significantly negative correlated to CAA, and it was related to RNA and DNA processing (Annex Fig. 4A). ME2 was significantly positively correlated with AoD and R_nonCAA. The significant BPs included vesicle-mediated transport, endosomal transport, and protein folding. The CC ontology terms were related to vesicle tethering complex, trans-Golgi network, and endocytic vesicle. The MFs were related to GTPase binding and guanyl nucleotide binding (Annex Fig. 4B).

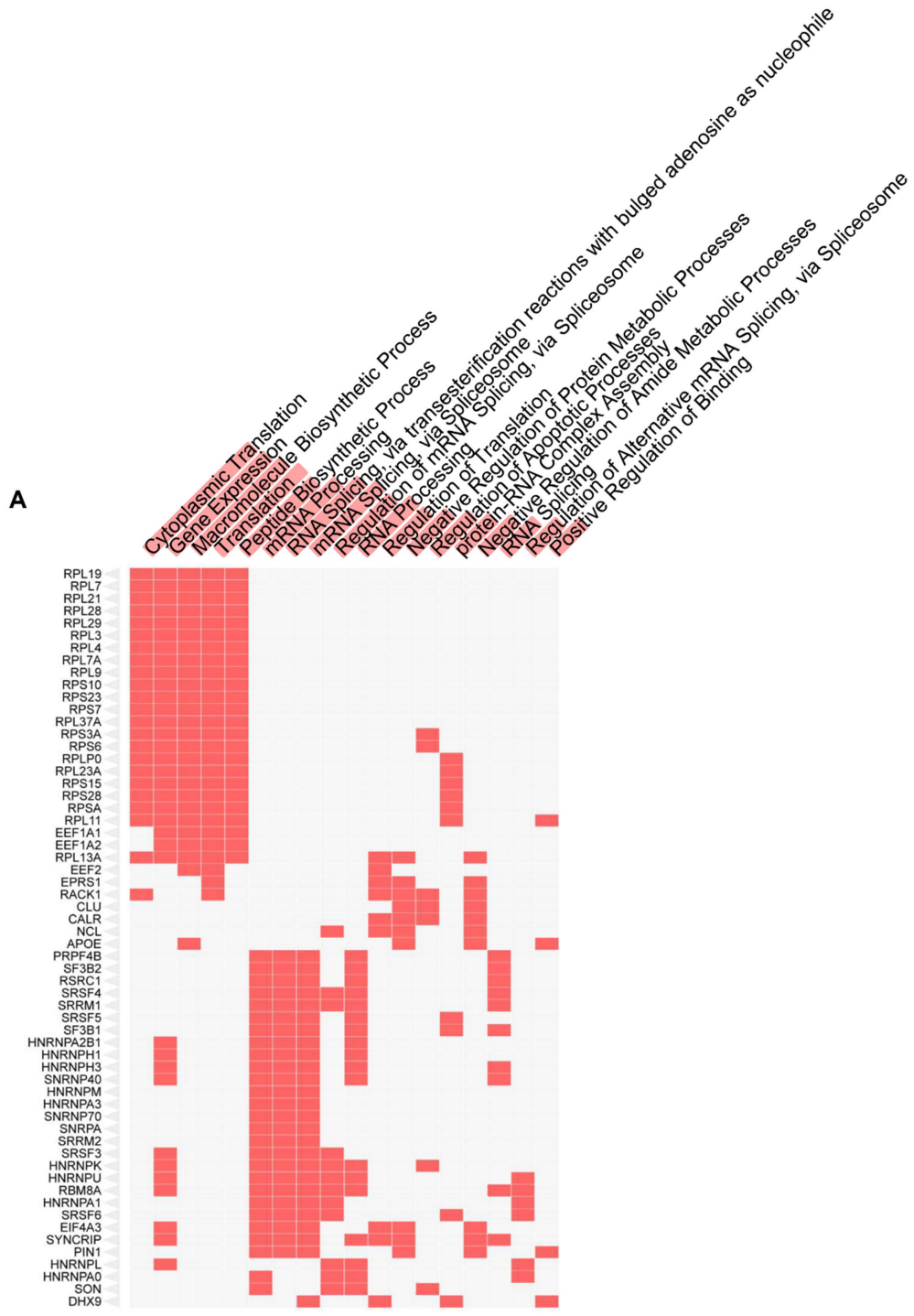

Figure 16: Peptides co-immunoprecipitated with Aβ. *A clustergram illustrating the top 20 biological processes and top 60 associated proteins from the peptides co-immunoprecipitated with Aβ (A).*

ME3 was significantly positively correlated to CAA. The BPs of this module were related to structural processes such as the regulation of supramolecular fibre organisation and actin filament organisation. The significant CC ontology terms were ficolin-1-rich granule lumen, ficolin-1-rich granule, and cell cortex. Ficolin-1 is synthesised in monocytes and was shown to be present in secretory granules of human neutrophils[116]. The MFs were fatty acid binding and actin filament binding (Annex Fig. 4C). ME5 was significantly positively correlated with sex. The BPs, CC ontology and MFs of ME5 were related to ATP metabolism (Annex Fig. 4D). ME7 had a significant positive correlation to CAA. The BPs of this module were related to different catabolic processes, the CC ontology, included proteasome core complex, vacuolar lumen, and vesicle lumen. In the MFs NAD binding and antioxidant activity showed up as significant (Annex Fig. 4E).

ME6 was significantly negatively correlated to CAA. The functional enrichment of ME6 showed terms related to RNA and DNA processing (Fig. 15C). ME8 was significantly negatively correlated with DD and cortex with the proteins related to RNA processing and ribosome assembly (Fig. 15D). ME17 was interesting as it was significantly positively correlated to AoO and significantly negatively correlated to the PVS ratio of CAA-affected vessels. This module contained mainly processes related to extracellular remodelling such as collagen fibre organisation, angiogenesis, and blood vessel development. The significant CC ontology terms for ME17 were with collagen trimer, collagen-containing extracellular matrix, and protein complex involved in cell-matrix adhesion (Fig. 15E). Extracellular matrix related proteins were already identified in the DEPs and GSEA analyses involving FC from FAD cases (Fig. 14). Specifically, it was the only outstanding difference between FC and OC cortices in FAD.

As validation of this observation, a Masson Goldner staining in AD cases, revealed collagen disorganisation in the meninges of FAD, while SAD meninges were intact (Fig. 15F). With this staining collagens and bones are stained blue, while keratin and muscle fibres would be stained red. Changes in collagen IV have been previously associated with fragility of blood vessels[9] and cerebral capillaries with Aβ deposits were shown to express more fibrillary collagen III and IV[54]. Accumulation of collagen IV was further associated with dysregulation of the basement membrane[54] and this disorganisation was shown with the Masson Goldner stain for meningeal vessels.

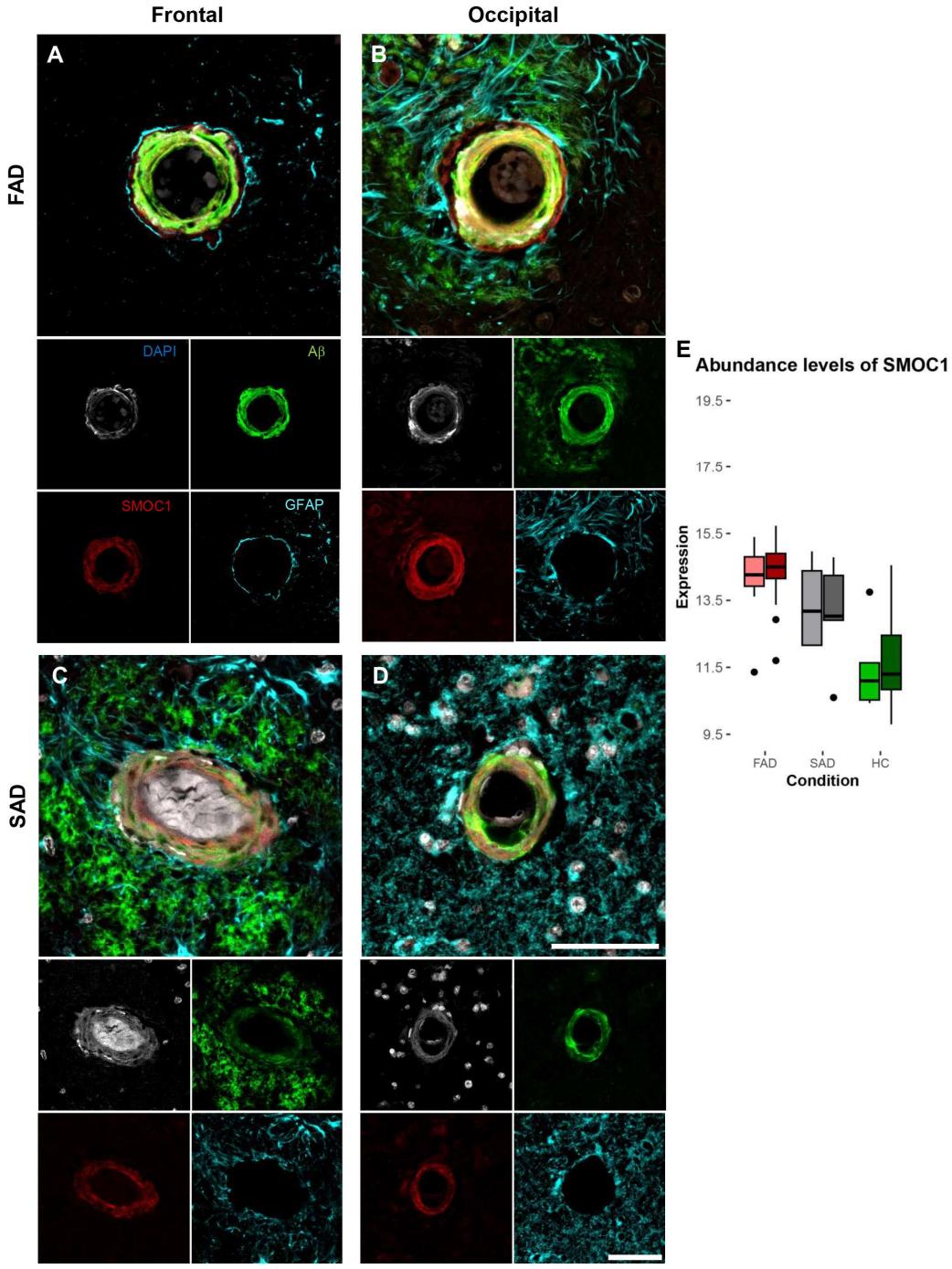

Figure 17: SMOC1 immunofluorescence in FAD and SAD. *Representative images are shown for 50 um caliber vessels of the FC and OC in FAD and SAD (n=3). Sections were stained for DAPI, Aβ, SMOC1 and GFAP, scale bar = 50μm. In FC FAD, there was SMOC1 in the vessel wall (A). In the OC of FAD SMOC1 staining could be observed within the vessel wall and in the surrounding plaque (B). Similarly, in the FC of SAD SMOC1 signal is restricted to the vessel wall (C). In the OC of SAD SMOC1 signal was observed in the vessel wall and in the plaque*

(D). There were no significant differences in SMOC1 abundance in the proteomic analysis between FAD and SAD (E).

The majority of modules resulting from the WGCNA were significantly correlated with CAA and these modules presented with processes related to DNA and RNA processing, catabolic processes and actin filament binding. There is the possibility that the DNA/RNA proteins identified are co-aggregating together with Aβ deposits in the parenchyma or the vascular tissue of AD patients[117,118]. In order to determine whether there are actual functional differences in purified vessels concerning DNA/RNA processing, or whether these proteins are being co-immunoprecipitated with Aβ, the peptides that co-immunoprecipitated with Aβ were analysed. A clustergram illustrating the top 20 enriched terms and top 60 associated genes is shown in figure 16A. Among the top 20 enriched terms there are mRNA processing, mRNA and RNA splicing, RNA processing and regulation of mRNA processing (Fig. 16A). This suggests that at least some proteins related to DNA and RNA processing could be co-aggregating with Aβ, or being trapped in Aβ vascular deposits. This cannot be determined as a certainty with the data obtained here, and further mechanistic studies in murine or cellular models are needed to clarify it. However, this observation is useful to ascertain which molecular processes can be distinctive for each AD variant. For instance, OC was the region that showed higher number of DEPs. Once, FAD exclusive DEPs are selected, and subtracting those that were shown to co-aggregate together with Aβ peptides, it is possible to identify affected processes and pathways exclusive for FAD (Annex Fig. 5A, B). Among those, RNA regulation and processing, RNA splicing and cytoskeleton remodelling biological processes were included, together with glycogenesis-related pathways (Annex Fig. 5C, D).

Finally, to validate the proteomics findings involving other processes, different markers were selected for immunofluorescence. Secreted modular calcium-binding protein 1 (SMOC1) was chosen because it had been identified in other proteomic studies[119,120] before and was shown to colocalise with Aβ plaques and CAA. Further, SMOC1 plays a role in glucose homeostasis and is a promotor for endothelial cell proliferation and angiogenesis[121]. There was more intense SMOC1 immunoreactivity in the small calibre vessels of FAD when compared to SAD (Fig. 17A-D) but there was only little staining coinciding with the Aβ plaques (Fig. 17B, C). In the proteomics of purified vessels, SMOC1 was more abundant in FAD but the difference was not significant between FAD and SAD (Fig. 17E).

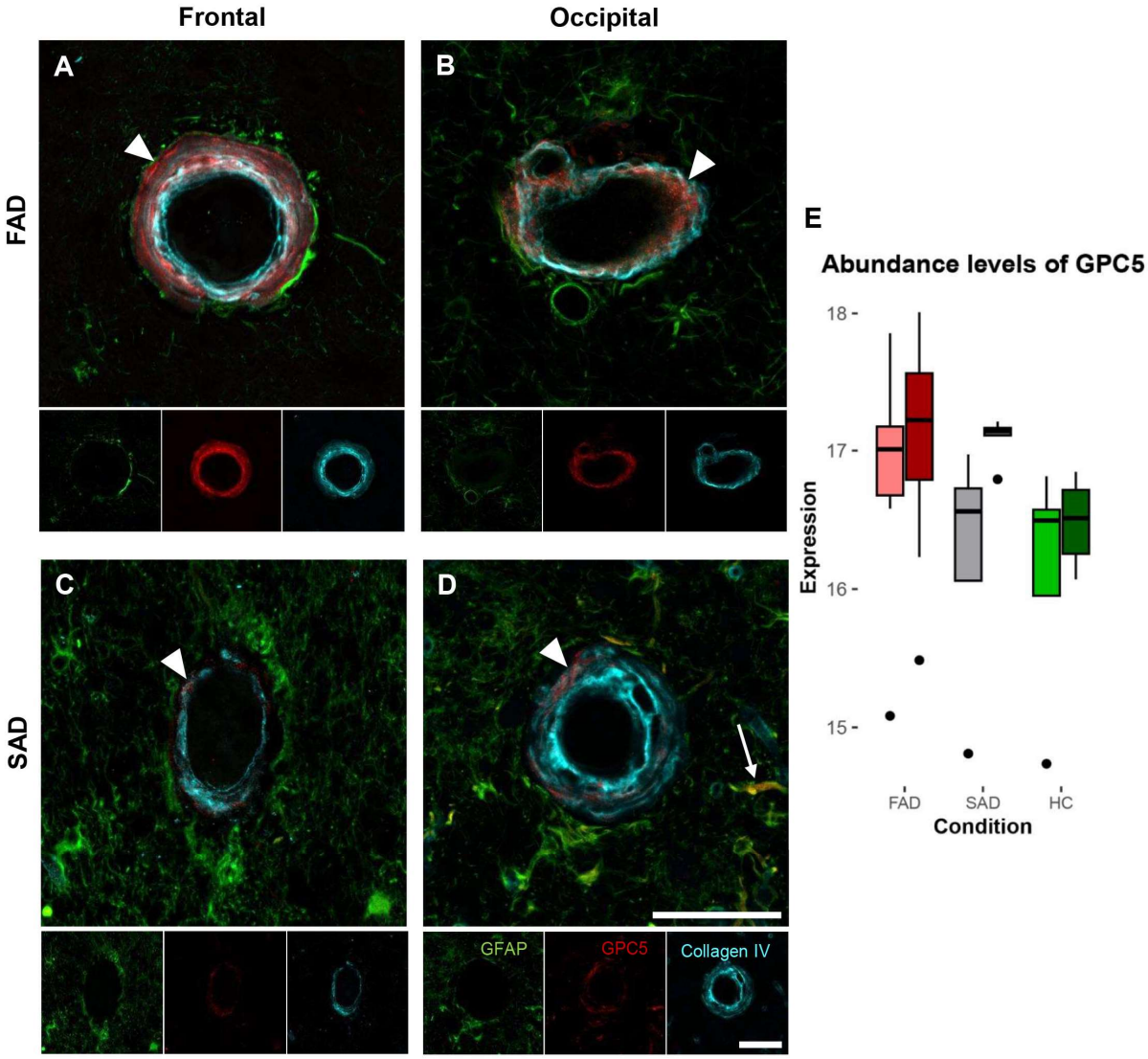

Figure 18: Glypican-5 in vessels of FAD and SAD. *Representative images for glypican-5 (GPC5) are shown for the FC and OC in FAD and SAD (n=3), scale bar 50µm. In the FC of FAD (A) and OC of FAD (B) GPC5 signal was observed in within the vessel wall. In the FC of SAD (C) there was no GPC5 signal in the vessel wall. But in the OC of SAD there was GPC5 signal (D). GPC5 abundance levels did not differ in the proteomics between FAD and SAD but the FC of SAD presented with less (E).*

Next, to evaluate the ECM different glycoproteins were considered. Glypican-5 (GPC5)[119] and tenascin-c (TNC)[122] were selected as they were shown to be produced by astrocytes and versican (VCAN) was shown to be produced by endothelial cells[75]. In FAD in FC and OC, collagen IV and GPC5 were found to accumulate in the vessel wall (white arrowheads, Fig. 18A, B). In SAD no GPC5 accumulation could be found in FC (white arrowhead, Fig. 18C) and some GPC5 signal in OC vessels (Fig. 18D).

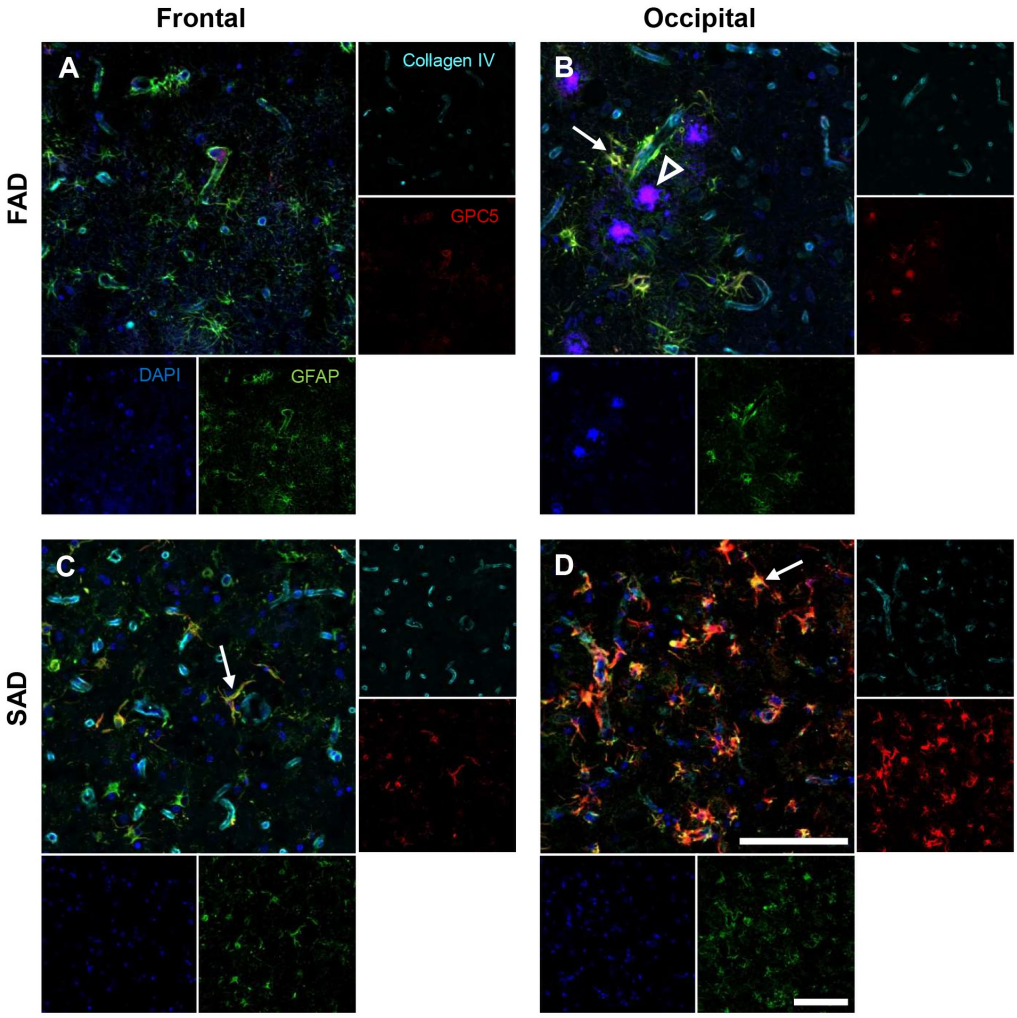

Figure 19: Glypican-5 signal in astrocytes of FAD and SAD. *Interestingly, GPC5 could not be observed in astrocytes in the FC (A). In the OC of FAD (B) there was little colocalisation between GPC5 and GFAP (white arrow), scale bar = 100µm. In the OC of FAD plaques stained by DAPI contained GPC5 signal (white arrowhead). In the FC of SAD, GPC5 signal colocalised more with GFAP (white arrow) but not as abundantly as in the OC of SAD (D).*

These findings were confirmed with the proteomic analysis of the isolated vessels, in which more GPC5 was found in FAD than SAD, but SAD OC levels were similar to FAD (Fig. 18E). However, in OC of SAD colocalisation of GPC5 and GFAP can be observed (white arrow, Fig, 18D). This colocalisation became more evident by taking lower magnification images. There is no overlap of GPC5 and GFAP signal in FC of FAD (Fig. 19A) while there are some astrocytes expressing GPC5 in the OC of FAD (white arrow, Fig. 19B). Additionally, GPC5 was found in plaques in the OC of FAD (empty, white arrowhead, Fig. 19B). The plaques were not directly stained for, but could be clearly identified in the DAPI staining, as well as CAA can be partially

visualised with DAPI (Fig. 17A, B). In SAD both in FC (white arrow, Fig. 19C) and OC (white arrow, Fig. 19D) astrocytes express GPC5 while this was more abundant in OC than FC.

TNC was evaluated in one FAD and one SAD case to confirm the proteomic findings. TNC was abundantly present in both cortices of FAD (Fig. 20A, B) and SAD (Fig. 20C, D) but in the FC of SAD the staining became more cell-shape (white arrowhead, Fig. 20C). The levels of TNC in the proteomic analysis did not differ between FAD and SAD (Fig. 20E), which was confirmed with the images. The same cases were stained for VCAN, and a similarly abundant signal was found for VCAN in FAD (Fig. 21A, B) and in SAD (Fig. 21C, D), but there was no signal in areas that were collagen IV positive. In the proteomic analysis of purified vessels, there was no difference between FAD and SAD in the abundance of VCAN, which became evident with the staining (Fig. 21E).

Taken together, the WGCNA highlighted different protein profiles associated with FAD, SAD, and HC. In comparison with HC and SAD, FAD presented with angiogenic processes in FC

RNA processing was shown to be different between FC and OC of FAD. In summary, the proteomic analyses of purified vessels demonstrated heterogeneous protein expressions in the groups. Moreover, OC of FAD patients presented with a more pathological proteomics signature related to RNA processing, while the FC presented with a more reactive profile. The validation staining demonstrated GPC5 expression within the vessel wall in FAD and within astrocytes in SAD. Basement membrane changes in the form of thickened walls with collagen IV and GPC5 accumulation in FAD. However, there were no differences in the glycoproteins VCAN and TNC.

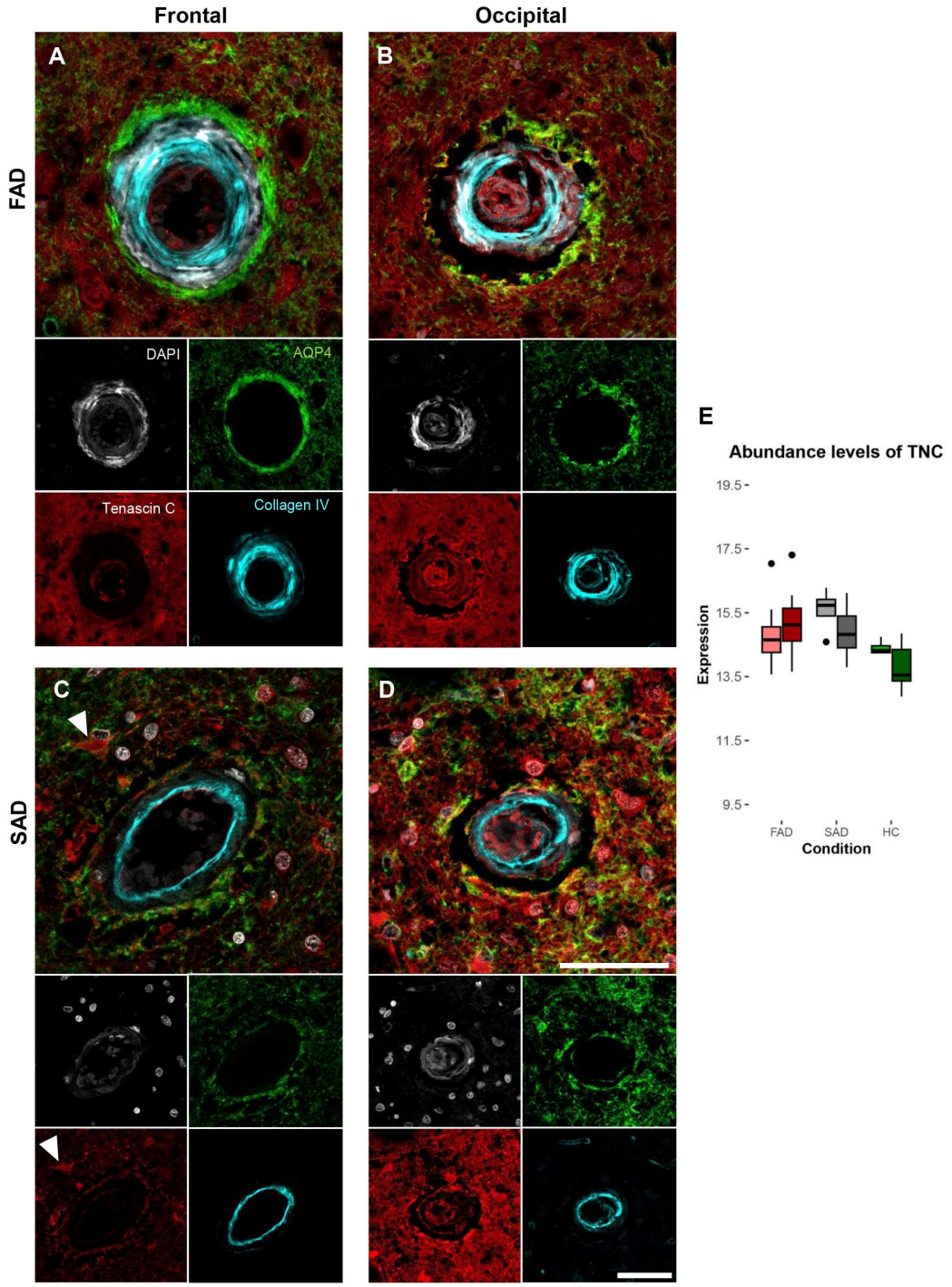

Figure 20: Tenascin-C in FAD and SAD vessels. *DAPI, aquaporin-4 (AQP4), tenascin C (TNC) and collagen IV were stained in FAD and SAD FC and OC sections (n=1), scale bar = 50µm. In FAD the FC (A) and OC (B) did not present differently in the TNC staining. In the FC of SAD, TNC was localised in astrocytes (white arrowheads) (C). In the OC of SAD TNC distributed everywhere (D) as in FAD. The abundance levels of TNC in the proteomics of purified vessels did not differ between FAD and SAD but the FC of SAD had the highest abundance (E).*

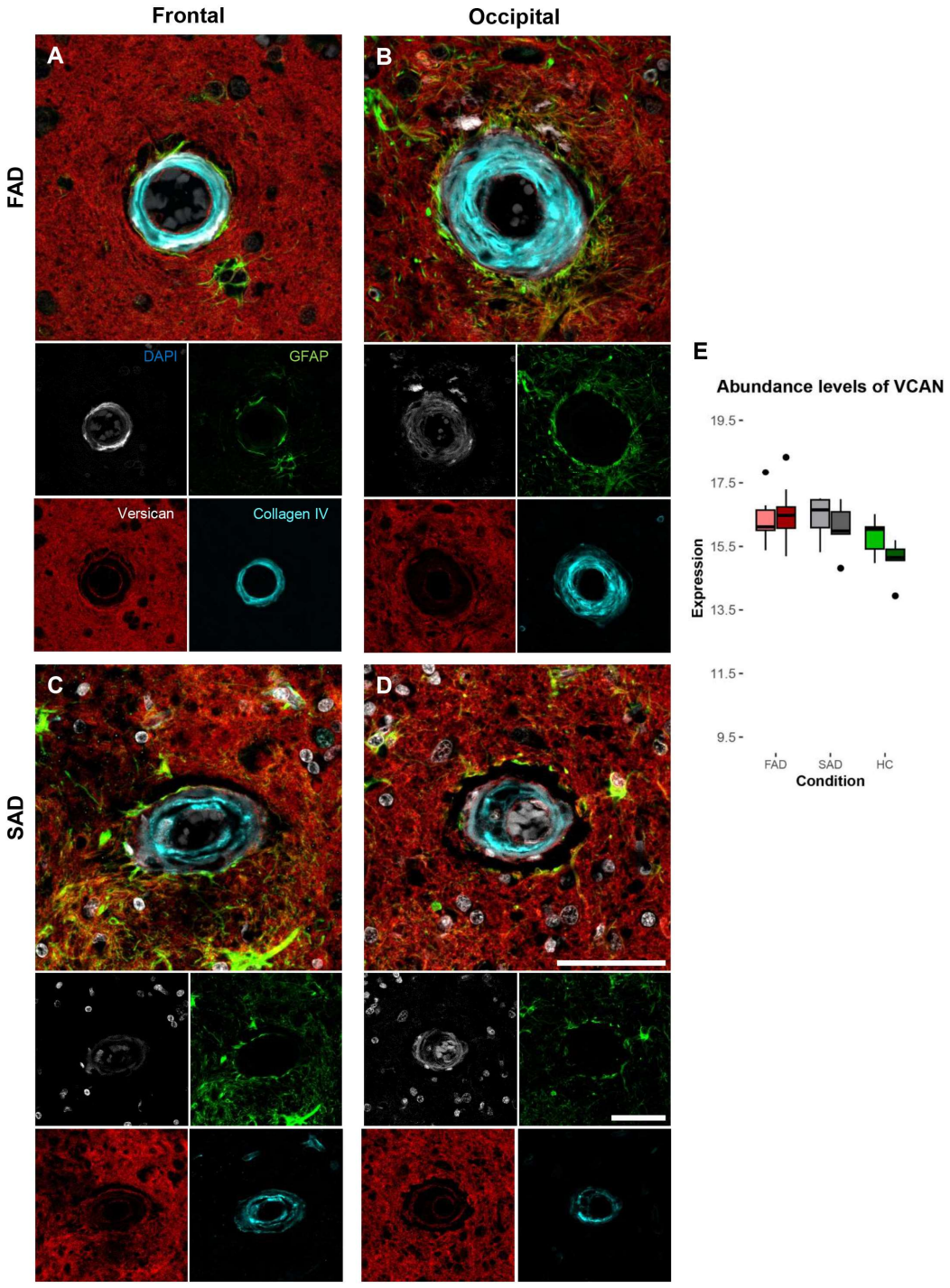

Figure 21: Versican distribution around vessels in FAD and SAD. *FC and OC of FAD and SAD (n=1) were stained for DAPI, GFAP, Versican (VCAN) and collagen IV, scale bar = 50µm. In FAD in the FC (A) and OC (B) VCAN is distributed without clear cellular localisation. There is no VCAN accumulation in the vessel wall in FAD or in the FC (C) or OC (D) in SAD. The abundance levels of VCAN in the purified vessels did not differ between FAD and SAD (E).*

3.5 phosphoTau proteomics

Previous work had demonstrated lower levels of tau pathology in the FC of FAD individuals measured by AT8[34], the diagnostic marker to evaluate post-mortem tau pathology for an AD diagnosis. Paraffin sections from FC and OC of 10 FAD and 5 SAD were stained for AT8 (Fig. 22A-D) and the signal intensity was measured. FAD presented with significantly less AT8 immunoreactivity in FC and OC in comparison to SAD (Fig. 22E). There was no significant difference in AT8 signal between FC and OC in SAD, but the OC of SAD presented with significantly more AT8 signal than the OC of FAD (Fig. 22E).

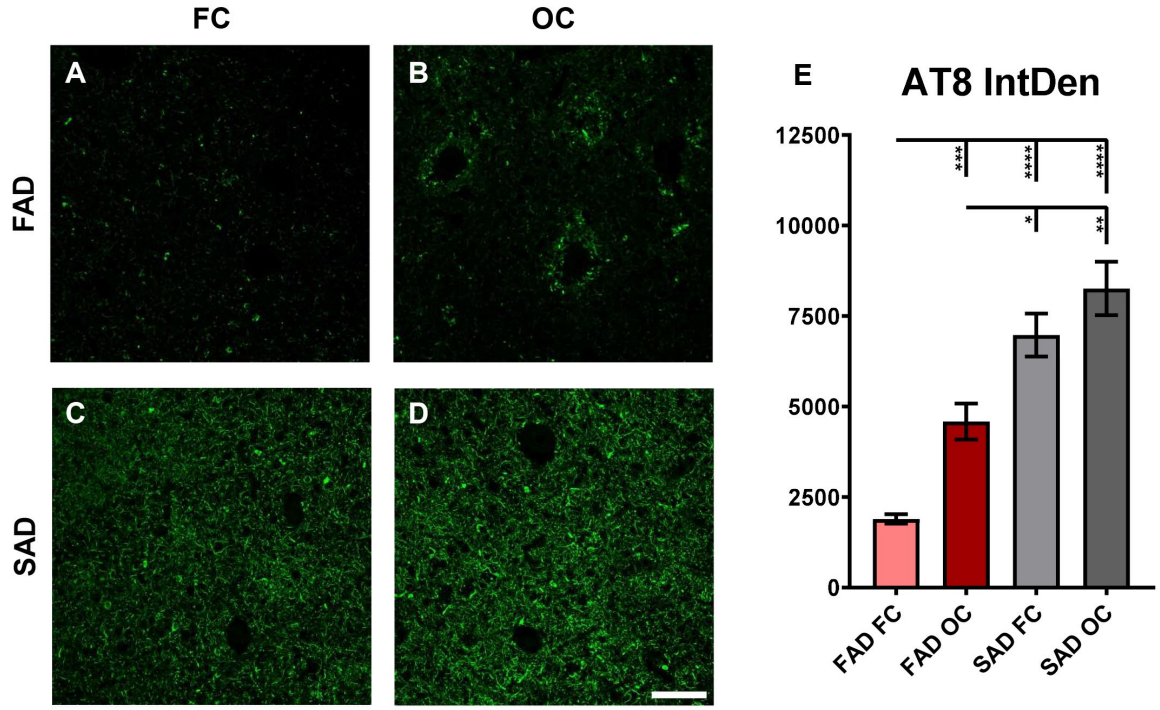

Figure 22: Tau pathology in FAD and SAD. *FC and OC of FAD and SAD were stained with AT8, the diagnostic marker for tau pathology. The FC of FAD (n=10) (A) presented with a neuropil threads and a low number of tangles. In the OC of FAD (n=10) (B) there are neuropil threads and tangles detected by AT8. In the FC of SAD (n=5) (C) and OC of SAD (n=5) (D) a high number of neuropil threads and tangles were detected. In total there was significantly more AT8 signal in SAD versus FAD. In both AD groups the OC presented with more signal intensity than the FC (E).*

In order to identify if other phosphorylations might differ between FAD and SAD and in the interest of identifying whether the changes in vessel proteomes were related to tau, phosphoTau proteomics was performed. This analysis provided information about the whole phospho proteome but for the frame of this work, only the tau phospho proteome was analysed.

From the dataset, across all batches, 21594 phosphopeptides with at least one confident phosphosite were identified. Out of the 21594 phosphopeptides, 339 were related to MAPT and 114 were unique tau phosphosites. The distribution of the phosphosites was illustrated along the 2N4R tau isoform for FC (Fig. 23A) and OC (Fig. 23B). The differences between FAD and SAD in FC and OC were highlighted by green stars. To gain more insight, all MAPT phosphosites were clustered into heatmaps (Fig. 23C) in which the HC distinctively clustered apart from the AD groups.

When FAD and SAD were compared with HC, FAD presented with a higher amount of phosphorylations. Thus, almost all phosphosites were present at a higher level in the phospho-proteome, but when tau pathology is evaluated immunohistochemically, FAD presented with significantly less AT8 signal, demonstrating that AT8 only visualised a small frame of tau pathology (Fig. 4, Fig. 22) and it does not reflect the whole extent of pathology in both AD variants. Alternatively, tau phospho-proteome can be used to predict specific kinase activity patterns involved in the generation of a particular tau phospho-proteome profile. As it was expected, the HC had lower predicted kinase activity in the FC (Fig. 24A) and OC (Fig. 24B), than both AD groups. The FAD cases mostly clustered together with high activities, and some SAD cases were clustered between FAD cases in the FC, while all FAD cases clearly clustered together with higher predicted kinase activity in the OC. The predicted kinase activity granted a clearer view on the phosphorylation status in FAD and SAD, with high kinase activity in FAD becoming evident. Additionally, the kinase activity was clustered in accordance with their family, for example, CAMK2 (Ca2+/calmodulin-dependent protein kinase II), and group, for example, CK1 (Cell kinase 1) and a ratio between FC and OC in FAD was plotted. This ratio was calculated for the phosphosites present in FC and OC (Fig. 24C). There were four kinases more active in the FC than OC in FAD (CSNK1D, CHEK1, GSK3B, and PRKCZ) while others (RPS6KB1, CAMK2A, PRKACA, PRKCI, MAPK13, PRKCA, and PRKAA1) were more

active in the OC. Interestingly; PRKAA1 was more active for phosphosites T217 and T231 in FC.

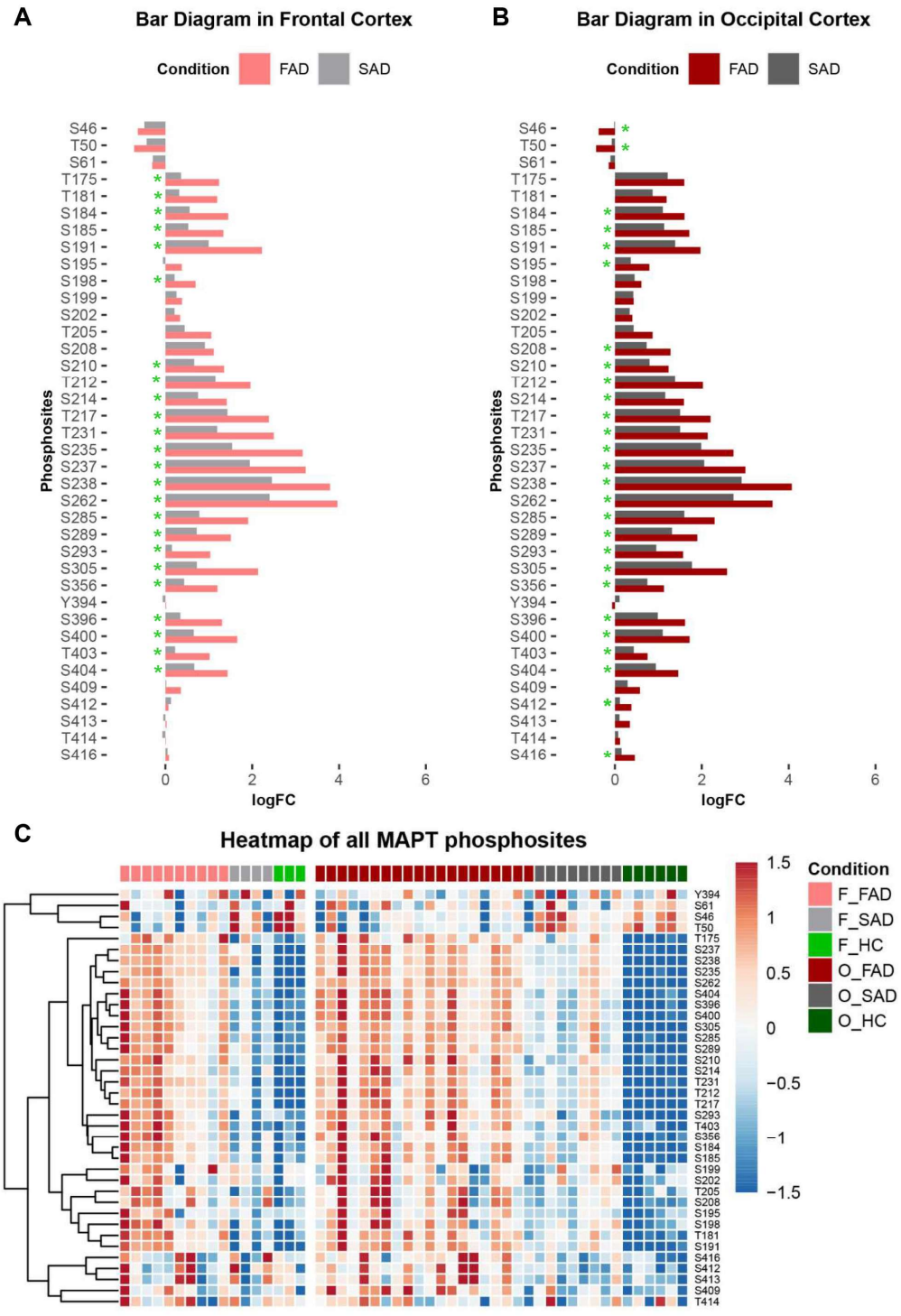

Figure 23: Phospho Tau Proteomics in FAD, SAD and HC. *The phosphosites were mapped along the 2N4R tau isoform for the FC (A) and OC (B). The log fold changes are shown for FAD (FC n=10, OC n=20) versus HC (FC n=3, OC n=6) and SAD (FC n=4, OC n=8) versus HC but the significances are shown for FAD versus SAD in FC and OC respectively. Next, the phosphosites were clustered into heatmaps and the HC cluster distinctively away from the AD groups (C).*

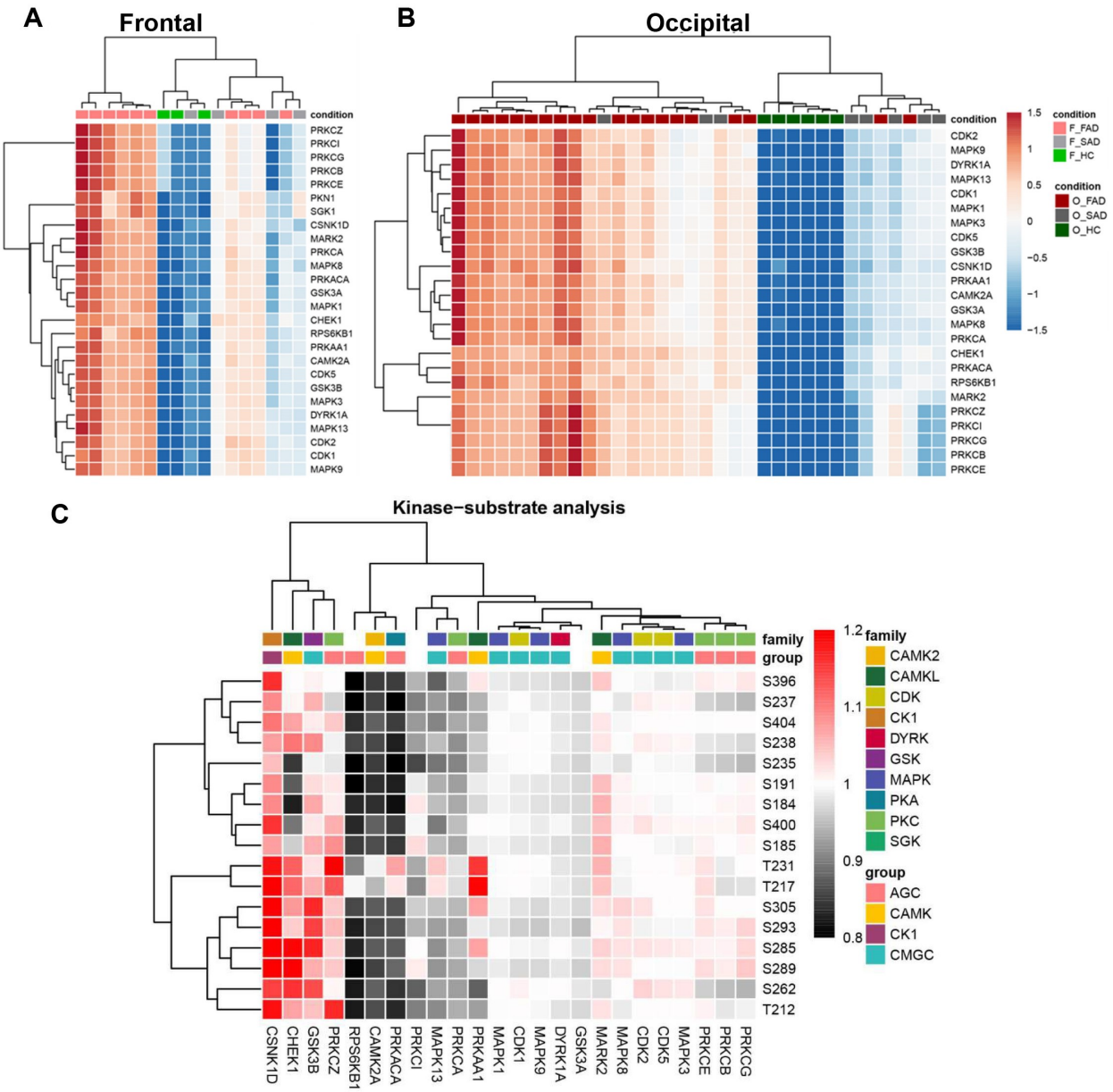

Figure 24: Predicted kinase activity in FAD, SAD and HC. *Based on the phospho proteome the kinase activity was predicted. In FC of FAD (n=10) (A) and HC (n=3) separate noticeable in the predicted kinase activity. Similarly, in OC, FAD (n=20) and HC (n=6) separated from each other. In the FC the SAD (n=4) and in the OC of SAD (n=8) cases present with less predicted kinase activity than FAD. A kinase-substrate analysis was performed for the FAD cases for which FC and OC data was available. The ratio of kinase activity for the specific phosphosite was calculated for FC minus OC. For all phosphosites, the kinases CSNK1D, CHEK1, GSK3B and PRKCZ were more activated in FC than OC. The kinases RPS6KB1, CAMK2A, PRKACA, MAPK13 and PRKCA were more activated in the OC for most phosphosites. A majority of kinases did not differ in their activity between FC and OC (C).*

To summarise there was significantly less AT8 signal in FAD compared to SAD, while there was more overall tau phosphorylation and higher predicted kinase activity in FAD. A previous study has shown the association of specific tau phosphorylations to the disease progression of AD. Tau PTMs were postulated to begin with c-terminal cleavage and negatively charged phosphorylation in proline-rich region (PRR). Next, within the microtubule-binding region, acetylation and ubiquitination participated in tau fibril formation advancing AD progression[17]. AT8 (S202/T205) is a well-established marker for the diagnosis of AD; however, when trying to identify specific mechanisms related to tau pathology, a more detailed look is needed. In order to do so, and as a validation of phospho-proteomic findings, FC and OC of 10 FAD and 5 SAD cases were stained for T231, T217, and T205 phosphorylations which are all located in the PRR domain of tau. T231 was previously associated with a non-demented disease state, T217 with early tau pathology, and T205 with progressed tau pathology[17]. In the general phospho-proteome T205, T217, and T231 were significantly more abundant in FC and OC in FAD versus SAD (Fig. 23A, B). Density was chosen instead of signal intensity for assessing differences between groups because the signal can vary between different types of tau deposits and the goal was to evaluate structural differences for tau deposits. These structural differences can be observed in staining different parts of the tangle or the neuropil, and the general amount of tau deposits. There was more staining of T231, T217, and T205 in FAD compared to SAD (Fig. 25A-D). In the FC of FAD T231 localised in a different part of the tangles than T217 and T205 (arrowhead, Fig. 25A-C) while S202/T205 did not stain one of the highlighted tangles (arrowhead, Fig. 25D) but does stain neuropil threads not present in the other phosphorylations (arrow, Fig. 25A-D). In general, there was significantly more T231, T217, and T205 in both cortices in FAD than in SAD. In FAD, there was significantly more T231, T217, and T205 than S202/T205 in FC and OC, while in SAD, the density increased from staining for T231 to S202/T205 (Fig. 25E).

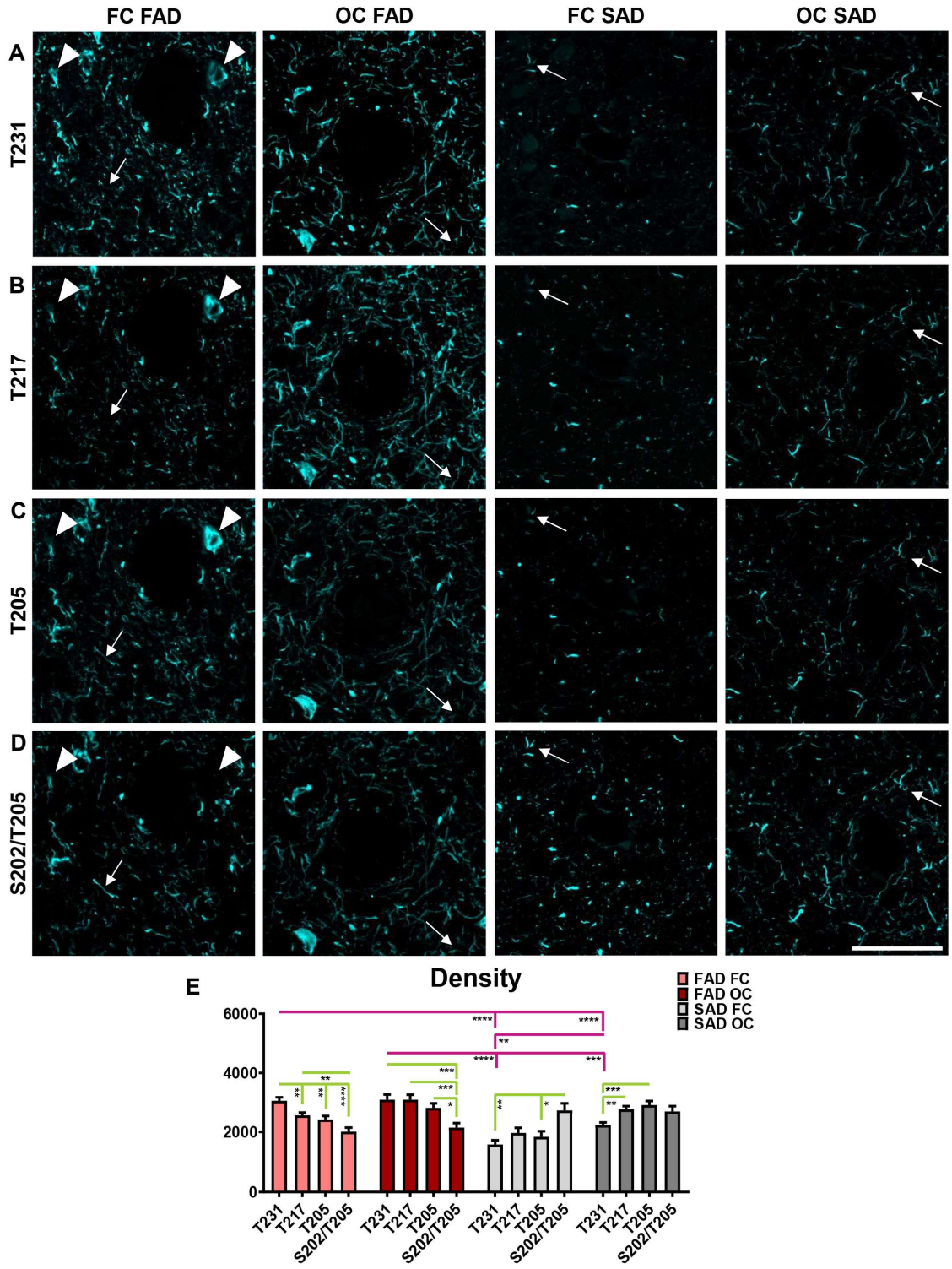

Figure 25: Phosphosite evaluation in FC and OC of FAD and SAD. *FC and OC of both FAD (n=10) and SAD (n=5) were stained for T231 (A), T217 (B), T205 (C) and S202/T205 (AT8), scale bar = 50µm (D). T231, T217 and T205 stained neurofibrillary tangles (NFT) in FAD (white arrowheads) but not in SAD. In the FC of FAD, it was observed that the different phosphorylations stained different parts of said NFTs (white arrowheads, A-D). In both*

*cortices of FAD and SAD the phosphorylations further stained the neuropil threads differently (white arrows, A-D). In the FC of FAD there was significantly more T231 density than T217 (p: **=0.0067), T205 (p: **=0.0011) and S202/T205 (p: ****<0.0001). Further there was significantly more T217 than S202/T205 (p: **=0.0059). In the OC of FAD there was no significant difference between T231 and T217 but there was significantly less S202/T205 than T231 (p: ***=0.0004), T217 (p: ***=0.0003) and T205 (p: *=0.111). In the FC of SAD, there was significantly more S202/T205 than T231 (p: **=0.0011) and T205 (p: *=0.0257) while in the OC there was significantly less T231 than T217 (p: **=0.0024) and T205 (p: ***=0.0009). The FC of FAD presented with significantly more T231 compared to the FC of SAD and OC of SAD (p: ****<0.0001). And the OC of FAD had significantly more T231 than FC and OC of SAD (p: ****<0.0001 and ***=0.0001, respectively). The OC of SAD showed significantly more T231 (p: **=0.0017) than the FC of SAD.*

Chapter 4: Evaluation of early changes in the vasculature

3.6 Vascular pathology in PS1KI mice

Provided that with the human material only end stage pathology can be evaluated where a large amount of comorbidities are present[35], a mouse line was generated carrying the E280A mutation, C57BL/6-Psen1$^{em1(E280A)}$. The mouse was generated by CRISPR/Cas in a C57/BL/6 background, and, from now on being referred to as PS1KI mouse. Given that this mouse line only carries a *PSEN1* mutation without humanised transgenic *APP* or tau mutations, it allowed studying early changes in the vasculature caused by the *PSEN1* E280A mutation. First, the vasculature of the PS1KI mice was evaluated by staining for laminin and smooth muscle actin (SMA) in 6-month-old wild-type mice, 6-month-old PS1KI mice, and 12-month-old PS1KI mice (Fig. 26A-F). There were no significant differences in the %Area of the markers or intensity of signal for either laminin (Fig. 26G, H) or SMA (Fig. 26I, J) in the groups. Additionally, significantly more tortuous vessels were found in 24-weeks-old PS1KI mice versus WT mice and 52-weeks-old PS1KI mice (Fig. 26K). In order to gain more insights, CLARITY (Fig. 27A, B) was used to gain 3D information about vascular branching. The branch length (Fig. 27C) was significantly longer in PS1KI mice when compared to WT mice while the number of branches (Fig. 27D) or junctions (Fig. 27E) was not significantly different.

This finding suggested abnormal angiogenesis in the PS1KI line. Thus, Notch3 signalling was evaluated in the mouse model due to its pivotal role in vessel development and homeostasis, and its possible dysmodulation as a γ-secretase substrate. Therefore, the Notch3 intracellular domain (NI3CD) was quantified for the nuclei of pericytes in isolated vessels from 6-months-old WT (Fig. 28A) and PS1KI (Fig. 28B) mice. There was significantly more NI3CD in the nuclei of pericytes in isolated vessels in PS1KI vs WT mice, seemly accumulating inside these nuclei (Fig. 28C).

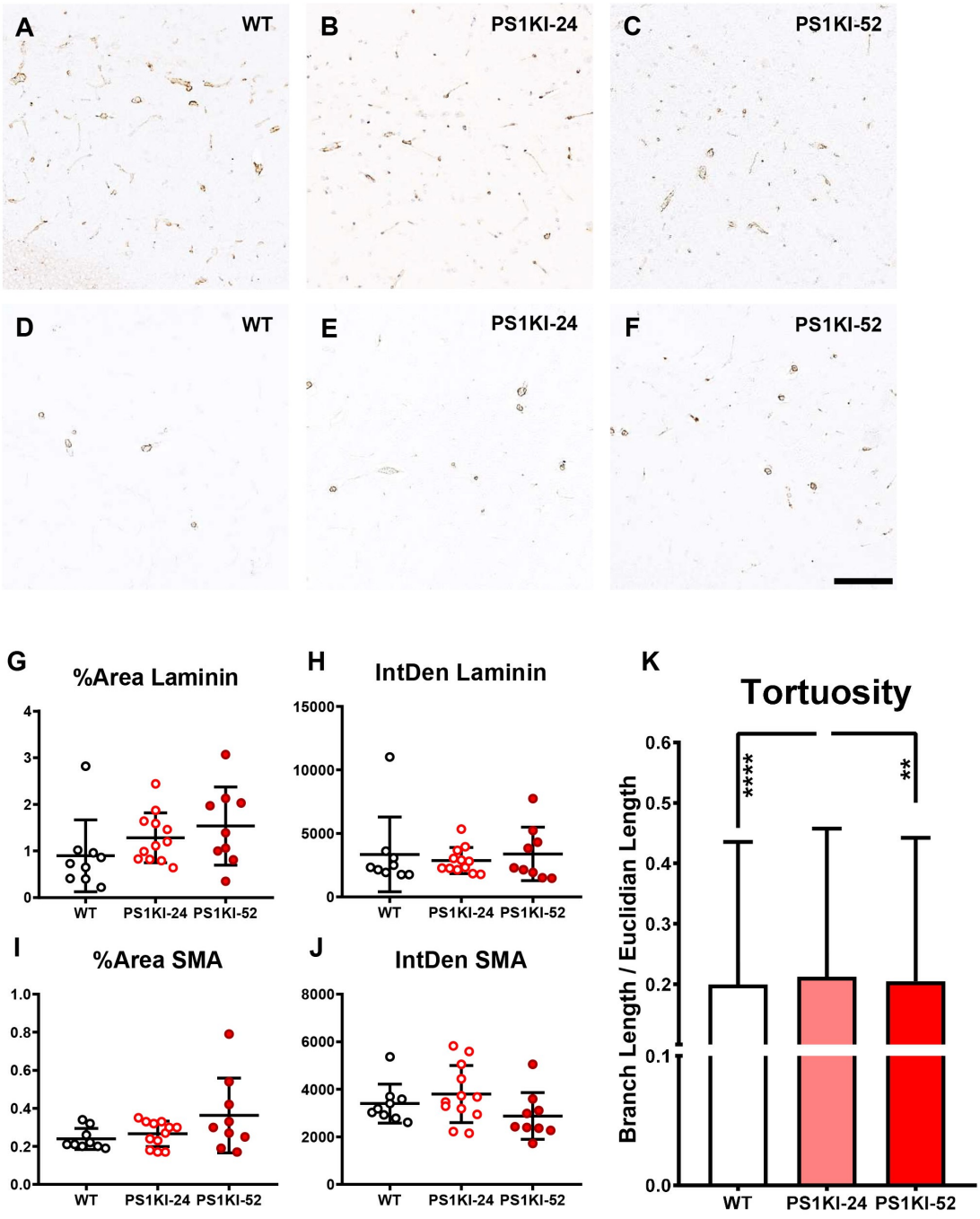

Figure 26: Vascular pathology and tortuosity in PS1KI mice. *Representative images are shown for laminin stained paraffin-fixed sections for 24-week-old WT (A), 24-week-old PS1KI (B) and 52-week-old PS1KI (C) (n=3). Similarly, representative images for SMA are displayed for 24-week-old WT (D), 24-week-old PS1KI (E) and 52-week-old PS1KI (F), scale bar = 100µm. The %area of laminin (G) and SMA (I) was quantified and no significant difference was found. Further, there was no significant difference in the integrated density of laminin (H) or SMA (J). However, in 24-week old PS1KI there were significant more tortuous vessels compared to 24-week-old WT and 52-week-old PS1KI (p: ****<0.001, **=0.0022)(K).*

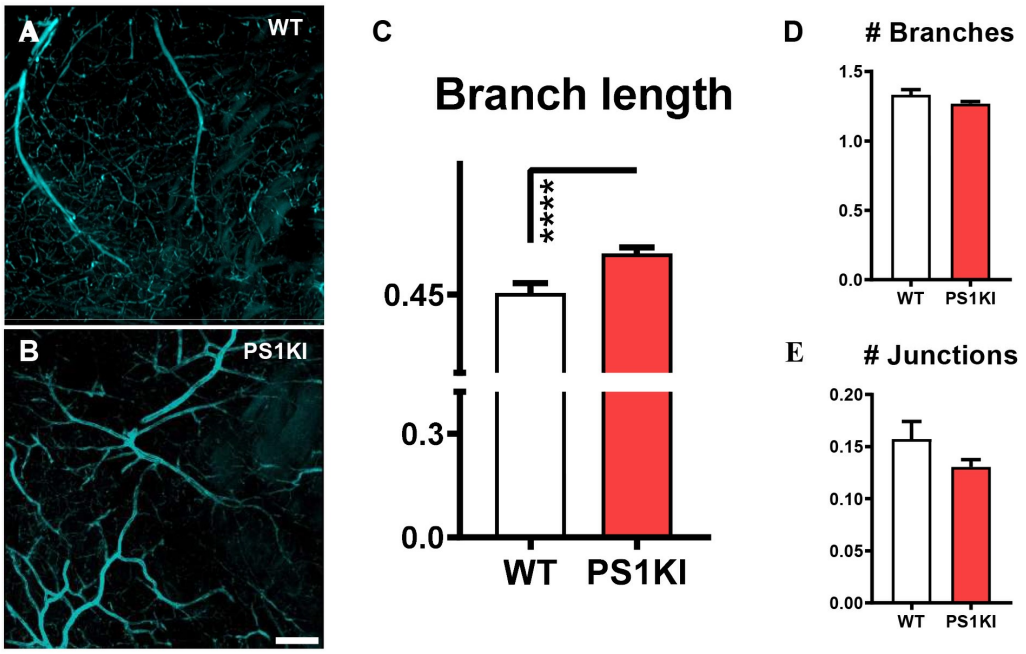

Figure 27 Branching in 6-month-old PS1KI and WT mice. *CLARITY was used to gain three-dimensional insight into the branching. Representative images are shown for 6-month-old (WT) (n=3) and 6-month-old PS1KI (B) (n=3), scale bar= 200µm. The branch length was significantly longer in PS1KI mice compared to WT (p: ****<0.0001) (C) while the number of branches (D) and number of junctions (E) was not significantly differences.*

In conclusion, there were no significant differences in the studied vascular markers. However, the vasculature of PS1KI mice seemed to be altered in the structural network of the vascular tree. This became evident due to more tortuous vessels with longer branches. A closer look at the exact mechanisms would be needed to identify the cause for the morphological changes in the vasculature.

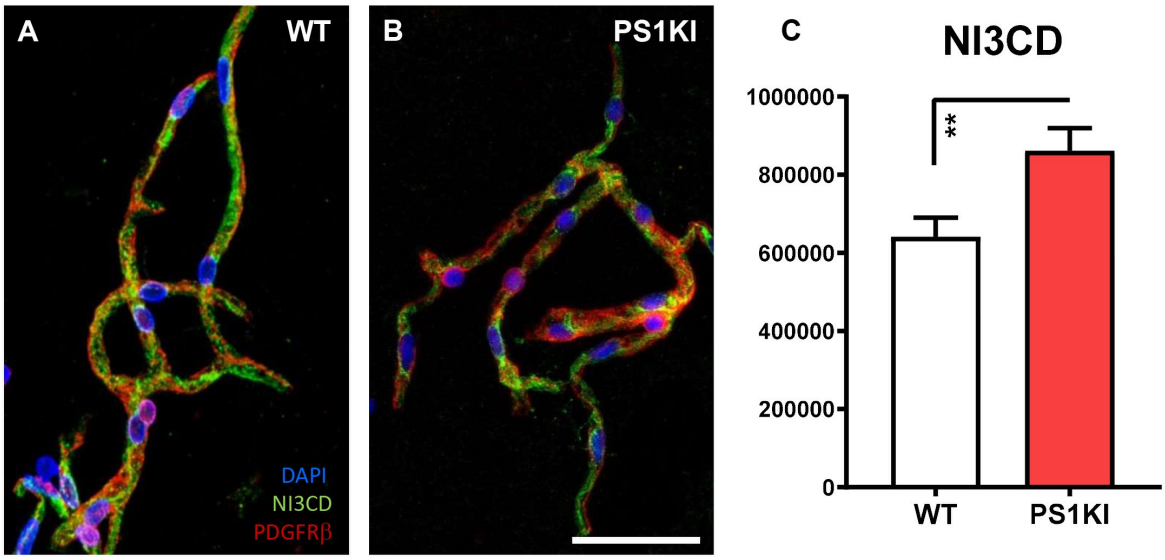

Figure 28: Notch3 intracellular domain in PS1KI and WT mice pericytes. *Isolated vessels of WT (A) (n=3) and PS1KI (B) (n=3) mice were stained for DAPI, NI3CD and PDGRFβ. NI3CD in the pericytes of those isolated vessels was found to be significantly higher in PS1KI than WT (C).*

3.7 Neurovascular unit modulations in PS1KI mice

In order to gain deeper insights into the vascular changes, electron microscopy was used for six months old PS1KI and WT mice. The focus of the analysis was the neurovascular unit in the hippocampus. Since the changes in the basement membrane were observed for FAD, the basement membrane (BM) was evaluated in WT (Fig. 29A, G) and PS1KI (Fig. 29B, H) mice. The analysis revealed abnormal thickening, duplication, and branching of the BM in PS1KI mice (red arrows, Fig. 29G, H), and the thickening of the BM was significantly increased in PS1KI mice (Fig. 29J). Notably, the mean BM thickness was 95.09 nm in WT mice, whereas PS1KI mice exhibited a significantly thicker BM, measuring 108.3 nm and the calculated difference of 13.21 nm ± 5.240 SEM. As part of the gliovascular unit, astrocyte end-feet were evaluated next. Many of the astrocyte end-feet (yellow colourised in Fig. 29D-F) presented with electron-dense degrading lamellar bodies (LB) in PS1KI mice (red arrowheads, Fig. 29E-F) but not in WT mice (Fig. 29D). A closer examination of the LB distribution revealed significant differences in the number of LB (Fig. 29K) and the diameter of the LB (Fig. 29L). Specifically, PS1KI mice exhibited a mean LB count per astrocyte end-foot of 1.160 compared to 0.1481 in WT, with a substantial difference of 1.012 ± 0.3060 SEM. Additionally, the mean LB diameter was markedly larger in PS1KI mice (2.045 µm) than in WT mice (0.07285 µm), with a substantial difference of 1.972 ± 0.2433 SEM.

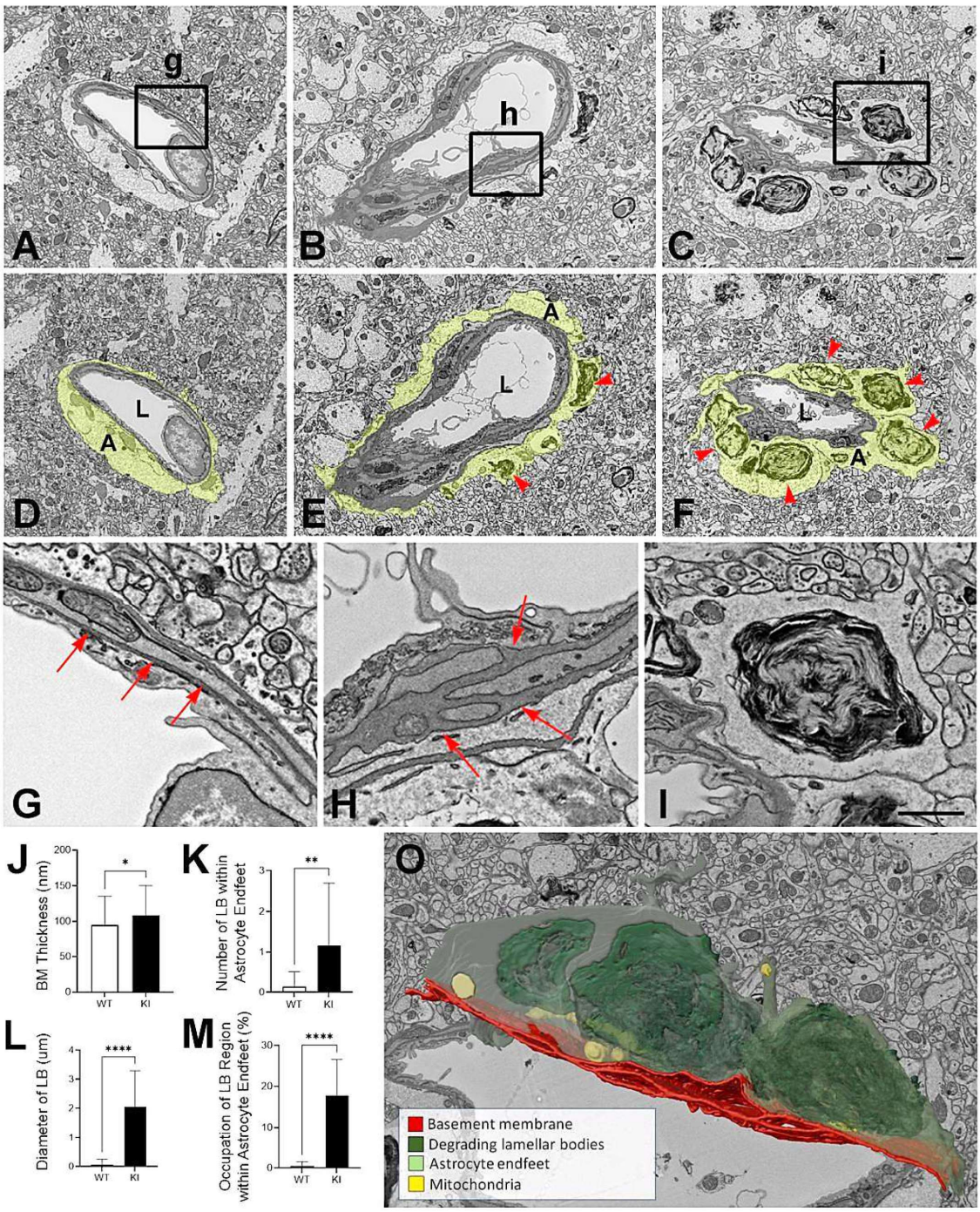

Figure 29: Vascular pathology in the hippocampus of PS1KI mice. *Abnormal thickening, branching and duplication of the basement membrane (BM) was observed for 6-month-old PS1KI mice (B, H) (n=3) but not for wild type (WT) (n=3) (A, G). Additionally, perivascular astrocyte end-feet surrounding vessel walls (yellow colourised in D-F) presented with electron-dense degrading lamellar bodies (LB) in PS1KI (red arrowheads, E, F, I) which were absent in WT (D). The BM was significantly thicker in PS1KI compared to WT (p: *=0.0123) (J). The number of LB (p: **=0.0018), their diameter (p: ****<0.0001) and the occupied area (p: ****<0.0001) of LB in astrocyte end-feet was significantly increased in PS1KI compared to WT (K-M). Finally, a 3D reconstruction is shown for PS1KI, illustrating the LB in astrocyte end-feet (O).*

Moreover, the analysis of LB area occupation within perivascular astrocyte end-feet revealed a significant disparity between WT and PS1KI groups. The mean occupation in WT was 0.5%, whereas in PS1KI, it was 17.82%, resulting in a notable difference of 17.28 ± 2.360 SEM (Fig. 29M). A 3D model of an astrocyte end-foot is shown illustrating the size and area of the LB (Fig. 29O). All of these changes suggest astrocytic pathology as an early event in *PSEN1* E280A mice, which could be associated with vascular changes given their role in the neurovascular unit.

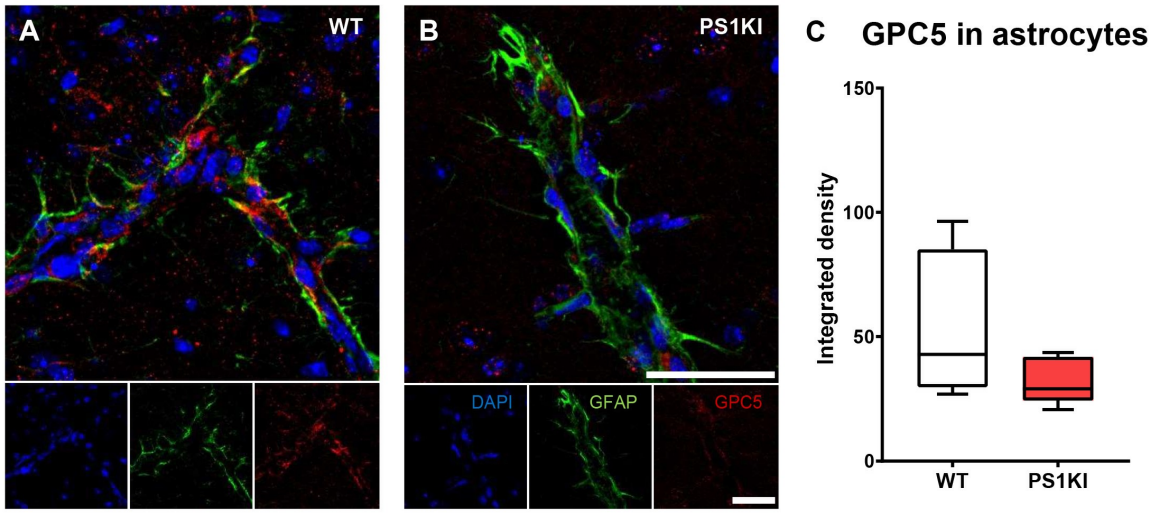

Figure 30: Glypican-5 immunoreactivity in astrocytes of PS1KI mice. *Representative images for WT (n=2) (A) and PS1KI (n=2) (B) vessels stained for DAPI, GFAP and GPC5 are shown, scale bar = 50µm. The integrated density was measured for GPC5 in astrocyte end-feet; the difference was not significant (unpaired t-test).*

Finally, the glycoprotein shown to be different in FAD was GPC5 and given the observed changes in the BM in PS1KI mice, GPC5 was evaluated in the PS1KI mice. No GPC5 deposits or accumulations were found in the vessel walls of either WT or PS1KI mice, but GPC5 signal was observed in WT astrocytes. Astrocyte end-feet contacting the vessel wall were found to express GPC5 in WT (Fig. 30A) and PS1KI mice (Fig. 30B). The comparison of GPC5 signal intensity, as measured by the integrated density, between WT and PS1KI did not show a significant difference; however, there was a trend indicating higher levels in WT, as depicted in Figure 30C. These results indicate a functional alteration of astrocytes in PS1KI animals, reflected in the decreased production of GPC5, with possible impact.

5. Discussion

In this work, the vasculature in FAD and SAD was compared using regular histological analyses, molecular biology approaches, and bioinformatics analyses. Various aspects of vascular pathology were evaluated such as the gliovascular unit and mural cell pathology. Additionally, a mouse model was available to evaluate early changes in pathology caused by the E280A mutation.

The presence of vascular pathology undetected by imaging during the life of the individuals was shown for both, FAD and SAD of the Colombian cases. Vascular pathology can be a simple side product of ageing, however, in FAD, there is an early onset of the disease with only a handful mutation carriers living past the 6th decade of their life[123,124]. There was significantly more vascular pathology in the FC of FAD compared to SAD and HC. The higher vulnerability of the FC in FAD to vascular pathology, without differences in other pathologies evaluated, is intriguing. One possibility is that the capillaries of the FC in FAD are more prone to vascular insults than in HC and SAD. This could be the result of the *PSEN1* mutation as recently, *PSEN1* mutations have been shown to affect small vessels and specifically mutations post codons 200 were associated with higher SVD imaging markers[125]. In the other cortices evaluated, there was no difference between FAD and SAD.

Further, there was no difference in the scoring for arteriosclerosis or PVS. The arteriosclerosis score might not differ between FAD and SAD because the prolonged disease duration is causing vascular damage in both disease variants, and especially with increased age in SAD. The presence of PVS was not different but the cellular and molecular composition of vessels with enlarged PVS could differ between FAD and SAD. The increased prevalence of vascular pathology is striking, given the relatively low prevalence of traditional cardiovascular risk factors in the studied group, except for hypertension. In FAD, the prevalence of hypertension was 40.63%, significantly higher than the prevalence for the general population in Colombia, which is 23%[126–128]. This suggests, the higher prevalence of hypertension could be related to *PSEN1* mutation independently of Aβ or tau pathology. PSEN1 was shown to be the driver of hypertension in other instances such as pulmonary hypertension[129]. Additionally, an increased presence of mixed AD pathology was shown in Hispanic populations[59]. The vascular scoring applied here, however, is not a direct enough or precise enough measurement for SVD

discrimination in this population, as it is only semi-quantitative and the presence of microinfarcts in most of the FAD cases rated these generally higher. The vascular scoring as well as CAA VCING, are well suited for diagnostic purposes but not sensitive enough to identify subtle differences. Therefore, all vessels within the FC and OC were quantified in FAD which also showed no significant differences. This was mainly caused by outlier cases presenting with an extremely high number of CAA vessels, or very few. However, the SAD cases used in this work were selected to have severe Aβ pathology and might not result in significant differences either. In human end-stage pathology brains, comorbidities such as Lewy body dementia, TDP-43 co-pathology or white matter rarefactions can be identified and should be considered as participants in the disease progression[35]. In the Colombian FAD family, large-vessel atherosclerosis was described before[35]. SVD is a major contributor to dementia and is related to hypertension which was present in 40% of the patients. Additionally, smoking, another traditional cardiovascular risk factor, was present in 43% of FAD individuals. Taken together, this suggests that the E280A mutation affects the vasculature and the increase in vascular pathology is not driven by the absolute amount of amyloid pathology but could rather be related to its relative composition in the vasculature.

Further, the Aβ peptidomics showed only FC FAD to have significantly different Aβ compositions in purified vessels. The differences in vascular pathology were most striking in FC but given that the total amount of CAA was not different, the molecular composition of CAA might have a bigger impact than the number of vessels affected. Previous work in the Colombian kindred studied the differences in Aβ peptide pathology with immunohistochemistry. Significantly more Aβ38 and Aβ43 were found in SAD vs FAD in Temporal Cortex while significantly more Aβ42 was present in FAD. The ratio of Aβ38/Aβ42 was shown as significantly higher in SAD[38]. The present study confirms the presence of more Aβ38 in SAD in isolated vessels of FC and OC from patients of the same kindred, while Aβ42 was not significantly different between groups or brain regions (Fig. 10). This could be correlated to findings from biomarker studies in which Aβ42 in the CSF alone was not a good discriminator of AD, but the Aβ42/Aβ40 ratio was. This could be the result of more abundant Aβ40, as shown here. Normalising Aβ42 with Aβ40 enables an adjustment for inter-individual differences, thereby improving the capability of amyloid peptides to discriminate between FAD and SAD[130].

Also, DAB-immunohistochemistry is not as sensitive as proteomic analysis, and signal analysis in DAB-immunohistochemistry is not stoichiometric because it does not comply with the Beer-Lambert law. The Beer-Lambert law relates the concentration of a reagent to its optical density or absorbance[131]. Further, purified vessels were used for the proteomic analysis. Thus, Aβ plaques can have been isolated alongside the isolated vessels, yet the majority of Aβ peptides identified resulted from the CAA as more Aβ40 was found which is mainly deposited in vessels. The Composition of CAA and plaques was shown to be different[132] and this was confirmed with the analysis performed here.

Next, over the past years, several proteomic studies have been performed to identify possible new biomarkers[133–135] and gain a deeper understanding of key pathways in disease[119,120] by employing algorithms such as weighted gene co-expression network analysis (WGCNA). In general, caution is needed when interpreting proteomic results as the expression levels of mRNA and protein can vary spatially, temporally, and quantitatively. Proteins associated with microtubule function, RNA/DNA binding, post-translational modification, and inflammation were found to be strongly associated with AD phenotype but were badly represented at the RNA level[136]. Here, RNA/DNA binding and modulation of RNA/DNA processes were significantly correlated with CAA in FAD. There can be an underlying disease associated mechanism or these related proteins are being co-immunoprecipitated with Aβ in the vessel wall. For brain tissue, the correlation between RNA and protein was shown to be weak[137] and the integration of different omics approaches became helpful to paint the full picture.

Previous studies showed loss of mitochondrial function and a hypometabolic phenotype in AD, a correlation between ECM proteins enriched in astrocytes and microglia and Braak stage while microtubule regulation was correlated with CERAD score[136]. Aβ-correlated proteins such as midkine (MDK), netrin 1 (NTN1), SMOC1 and intercellular adhesion molecule 1 (ICAM1), were shown to colocalise with Aβ in plaques in human tissue and 5x FAD mouse models. In binding assays however, only MDK and NTN1 bound to Aβ directly implicating a possible function for these proteins together[119]. Of these proteins, MDK, NTN1, and SMOC1 have been previously shown to be present in Aβ plaques[138]. Here, SMOC1 was found to be present in the vessel wall and to a lesser extent in the Aβ plaques. One possible explanation is that in the study by Bai et al.[119], sporadic, late-onset cases were used, while in this study, familial cases with an

early onset of disease were used. There is no information on CAA status in the AD cohort used in the study by Bai et al.[119], while in the FAD cohort, high degrees of CAA were shown.

Putting together DEPs, GSEA, WGCNA and other proteomic analyses, it becomes evident that AD proteomic profiles are a mixture of several simultaneous events. In the case of FAD, the integration of these analyses could clarify WGCNA findings, attributing mechanisms to the modules correlating with demographic or pathological features. At least two modules, ME1 and ME6, which correlate with CAA pathology can be attributed to co-aggregating events with the Aβ peptides involved in CAA deposition. The other two modules associating with CAA pathology, ME3 and ME7, show a more functional profile towards cytoskeleton and catabolism dysregulation. Interestingly, ME8 also showed RNA-related BPs, together with coherent CC and MF ontology terms, hinting to an actual molecular mechanism, and associating with disease duration and brain area in FAD cases. Further proof that these proteins were not just co-depositing with Aβ, but reflect functional features, is the analysis of FAD OC exclusively dysregulated proteins when Aβ co-aggregating proteins are subtracted, showing similar ontology terms than those found in ME8. Thus, caution is warranted when interpreting proteomic findings in any AD variant, and an effort to differentiate between co-depositing proteins and functionally involved proteins should be made.

For instance, Aβ deposits have been shown to aggregate with HSPGs, perlecan, collagen IV, laminin, and fibronectin in the vicinity of microvessels[11]. In FAD, Aβ was found to colocalise with ECM components in the vessel wall, while in SAD GPC5 expression was mainly located in astrocytes. A downregulation of GPC5 in AD and the overexpression of GPC5 preventing synaptic hyperexcitability in astrocytes have been reported before[139]. Thus, suggesting astrocytes in FAD are more exposed to synaptic hyperexcitability. VCAN and TNC were not clearly accumulating with Aβ in plaques or CAA but the signal was very abundant. Additionally, there was no significant difference between FAD and SAD for VCAN or TNC, which could be because these glycoproteins behave the same for any form of AD. Changes in the ECM of the perineuronal nets (PNN) have been described before for the 5xFAD mouse model, and PNN enmeshed neurons seem to exhibit resilience against phospho tau accumulation[140,141]. As mentioned above, collagen IV was found to accumulate in the CAA vessels[54] and this could be confirmed for both FAD and SAD. In order to study early changes of the ECM without other

pathologies interfering, mouse models are needed. For instance, a study in APP-KI mice showed ECM-receptor interaction, laminin interaction, and cell-substrate adhesion as the top 3 enriched biological pathways and processes in only 2-month-old animals. Proteins related to these processes were downregulated in animals of this age alongside reduced expression levels of PDGFRβ, a reduction in the tight junction protein claudin-5, and reduced adherens junction proteins. These were the earliest changes in brain capillaries prior to Aβ accumulation in the brain[142].

In the E280A PS1KI mice, abnormalities in BM in the form of BM thickening were shown for at 6 Month of age by means of EM. In the absence of Aβ or tau pathology, the changes observed can be attributed to the *PSEN1* E280A mutation, supported by the findings in post-mortem brain tissue from *PSEN1* E280A human carriers, and the reports mentioned above of *PSEN1* mutations affecting angiogenesis, highlighting a pathophysiological path of vascular pathology beyond the amyloid hypothesis and tau misfolding. Additionally, the proteomics of purified vessels from the FC of FAD revealed processes related to BM and blood vessel development suggesting these are also changes caused by the mutation.

Single-cell sequencing studies in AD revealed impaired angiogenesis, synaptic signalling, and myelination[143] by dysregulation of endothelial cells, astrocytes, and oligodendrocytes, and pericytes[144]. Pericytes were shown to induce polarisation of astrocyte end-feet and a reduced pericyte coverage resulted in reduced polarisation of AQP4 and increased BBB permeability[145]. Pericytes were assessed as PDGFRβ-positive cell bodies and previous studies showed decreased PDGFRβ coverage in capillaries of FC in s small sample of late-onset AD[146]. While more recent stereological studies demonstrated a denser capillary network with preserved pericytes in FC of late-onset AD[147]. A Single-cell revealed decreased PDGFRβ expression of pericytes in AD[148]. The present study showed apoptotic pericytes, fewer pericytes in non-dilated FAD vessels and overall reduced PDGFRβ coverage compared to SAD, which is consistent with the work by Sengillo et al. Moreover, ultrastructural analysis revealed apoptotic pericytes in FAD confirmed a reduction in pericytes in FAD[146]. Pericytes involved in maintaining ECM organisation presented with selective vulnerability and were shown to be present across small and large diameter brain vessels alongside other pericyte types[149]. The reduced coverage of non-dilated

vessels could be a result of the loss of ECM organisation pericytes as the non-dilated vessels of-often presented with thickened BM suggesting a dysregulation of BM in these vessels.

Aβ is accumulated perivascular, and in pericytes, the BM is degraded by MMPs, leading to an altered composition and thickening of the BM. Single-cell sequencing revealed, the selective vulnerability of ECM-maintaining pericytes, dysregulated vasoconstriction and compromised blood flow[149]. Reduced blood flow could result from constriction of capillaries at the site of pericytes[150]. Single-cell transcriptomics revealed Notch3 inactivation to alter the regulation of calcium and contractile function of mural cells, thereby promoting an increase in ECM[151].

The relevance of enlarged PVS for the glymphatic system has gained more and more relevance over the past years. In this work FAD vessels presented with significantly enlarged PVS in contrast to SAD. Although, the enlarged PVS can always be an artefact of the tissue processing due to prolonged fixation or the dehydration of the tissue prior paraffin embedding. However, if this were the case, the number of affected vessels should be more evenly distributed between the groups. Alternatively, CSF samples could have been analysed, for example for GFAP, to have a more direct measurement of astrocyte's status and the glymphatic system in the living brain. However, those samples were unfortunately not available for this project. Further, Aβ CAA-unaffected vessels presented with significantly enlarged PVS in contrast to all other vessels. The dilation of vessels was associated with reduced pericyte coverage. The enlargement of PVS could arguably translate into the loss of astrocyte end-feet in FAD. Still, with only histological analysis, it is not possible to determine the cause-and-effect relationship. Additionally, the remodelling of the BM further influences the polarisation of astrocyte end-feet. In healthy tissue, AQP4 is polarised towards the BM-facing the surface of astrocyte's end-feet. In AD, abnormal deposits could cause the translocation of AQP4 to outside of the PVS, thereby reducing the polarisation of AQP4 to astrocyte end-feet[11]. Further, mouse knock-out models showed that insufficient platelet-growth factor B signalling decreased AQP4 polarisation to astrocyte end-feet and that platelet-growth factor B was needed for the development of the glymphatic system[145]. Taken together, different processes were shown to change the interplay of the neurovascular unit in AD.

Astrocyte end-feet retract and pericytes contract altering blood flow and clearance of waste products[132,150]. Microinfarcts have been associated with reduced AQP4 levels that resulted in

dysfunction of the glymphatic system[152]. In the Colombian kindred the incidence of microin-microinfarcts was high and occurred with reduced perivascular AQP4 signal, as shown in this study and by Henao-Restrepo et al.[153]. It should be noted that *PSEN1* E280A FAD astrocytes have been shown to be distinctively dysregulated in single-cell analysis compared SAD astrocytes[154]. This combined with the accumulation of ECM components in the vessel walls, indicates reduced glymphatic clearance.

The proteomic analysis of purified vessels presented distinct differences between FC and OC in FAD. There was more reactive pathology happening in FC of FAD while typical pathological changes were observed in OC. ME17 in FC presented with processes related to the extracellular matrix and the regulation of Wnt signalling. Wnt signaling is generally thought to be a protective mechanism for synaptic integrity and memory maintenance[155]. Further, this module was negatively correlated to sex and HC, but positively correlated with FAD. This means there were more of those associated proteins present in FAD and that in FAD there is a different form of pathology happening than in SAD, especially in male mutation carriers. When FC and OC were compared for FAD only, the Wnt signaling processes did not show up in the modules, suggesting this is a global effect happening in the FAD brains. Wnt/β-catenin pathways further regulate the inactivation of GSK3β[156]. It is important to note that proteome profiling only reveals disease-correlated components, but correlation does not imply causation[119].

The goal of this thesis was to evaluate vascular pathology in FAD, but one cannot neglect a whole pathology that is happening alongside vascular and amyloid pathology. Additionally, previous work showed cortices to be differently affected by tau pathology in late-onset FAD. In order to determine if this is caused by vascular pathology driving the other pathologies, the tau phospho-proteome was evaluated in the same tissue that was used for the purified vessels. The balance between tau kinases and phosphatases regulates tau phosphorylation[157]. Hence, phosphorylation of tau is not sufficient to induce aggregation[158]. Tau phosphorylation was closely linked to abnormal mitochondria function and location. Thus, it is likely to contribute to depleting functional mitochondria from synapses and, thereby, causing synaptic dysfunction[14].

Tau presented with higher levels of phosphorylations in FAD compared to SAD as shown by the phospho proteome and predicted kinase activity. Additionally, specific kinases were more active in FC than in OC and vice versa. Tau hyperphosphorylation is a highly dynamic process in

which tau is phosphorylated and dephosphorylated by, for example, phosphatases or glycosyla-glycosylations. N-glycosylation was shown to suppress dephosphorylation and accelerate tau phosphorylation by changing the conformation. O-GlcNAcylation, a form of o-glycosylation, may protect against phosphorylation of tau[158]. Specific phosphorylations were shown to further detach tau or reduce the affinity of tau to microtubules such as S214[159], S262 and T231[160] . Additionally, the phosphosites T231, S235 and S262 were correlated with higher seeding capacity[161,162], and S262 is a special phosphorylation site as it is localised in the microtubule-binding region and S262 was shown to promote oligomerisation of tau[158]. In this study, S235 was found to be higher expressed in FAD compared to SAD in both cortices, and S262 was significantly higher in both cortices in FAD, suggesting a possible cause for higher pTau oligomerisation in FAD. The predicted kinase-substrate analysis revealed more active kinases in OC for phosphosite S235. All of the above mentioned phosphorylations were shown to be higher in FAD compared to SAD. Next, there was an antibody available for T231, T217, and T205, and there was significantly more T231 in FAD compared to SAD in both cortices, which could explain the higher phosphorylation levels in FAD. Interestingly, the diagnostic marker, AT8, staining S202/T205 presented with lower signal intensity and density in FAD compared to SAD in both cortices. Within FAD, the lower levels of AT8 in FC compared to OC could be confirmed, but the density of AT8 was not significantly different. The densities of the other phosphorylations studied with immunofluorescence were not significantly different between FC and OC in FAD. This suggests that even though AT8 presents differently in signal intensity, the amount of tau pathology is not actually different between FC and OC in FAD.

Kinases activity was then predicted based on the phosphosites found to be present in FAD, SAD, and HC. It revealed distinctively more active tau kinases in FAD compared to HC while SAD could be placed in between. High GSK3β activity was previously shown for AD[157,34] as well as the activation of MAP kinase signalling in AD[119]. Here, specific kinases were shown to be more active in the FC than in the OC and vice versa based on the predicted kinase activity. Explicitly, higher GSK3β activity was shown for the FC in FAD compared to OC in FAD. Phosphorylation of β-catenin by GSK3β promotes β-catenin destabilisation and degradation thereby impeding nuclear translocation of the protein[163]. Additionally, *PSEN1* mutations were shown to lose the ability to stabilise β-catenin resulting in reduced active β-catenin levels[164]. Further studies will

be needed to confirm the predicted kinase activity, but this gives more insight into the progres-progression of tau pathology. Unfortunately, only the kinase activity could be predicted, yet for a complete picture, phosphatases activity will need to be taken into account.

To evaluate the effect of the E280A mutation on the development of vascular pathology a mouse model was needed to avoid the comorbidities. The PS1KI mice presented with changes in tortuosity and vessel branching. The EM studies of human material revealed thickening of the BM alongside apoptotic astrocyte end-feet. Serial EM was employed to gain ultrastructural insights into alterations of the gliovascular unit. These analyses demonstrated thickening of the BM in PS1KI mice in the absence of Aβ or tau suggesting the E280A mutation causes these vascular changes before protein aggregates build up. Additionally, astrocyte end-feet presented with a high amount of LB occupying a large area of the astrocyte end-feet. These electron-dense LBs can be degraded cell organelles requiring further investigations. Alternatively, the astrocytes are under stress making them switch to a glycogenesis mode with an increase in fatty acid metabolism. In cell culture experiments, astrocytes were shown to be important mediators for Aβ induced neurotoxicity and tau phosphorylation[165], suggesting an important role for astrocytes in mediating disease progression. Thus, the serial EM revealed pathological changes in the gliovascular unit in 6-month-old animals. In *PSEN1* transgene mouse lines, vascular changes were shown by histology in aged animals, while ultrastructural differences in the form of BM thickening and distorted endothelial cell nuclei could be found in 11-month-old animals. The transgenic mice used in this study carried the M146V only in neurons. This could explain why the E280A mutation presented with vascular changes as early as 6 months of age with both histological and ultrastructural methods[166]. However, this does show that *PSEN1* mutations can cause vascular pathology and that neuronal to vascular signalling takes part in the pathogenesis of vascular pathology. The mouse model used in the current study carried the E280A mutation in all cells, possibly explaining an earlier visible neurovascular phenotype. In summary, the mouse model provided the insight that the E280A mutation is sufficient to induce vascular alterations in the form of abnormal branching, BM thickening, and abnormal LBs in astrocyte end-feet.

Finally, an effect of *PSEN1* mutations on angiogenesis prior to amyloid pathology has been shown. This opens the possibility for different γ-secretase substrates other than APP to be dysregulated. For example, Notch3, which is highly expressed in two cellular components of the

BBB, namely pericytes and smooth muscle cells. Notch3 signalling has been known to have a key role in development and to interact with various pathways. One of these pathways is the Wnt pathway which is involved in cell-fate determination, survival and proliferation. The balance in Notch and Wnt signalling is required for vascular sprouting and regression in angiogenesis[167]. The WGCNA from all groups showed regulation of Wnt signalling to be affected in the FC of FAD, and the PS1KI mice presented with significantly more Notch3 intracellular domain in the nuclei of pericytes. Taken together, there are two different ways in which angiogenesis could be impaired in *PSEN1* mutation carriers. First, *PSEN1* mutations and a dysregulation of Notch3 signalling both negatively impact β-catenin signalling. Second, altered Wnt signalling in combination with Notch dysregulation impairs cell proliferation and vascular sprouting. Thus, there are different key pathways of angiogenesis affected by the *PSEN1* mutation resulting in non-amyloidogenic vascular pathology prior amyloid accumulation and tau hyperphosphorylation.

There were several limitations to this work, the biggest being the uneven number of FAD (n=32) and SAD (n=10). This limited statistical analyses to non-parametric t-tests. Further, the SAD cases were matched in severity of Aβ pathology, which resulted in the low number of cases used in this study, and other differences between FAD and SAD might have gone unnoticed this way. White matter pathology was not addressed within the frame of this study but should be considered for future studies to obtain the complete picture of vascular pathology. Next, not all analyses were performed with all cases, due to material and resources limitations. Additionally, the quality of the post-mortem human tissue has to be taken into account. Confounding factors such as age, gender, PMI, and ischemia affect sample quality in AD, with larger effects on the resulting modified phospho-proteome than on the whole proteome because protein modifications are highly transient and dynamic[119]. This further reduces the power of comparison in some analysis.

The next drawback was that no CLARITY protocol could be made working on the available human tissue, to complement some of the findings, because the tissue has been over-fixated in formalin for a long time. The resulting crosslinking of formalin with amino acid side chains can prevent antibody binding, and hydrogen bonds can be disrupted by formaldehyde, resulting in changes of the protein configuration. The next limitation is the failure to establish a primary cell

culture model of the mice to identify possible mechanisms of the vascular pathology observed in human subjects and mice carrying the E280A mutation. This point is currently being addressed with the standardisation of immortalised cell cultures for different cell types carrying the *PSEN1* E280A mutation. The ultrastructural studies presented here were performed on 6-month-old animals. Unfortunately, the data sets for younger animals could not be obtained in the frame of this work but will be included in future publications.

6. Conclusions

This work showed that vascular pathology is indeed a main feature in AD, and contributes to its progression and severity. The morphological findings together with proteomic analyses in FAD showed a multifactorial picture for SVD pathology. Seemly, even though CAA pathology is a main factor in vascular damage, other processes involving neurovascular unit components such as pericytes and astrocytes are actually more relevant to the structural findings. Specifically, those associated to angiogenesis and glymphatic clearance.

Furthermore, with the help of a knock-in-mouse model, it was proven that E280A mutation causes early changes in the vasculature, promoting vascular damage without the need for protein aggregates. In fact, the strongest evidence points towards early astrocytic dysfunction that directly affects basement membrane structure and might be influencing vascular remodelling.

Previous evidence shows that Aβ and tau accumulation in *PSEN1* E280A patients takes place in the second and third decade of live, respectively. This work supports also for SVD as an early event in FAD pathology, it remains to be determined if that takes place simultaneously with those other pathological events. Further studies should address this issue in view of possible therapeutic approaches for this disorder. Finally, even though SAD etiopathology might diverge from that in FAD, the findings presented here can also shed a light on SVD contribution in this AD variant.

7. Annex

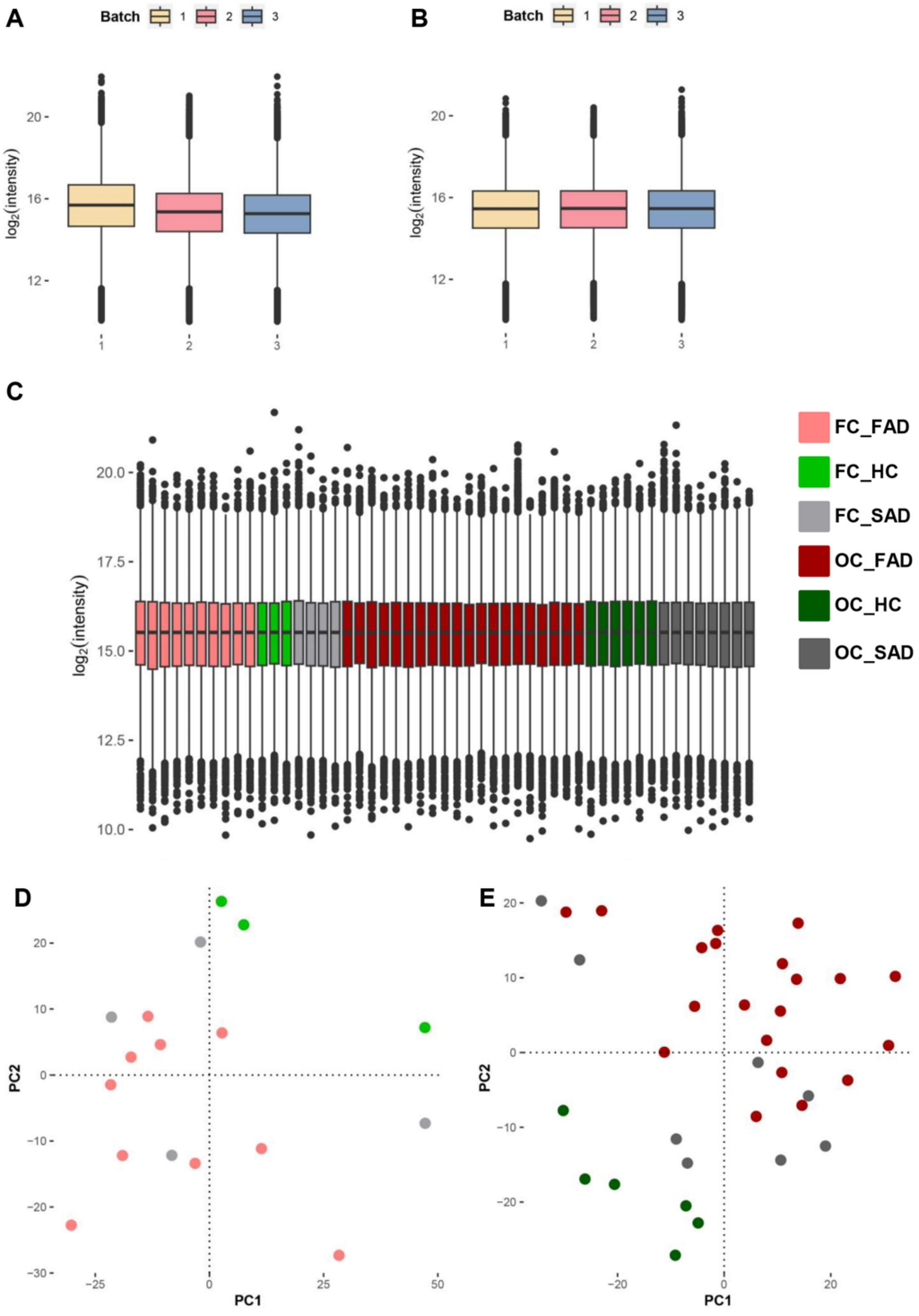

Annex Figure 1: Phosphotau-proteomics batch integration. *The batches before (A) and after (B) the use of harmonizR are shown. Additionally, for each case, the TMT data is shown (C). The principal component analysis showed the HC in FC (D) and OC (E) cluster separately from the AD groups.*

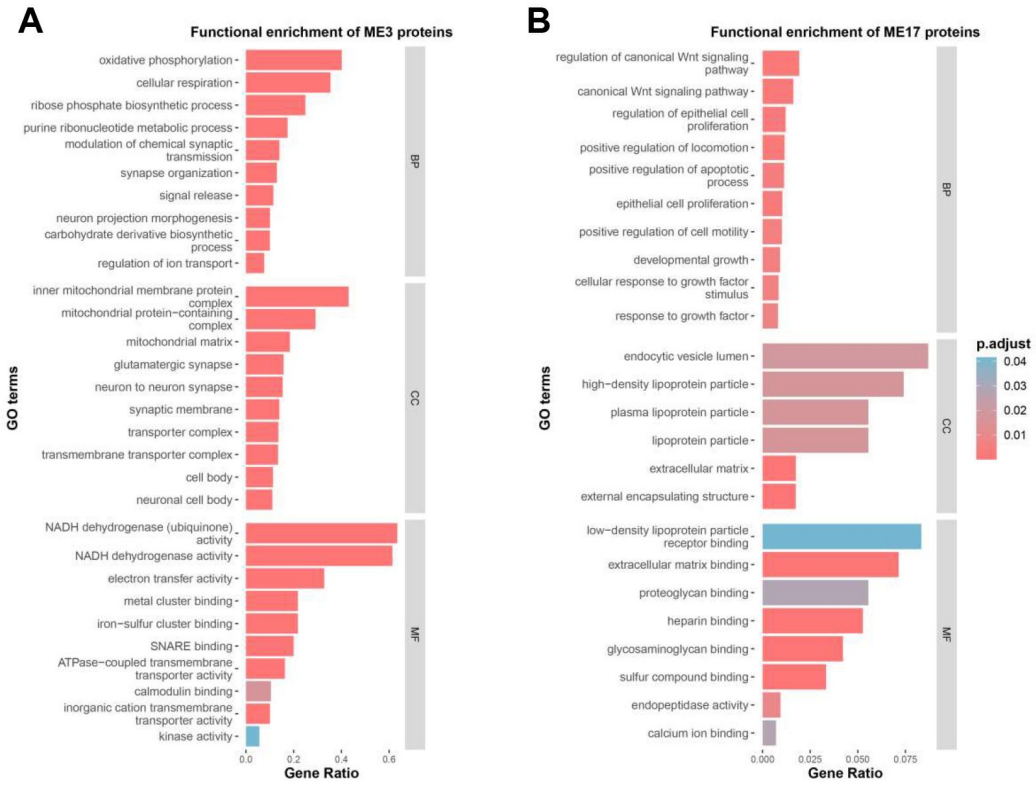

Annex Figure 2: Significant WGCNA modules in the FC of FAD and SAD. *The BPs of ME3 were related to oxidative phosphorylation and cellular respiration (A). In ME17 the BPs were associated to Wnt signalling and regulaiton of apoptotic processes (B).*

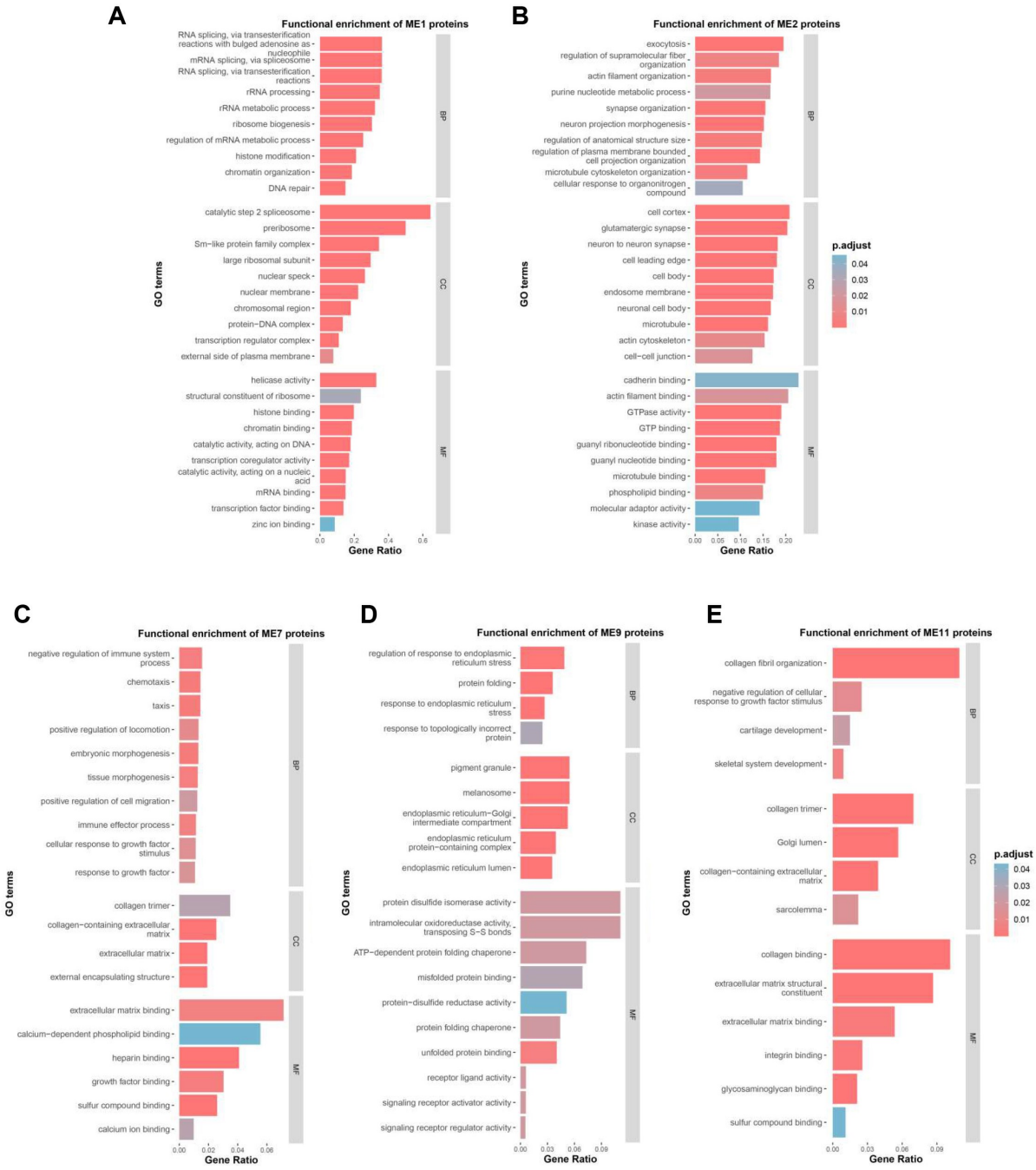

Annex Figure 3: Significant WGCNA modules in the OC of FAD and SAD. *The significant modules for the WGCNA in OC of FAD and SAD are shown. The BPs in ME1 were associated with RNA and mRNA processing (A). The BPs in ME 2 were related to exocytosis and actin filament organisation (B). The BPs of ME7 were associated with immune system process and tissue morphogenesis (C). ME9 contained BPs related to ER stress and protein folding (D). The BPs of ME11 were related to collagen fibril organisation as was reflected by the CC ontology term collagen trimer and MFs such as collagen binding (E).*

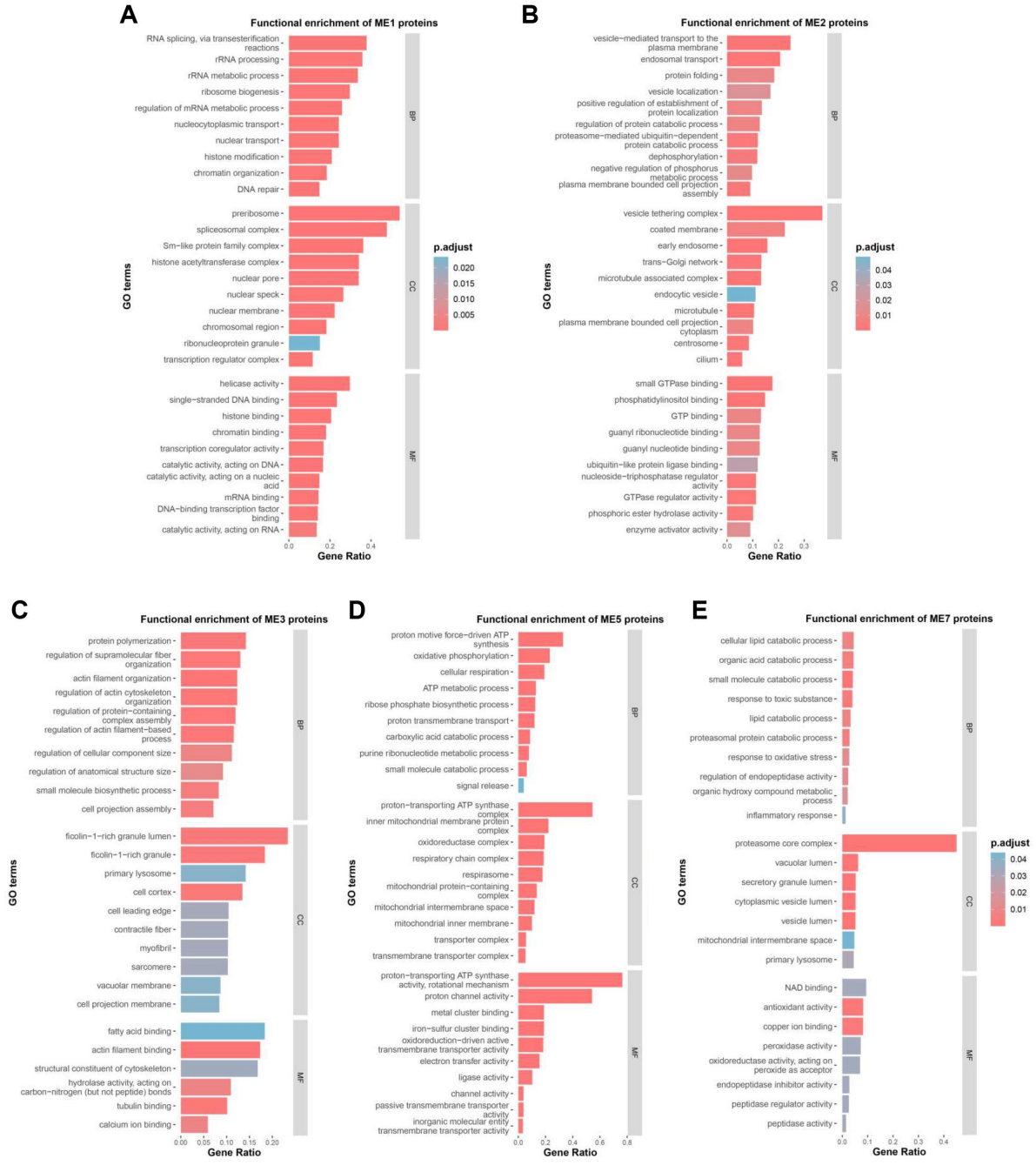

Annex Figure 4: Significant WGCNA modules in FAD. *The significant modules in the WGCNA of FC and OC in FAD and their functional enrichment of ME1 (A), ME2 (B), ME3 (C), ME5 (D) and ME7 (E) are shown. ME1 contains mainly BPs related to RNA processing. ME2 contained BPs related to transport and MFs related to GTP binding (B). The BPs of ME3 were related to protein polymerisation and actin filament organisation (C). In ME5 the BPs were associated with cellular respiration and ATP metabolic processes (D). Finally, in ME7 the BPs were related to catabolic processes (E).*

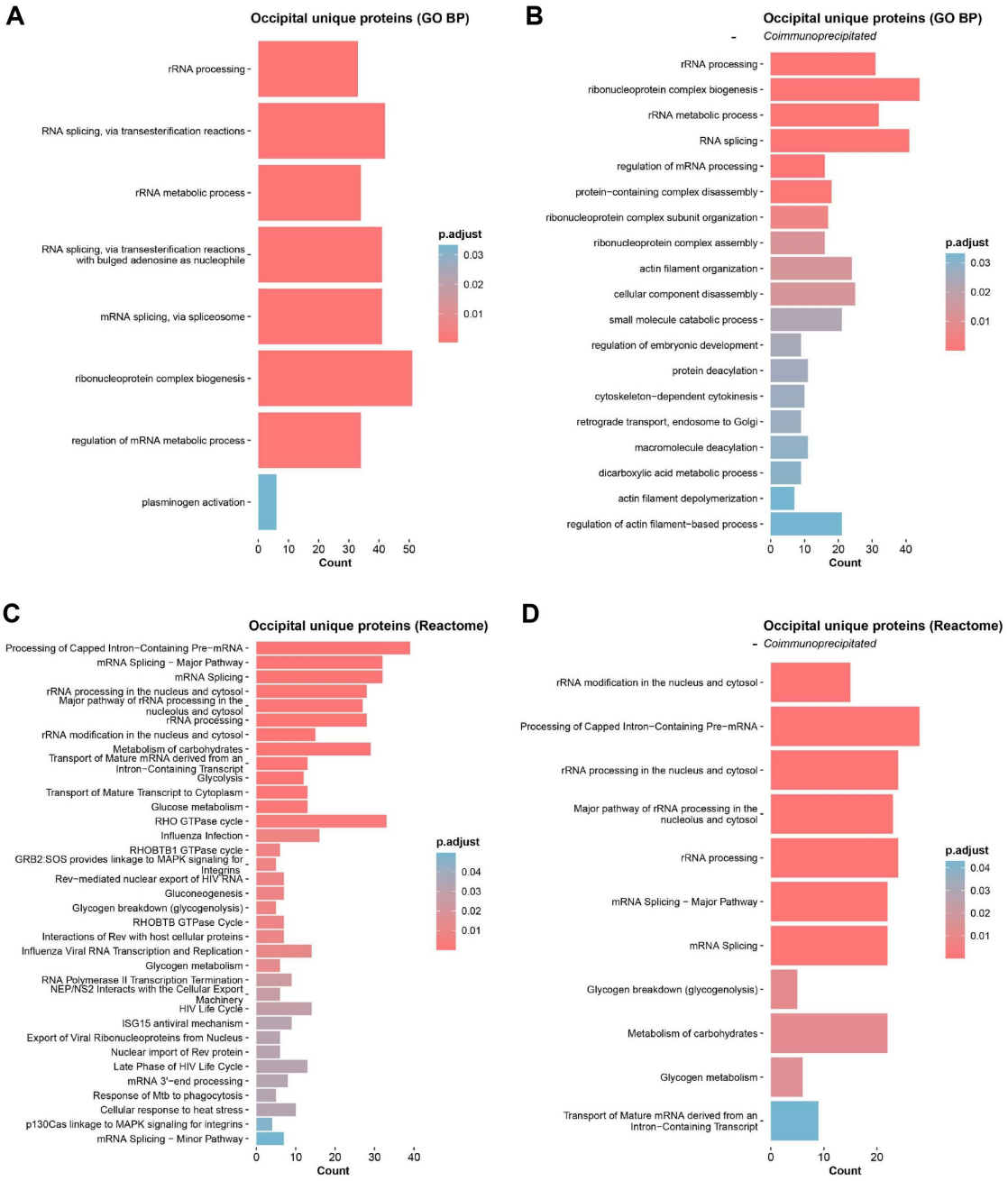

Annex Figure 5: GO BP of uniquely expressed proteins in the OC of FAD. *The GO BP is shown for the uniquely upregulated proteins in OC (496 proteins) (A) and the GO BP for the OC unique proteins minus the co-immunoprecipitated proteins (441 proteins) (B) is shown. For both analyses the reactome was plotted (C, D).*

8. List of Figures

9. List of Tables

10. List of Abbreviations

Aβ	Amyloid-β
AICD	APP intracellular domain
AD	Alzheimer's Disease
ADAD	Autosomal Dominant AD
ADAM/ADAMTS	Adamalysins
AGn	Agnosia
APH1	Anterior PHarynx defective 1 homolog
ApoE	Apolipoprotein E
ApoE4	Apolipoprotein E ε4 allele
AGC	Automatic Gain Control
AGr	Agraphia
ALe	Alexia
ANo	Anomia
APh	Aphasia
APP	Amyloid Precursor Protein
Apr	Apraxia
α-SMA	Alpha-Smooth Muscle Actin
AoD	Age of Death
AoO	Age of Onset
AQP4	Aquaporin-4
BBB	Blood-Brain Barrier
BM	Basement Membrane
BP	Biological Process
BR	Bradykinesia
CAA	Cerebral Amyloid Angiopathy
CB	Cacodylate Buffer
CBF	Cerebral Blood Flow
CC	Cellular Component
CERAD	Consortium to Establish a Registry for Alzheimer's Disease
CLDN-5	Claudin-5
CSVD	Cerebral Small Vessel Disease
CTF	C-Terminal Fragment
CWP	Cotton Wool Plaque
DAB	3,3'-Diaminobenzidine
DD	Disease Duration
ddH_2O	Distilled Water
DE	Depression
DEP	Differentially Expressed Protein
DIAN	Dominantly Inherited Alzheimer Network
DLB	Dementia with Lewy Bodies
EC/PE	Echolalia/Preservation
ECM	Extracellular Matrix
EGF	Epidermal Growth Factor
EGFR	Epidermal Growth Factor Repeats
EM	Electron Microscopy
EOAD	Early-Onset AD
FAD	Familial Alzheimer's disease
FC	Frontal Cortex
FTD	Frontotemporal Dementia
GA	Gait
GAG	Glycosamicoglycans
GFAP	Glial Fibrillary Acidic Protein
GO	Gene Ontology
GPC5	Glypican-5
GSEA	Gene Set Enrichment Analysis
GSK3	Glycogen Synthase Kinase-3
GSK3β	Glycogen Synthase Kinase-3 β
HA	Hallucinations
HBP	High Blood Pressure
HC	Healthy Control
Hes	Hairy and enhancer of split
Hey	Hes related with YRPW motif
HSPG	Heparan Sulfate Proteoglycans

IN Insomnia

ICAM1 intercellular adhesion molecule 1

IF Immunofluorescence

IP Immunoprecipitated

JNK C-Jun Amino Terminal Kinase

LB Lamellar Bodies

LOAD Late-Onset AD

MAPT Microtubule-Associated Protein Tau

MBD Microtubule Binding Domain

MDK Midkine

ME Module

MF Molecular Function

MI Memory Impairment

MMP Matrix Metalloproteinases

ND No data

NEXT Notch Extracellular Domain

NFT Neurofibrillary Tangle

NG No Genotype

NG2 Neural/glial antigen 2

NICD Notch Intracellular Domain

NI3CD Notch3 Intracellular Domain

NTN1 Netrin-1

NVU Neurovascular Unit

OC Occipital Cortex

PC Parietal Cortex

PEN-2 Presenilin Enhancer 2

PDGRFβ Platelet Derived Growth Factor Receptor β

PDK2/3 Pyruvate dehydrogenase kinase isoform 2/3

PMI Post-Mortem Intervall

PHF Paired Helical Filaments

PNN Perineuronal nets

PRR Proline-Rich Region

PSEN1 Presenilin-1

PSEN2 Presenilin-2

PSM Peptde spectrum match

PTM Post-Translational Modification

PVS Perivascular Space

S1P sphingosine-1-phosphate

SAD Sporadic Alzheimer's disease

SBEM serial block-face scanning electron microscopy

SD Spatial Disorientation

SDS Sodium dodecyl sulfate

SE Seizures

SMOC1 Secreted modular calcium-binding protein 1

SORL1 ApoE neuronal receptor

SP Speech

SQSTM1 Sequestosome 1

SVD Small Vessel Disease

TANC Tangle-Associated Neuritic Clusters

TC Temporal Cortex

TIMP Tissue Inhibitor of Metalloproteinases

TDP-43 TAR DNA-binding protein 43

TNC Tenascin-C

TR Tremor

RI Rigidity

ROI Region of Interest

VaD Vascular Dementia

VICD Vascular Cognitive Impairment and Dementia

VCAN Versican

VSMC Vascular Smooth Muscle Cell

WGCNA Weighted Gene Co-Expresison Network Analysis

WT Wild-type

WM White Matter

WMH White Matter Hyperintensities

11.List of Supplementary Figures

11. Bibliography

1. Prince M, Ali GC, Guerchet M, Wu YT, Prina M, Wimo A. *World Alzheimer Report 2015: The Global Impact of Dementia*. 1st ed. Alzheimer's Disease Indernational; 2015. Accessed October 1, 2019. https://www.alz.co.uk/research/world-report-2015

2. Soria Lopez JA, González HM, Léger GC. Alzheimer's disease. In: *Handbook of Clinical Neurology*. Vol 167. Elsevier; 2019:231-255. doi:10.1016/B978-0-12-804766-8.00013-3

3. Braak H, Braak E. Neuropathological stageing of Alzheimer-related changes. *Acta Neuropathol (Berl)*. 1991;82(4):239-259. doi:10.1007/BF00308809

4. Moloney CM, Lowe VJ, Murray ME. Visualization of neurofibrillary tangle maturity in Alzheimer's disease: A clinicopathologic perspective for biomarker research. *Alzheimers Dement*. 2021;17(9):1554-1574. doi:10.1002/alz.12321

5. Blennow K, de Leon MJ, Zetterberg H. Alzheimer's disease. *Lancet Lond Engl*. 2006;368(9533):387-403. doi:10.1016/S0140-6736(06)69113-7

6. De Strooper B, Saftig P, Craessaerts K, et al. Deficiency of presenilin-1 inhibits the normal cleavage of amyloid precursor protein. *Nature*. 1998;391(6665):387-390. doi:10.1038/34910

7. Wolfe MS, Xia W, Ostaszewski BL, Diehl TS, Kimberly WT, Selkoe DJ. Two transmembrane aspartates in presenilin-1 required for presenilin endoproteolysis and γ-secretase activity. *Nature*. 1999;398(6727):513-517. doi:10.1038/19077

8. Thal DR, Rüb U, Orantes M, Braak H. Phases of A beta-deposition in the human brain and its relevance for the development of AD. *Neurology*. 2002;58(12):1791-1800. doi:10.1212/wnl.58.12.1791

9. Chojdak-Łukasiewicz J, Dziadkowiak E, Zimny A, Paradowski B. Cerebral small vessel disease: A review. *Adv Clin Exp Med Off Organ Wroclaw Med Univ*. 2021;30(3):349-356. doi:10.17219/acem/131216

10. Yamaguchi H, Yamazaki T, Lemere CA, Frosch MP, Selkoe DJ. Beta amyloid is focally deposited within the outer basement membrane in the amyloid angiopathy of Alzheimer's disease. An immunoelectron microscopic study. *Am J Pathol*. 1992;141(1):249-259.

11. Howe MD, McCullough LD, Urayama A. The Role of Basement Membranes in Cerebral Amyloid Angiopathy. *Front Physiol*. 2020;11:601320. doi:10.3389/fphys.2020.601320

12. Devi G. The tauopathies. *Handb Clin Neurol*. 2023;196:251-265. doi:10.1016/B978-0-323-98817-9.00015-6

13. Neve RL, Harris P, Kosik KS, Kurnit DM, Donlon TA. Identification of cDNA clones for the human microtubule-associated protein tau and chromosomal localization of the genes for tau and microtubule-associated protein 2. *Mol Brain Res*. 1986;1(3):271-280. doi:10.1016/0169-328X(86)90033-1

14. Noble W, Hanger DP, Miller CCJ, Lovestone S. The importance of tau phosphorylation for neurodegenerative diseases. *Front Neurol*. 2013;4:83. doi:10.3389/fneur.2013.00083

15. Mandelkow EM, Mandelkow E. Tau in Alzheimer's disease. *Trends Cell Biol*. 1998;8(11):425-427. doi:10.1016/s0962-8924(98)01368-3

16. Muralidar S, Ambi SV, Sekaran S, Thirumalai D, Palaniappan B. Role of tau protein in Alzheimer's disease: The prime pathological player. *Int J Biol Macromol*. 2020;163:1599-1617. doi:10.1016/j.ijbiomac.2020.07.327

17. Wesseling H, Mair W, Kumar M, et al. Tau PTM Profiles Identify Patient Heterogeneity and Stages of Alzheimer's Disease. *Cell*. 2020;183(6):1699-1713.e13. doi:10.1016/j.cell.2020.10.029

18. Perry G, Kawai M, Tabaton M, et al. Neuropil threads of Alzheimer's disease show a marked alteration of the normal cytoskeleton. *J Neurosci Off J Soc Neurosci*. 1991;11(6):1748-1755. doi:10.1523/JNEUROSCI.11-06-01748.1991

19. Miyakawa T, Shimoji A, Kuramoto R, Higuchi Y. The relationship between senile plaques and cerebral blood vessels in Alzheimer's disease and senile dementia. Morphological mechanism of senile plaque production. *Virchows Arch B Cell Pathol Incl Mol Pathol*. 1982;40(2):121-129. doi:10.1007/BF02932857

20. Kawai M, Kalaria RN, Harik SI, Perry G. The relationship of amyloid plaques to cerebral capillaries in Alzheimer's disease. *Am J Pathol*. 1990;137(6):1435-1446.

21. Hansra GK, Popov G, Banaczek PO, et al. The neuritic plaque in Alzheimer's disease: perivascular degeneration of neuronal processes. *Neurobiol Aging*. 2019;82:88-101. doi:10.1016/j.neurobiolaging.2019.06.009

22. Dorszewska J, Prendecki M, Oczkowska A, Dezor M, Kozubski W. Molecular Basis of Familial and Sporadic Alzheimer's Disease. *Curr Alzheimer Res*. 2016;13(9):952-963. doi:10.2174/1567205013666160314150501

23. Rahman MA, Rahman MS, Uddin MJ, Mamum-Or-Rashid ANM, Pang MG, Rhim H. Emerging risk of environmental factors: insight mechanisms of Alzheimer's diseases. *Environ Sci Pollut Res Int*. 2020;27(36):44659-44672. doi:10.1007/s11356-020-08243-z

24. *Alzforum*. Accessed October 10, 2019. https://www.alzforum.org/mutations

25. Hane FT, Lee BY, Leonenko Z. Recent Progress in Alzheimer's Disease Research, Part 1: Pathology. *J Alzheimers Dis JAD*. 2017;57(1):1-28. doi:10.3233/JAD-160882

26. Robinson M, Lee BY, Hane FT. Recent Progress in Alzheimer's Disease Research, Part 2: Genetics and Epidemiology. *J Alzheimers Dis JAD*. 2017;57(2):317-330. doi:10.3233/JAD-161149

27. Shepherd C, McCann H, Halliday GM. Variations in the neuropathology of familial Alzheimer's disease. *Acta Neuropathol (Berl)*. 2009;118(1):37-52. doi:10.1007/s00401-009-0521-4

28. Schultz SA, Shirzadi Z, Schultz AP, et al. Location of pathogenic variants in *PSEN1* impacts progression of cognitive, clinical, and neurodegenerative measures in autosomal-dominant Alzheimer's disease. *Aging Cell*. 2023;22(8):e13871. doi:10.1111/acel.13871

29. Schellenberg GD, Montine TJ. The genetics and neuropathology of Alzheimer's disease. *Acta Neuropathol (Berl)*. 2012;124(3):305-323. doi:10.1007/s00401-012-0996-2

30. Chhatwal JP, Schultz SA, McDade E, et al. Variant-dependent heterogeneity in amyloid β burden in autosomal dominant Alzheimer's disease: cross-sectional and longitudinal analyses of an observational study. *Lancet Neurol*. 2022;21(2):140-152. doi:10.1016/S1474-4422(21)00375-6

31. Yang Y, Bagyinszky E, An SSA. Presenilin-1 (PSEN1) Mutations: Clinical Phenotypes beyond Alzheimer's Disease. *Int J Mol Sci*. 2023;24(9):8417. doi:10.3390/ijms24098417

32. Sepulveda-Falla D, Glatzel M, Lopera F. Phenotypic profile of early-onset familial Alzheimer's disease caused by presenilin-1 E280A mutation. *J Alzheimers Dis JAD*. 2012;32(1):1-12. doi:10.3233/JAD-2012-120907

33. Acosta-Baena N, Sepulveda-Falla D, Lopera-Gómez CM, et al. Pre-dementia clinical stages in presenilin 1 E280A familial early-onset Alzheimer's disease: a retrospective cohort study. *Lancet Neurol*. 2011;10(3):213-220. doi:10.1016/S1474-4422(10)70323-9

34. Sepulveda-Falla D, Chavez-Gutierrez L, Portelius E, et al. A multifactorial model of pathology for age of onset heterogeneity in familial Alzheimer's disease. *Acta Neuropathol (Berl)*. 2021;141(2):217-233. doi:10.1007/s00401-020-02249-0

35. Sepulveda-Falla D, Lanau CAV, White C, et al. Comorbidities in Early-Onset Sporadic versus Presenilin-1 Mutation-Associated Alzheimer's Disease Dementia: Evidence for Dependency on Alzheimer's Disease Neuropathological Changes. *MedRxiv Prepr Serv Health Sci*. Published online August 16, 2023:2023.08.14.23294081. doi:10.1101/2023.08.14.23294081

36. Littau JL, Velilla L, Hase Y, et al. Evidence of beta amyloid independent small vessel disease in familial Alzheimer's disease. *Brain Pathol*. 2022;32(6):e13097. doi:10.1111/bpa.13097

37. Sepulveda-Falla D, Barrera-Ocampo A, Hagel C, et al. Familial Alzheimer's disease-associated presenilin-1 alters cerebellar activity and calcium homeostasis. *J Clin Invest*. 2014;124(4):1552-1567. doi:10.1172/JCI66407

38. Dinkel F, Trujillo-Rodriguez D, Villegas A, et al. Decreased Deposition of Beta-Amyloid 1-38 and Increased Deposition of Beta-Amyloid 1-42 in Brain Tissue of Presenilin-1 E280A Familial Alzheimer's Disease Patients. *Front Aging Neurosci*. 2020;12:220. doi:10.3389/fnagi.2020.00220

39. Malek-Ahmadi M, Beach TG, Zamrini E, et al. Faster cognitive decline in dementia due to Alzheimer disease with clinically undiagnosed Lewy body disease. *PloS One*. 2019;14(6):e0217566. doi:10.1371/journal.pone.0217566

40. Spina S, La Joie R, Petersen C, et al. Comorbid neuropathological diagnoses in early versus late-onset Alzheimer's disease. *Brain J Neurol*. 2021;144(7):2186-2198. doi:10.1093/brain/awab099

41. Procter TV, Williams A, Montagne A. Interplay between Brain Pericytes and Endothelial Cells in Dementia. *Am J Pathol*. 2021;191(11):1917-1931. doi:10.1016/j.ajpath.2021.07.003

42. Araque Caballero MÁ, Suárez-Calvet M, Duering M, et al. White matter diffusion alterations precede symptom onset in autosomal dominant Alzheimer's disease. *Brain J Neurol*. 2018;141(10):3065-3080. doi:10.1093/brain/awy229

43. de la Torre JC, Mussivan T. Can disturbed brain microcirculation cause Alzheimer's disease? *Neurol Res*. 1993;15(3):146-153. doi:10.1080/01616412.1993.11740127

44. Kalaria RN. Vascular basis for brain degeneration: faltering controls and risk factors for dementia. *Nutr Rev*. 2010;68 Suppl 2:S74-87. doi:10.1111/j.1753-4887.2010.00352.x

45. Sweeney MD, Montagne A, Sagare AP, et al. Vascular dysfunction-The disregarded partner of Alzheimer's disease. *Alzheimers Dement J Alzheimers Assoc*. 2019;15(1):158-167. doi:10.1016/j.jalz.2018.07.222

46. Montagne A, Nation DA, Sagare AP, et al. APOE4 leads to blood–brain barrier dysfunction predicting cognitive decline. *Nature*. 2020;581(7806):71-76. doi:10.1038/s41586-020-2247-3

47. Hakim AM. Small Vessel Disease. *Front Neurol*. 2019;10:1020. doi:10.3389/fneur.2019.01020

48. Xhima K, Ottoy J, Gibson E, et al. Distinct spatial contributions of amyloid pathology and cerebral small vessel disease to hippocampal morphology. *Alzheimers Dement J Alzheimers Assoc*. Published online April 4, 2024. doi:10.1002/alz.13791

49. Rosenberg GA. Extracellular matrix inflammation in vascular cognitive impairment and dementia. *Clin Sci*. 2017;131(6):425-437. doi:10.1042/CS20160604

50. Shi Y, Wardlaw JM. Update on cerebral small vessel disease: a dynamic whole-brain disease. *BMJ*. 2016;1(3):83-92. doi:10.1136/svn-2016-000035

51. Mestre H, Kostrikov S, Mehta RI, Nedergaard M. Perivascular spaces, glymphatic dysfunction, and small vessel disease. *Clin Sci Lond Engl 1979*. 2017;131(17):2257-2274. doi:10.1042/CS20160381

52. Pontes-Neto OM, Auriel E, Greenberg SM. Advances in our Understanding of the Pathophysiology, Detection and Management of Cerebral Amyloid Angiopathy. *Eur Neurol Rev*. 2012;7(2):134-139. doi:10.17925/enr.2012.07.02.134

53. Yilmaz P, Ikram MA, Ikram MK, et al. Application of an Imaging-Based Sum Score for Cerebral Amyloid Angiopathy to the General Population: Risk of Major Neurological Diseases and Mortality. *Front Neurol*. 2019;10:1276. doi:10.3389/fneur.2019.01276

54. Kalaria RN, Sepulveda-Falla D. Cerebral Small Vessel Disease in Sporadic and Familial Alzheimer Disease. *Am J Pathol*. 2021;191(11):1888-1905. doi:10.1016/j.ajpath.2021.07.004

55. Del Bene A, Makin SDJ, Doubal FN, Inzitari D, Wardlaw JM. Variation in risk factors for recent small subcortical infarcts with infarct size, shape, and location. *Stroke*. 2013;44(11):3000-3006. doi:10.1161/STROKEAHA.113.002227

56. Iturria-Medina Y, Sotero RC, Toussaint PJ, Mateos-Pérez JM, Evans AC, Alzheimer's Disease Neuroimaging Initiative. Early role of vascular dysregulation on late-onset Alzheimer's disease based on multifactorial data-driven analysis. *Nat Commun*. 2016;7:11934. doi:10.1038/ncomms11934

57. Yew B, Nation DA, Alzheimer's Disease Neuroimaging Initiative. Cerebrovascular resistance: effects on cognitive decline, cortical atrophy, and progression to dementia. *Brain J Neurol*. 2017;140(7):1987-2001. doi:10.1093/brain/awx112

58. Korte N, Nortley R, Attwell D. Cerebral blood flow decrease as an early pathological mechanism in Alzheimer's disease. *Acta Neuropathol (Berl)*. 2020;140(6):793-810. doi:10.1007/s00401-020-02215-w

59. Filshtein TJ, Dugger BN, Jin LW, et al. Neuropathological Diagnoses of Demented Hispanic, Black, and Non-Hispanic White Decedents Seen at an Alzheimer's Disease Center. *J Alzheimers Dis JAD*. 2019;68(1):145-158. doi:10.3233/JAD-180992

60. Schoemaker D, Arboleda-Velasquez JF. NOTCH3 Signaling and Aggregation as Targets for the Treatment of CADASIL and Other NOTCH3-Associated Small-Vessel Disease. *Am J Pathol*. Published online April 22, 2021. doi:10.1016/j.ajpath.2021.03.015

61. Peters N, Opherk C, Zacherle S, Capell A, Gempel P, Dichgans M. CADASIL-associated Notch3 mutations have differential effects both on ligand binding and ligand-induced Notch3 receptor signaling through RBP-Jk. *Exp Cell Res*. 2004;299(2):454-464. doi:10.1016/j.yexcr.2004.06.004

62. Morris HE, Neves KB, Montezano AC, MacLean MR, Touyz RM. Notch3 signalling and vascular remodelling in pulmonary arterial hypertension. *Clin Sci*. 2019;133(24):2481-2498. doi:10.1042/CS20190835

63. Louvi A, Arboleda-Velasquez JF, Artavanis-Tsakonas S. CADASIL: A Critical Look at a Notch Disease. *Dev Neurosci*. 2006;28(1-2):5-12. doi:10.1159/000090748

64. Arboleda-Velasquez JF, Zhou Z, Shin HK, et al. Linking Notch signaling to ischemic stroke. *Proc Natl Acad Sci U S A*. 2008;105(12):4856-4861. doi:10.1073/pnas.0709867105

65. Schoemaker D, Arboleda-Velasquez JF. Notch3 Signaling and Aggregation as Targets for the Treatment of CADASIL and Other NOTCH3-Associated Small-Vessel Diseases. *Am J Pathol*. 2021;191(11):1856-1870. doi:10.1016/j.ajpath.2021.03.015

66. Iadecola C. Neurovascular regulation in the normal brain and in Alzheimer's disease. *Nat Rev Neurosci*. 2004;5(5):347-360. doi:10.1038/nrn1387

67. Iadecola C. The Pathobiology of Vascular Dementia. *Neuron*. 2013;80(4):844-866. doi:10.1016/j.neuron.2013.10.008

68. Paulsson M. Basement membrane proteins: structure, assembly, and cellular interactions. *Crit Rev Biochem Mol Biol*. 1992;27(1-2):93-127. doi:10.3109/10409239209082560

69. Sarrazin S, Lamanna WC, Esko JD. Heparan sulfate proteoglycans. *Cold Spring Harb Perspect Biol*. 2011;3(7):a004952. doi:10.1101/cshperspect.a004952

70. Hynes RO, Naba A. Overview of the matrisome--an inventory of extracellular matrix constituents and functions. *Cold Spring Harb Perspect Biol*. 2012;4(1):a004903. doi:10.1101/cshperspect.a004903

71. Kruegel J, Miosge N. Basement membrane components are key players in specialized extracellular matrices. *Cell Mol Life Sci CMLS*. 2010;67(17):2879-2895. doi:10.1007/s00018-010-0367-x

72. Bonnans C, Chou J, Werb Z. Remodelling the extracellular matrix in development and disease. *Nat Rev Mol Cell Biol*. 2014;15(12):786-801. doi:10.1038/nrm3904

73. Farhy Tselnicker I, Boisvert MM, Allen NJ. The role of neuronal versus astrocyte-derived heparan sulfate proteoglycans in brain development and injury. *Biochem Soc Trans*. 2014;42(5):1263-1269. doi:10.1042/BST20140166

74. Allnoch L, Leitzen E, Zdora I, Baumgärtner W, Hansmann F. Astrocyte depletion alters extracellular matrix composition in the demyelinating phase of Theiler's murine encephalomyelitis. *PloS One*. 2022;17(6):e0270239. doi:10.1371/journal.pone.0270239

75. Snow AD, Kinsella MG, Parks E, et al. Differential binding of vascular cell-derived proteoglycans (perlecan, biglycan, decorin, and versican) to the beta-amyloid protein of Alzheimer's disease. *Arch Biochem Biophys*. 1995;320(1):84-95. doi:10.1006/abbi.1995.1345

76. Díaz-Castro B, Robel S, Mishra A. Astrocyte Endfeet in Brain Function and Pathology: Open Questions. *Annu Rev Neurosci*. 2023;46(1):101-121. doi:10.1146/annurev-neuro-091922-031205

77. Ma S, Kwon HJ, Huang Z. A Functional Requirement for Astroglia in Promoting Blood Vessel Development in the Early Postnatal Brain. Baud O, ed. *PLoS ONE*. 2012;7(10):e48001. doi:10.1371/journal.pone.0048001

78. Sweeney MD, Ayyadurai S, Zlokovic BV. Pericytes of the neurovascular unit: key functions and signaling pathways. *Nat Neurosci*. 2016;19(6):771-783. doi:10.1038/nn.4288

79. Vanlandewijck M, He L, Mäe MA, et al. A molecular atlas of cell types and zonation in the brain vasculature. *Nature*. 2018;554(7693):475-480. doi:10.1038/nature25739

80. Szpak GM, Lewandowska E, Wierzba-Bobrowicz T, et al. Small cerebral vessel disease in familial amyloid and non-amyloid angiopathies: FAD-PS-1 (P117L) mutation and CA-DASIL. Immunohistochemical and ultrastructural studies. *Folia Neuropathol*. 2007;45(4):192-204.

81. Sengillo JD, Winkler EA, Walker CT, Sullivan JS, Johnson M, Zlokovic BV. Deficiency in mural vascular cells coincides with blood-brain barrier disruption in Alzheimer's disease. *Brain Pathol Zurich Switz*. 2013;23(3):303-310. doi:10.1111/bpa.12004

82. Fernandez-Klett F, Brandt L, Fernández-Zapata C, et al. Denser brain capillary network with preserved pericytes in Alzheimer's disease. *Brain Pathol Zurich Switz*. Published online September 2, 2020. doi:10.1111/bpa.12897

83. Uemura MT, Maki T, Ihara M, Lee VMY, Trojanowski JQ. Brain Microvascular Pericytes in Vascular Cognitive Impairment and Dementia. *Front Aging Neurosci*. 2020;12:80. doi:10.3389/fnagi.2020.00080

84. Rucker HK, Wynder HJ, Thomas WE. Cellular mechanisms of CNS pericytes. *Brain Res Bull*. 2000;51(5):363-369. doi:10.1016/s0361-9230(99)00260-9

85. Nitta T, Hata M, Gotoh S, et al. Size-selective loosening of the blood-brain barrier in claudin-5-deficient mice. *J Cell Biol*. 2003;161(3):653-660. doi:10.1083/jcb.200302070

86. Ceccom J, Loukh N, Lauwers-Cances V, et al. Reduced sphingosine kinase-1 and enhanced sphingosine 1-phosphate lyase expression demonstrate deregulated sphingosine 1-phosphate signaling in Alzheimer's disease. *Acta Neuropathol Commun*. 2014;2:12. doi:10.1186/2051-5960-2-12

87. Malaplate-Armand C, Florent-Béchard S, Youssef I, et al. Soluble oligomers of amyloid-beta peptide induce neuronal apoptosis by activating a cPLA2-dependent sphingomyelinase-ceramide pathway. *Neurobiol Dis*. 2006;23(1):178-189. doi:10.1016/j.nbd.2006.02.010

88. Cheng J, Korte N, Nortley R, Sethi H, Tang Y, Attwell D. Targeting pericytes for therapeutic approaches to neurological disorders. *Acta Neuropathol (Berl)*. 2018;136(4):507-523. doi:10.1007/s00401-018-1893-0

89. Santos GSP, Magno LAV, Romano-Silva MA, Mintz A, Birbrair A. Pericyte Plasticity in the Brain. *Neurosci Bull*. 2019;35(3):551-560. doi:10.1007/s12264-018-0296-5

90. Acosta-Baena N, Sepulveda-Falla D, Lopera-Gómez CM, et al. Pre-dementia clinical stages in presenilin 1 E280A familial early-onset Alzheimer's disease: a retrospective cohort study. *Lancet Neurol*. 2011;10(3):213-220. doi:10.1016/S1474-4422(10)70323-9

91. Sepulveda-Falla D, Matschke J, Bernreuther C, et al. Deposition of Hyperphosphorylated Tau in Cerebellum of PS1 E280A Alzheimer's Disease. *Brain Pathol*. 2011;21(4):452-463. doi:10.1111/j.1750-3639.2010.00469.x

92. Deramecourt V, Slade JY, Oakley AE, et al. Staging and natural history of cerebrovascular pathology in dementia. *Neurology*. 2012;78(14):1043-1050. doi:10.1212/WNL.0b013e31824e8e7f

93. Skrobot OA, Attems J, Esiri M, et al. Vascular cognitive impairment neuropathology guidelines (VCING): the contribution of cerebrovascular pathology to cognitive impairment. *Brain*. 2016;139(11):2957-2969. doi:10.1093/brain/aww214

94. Love S, Chalmers K, Ince P, et al. Development, appraisal, validation and implementation of a consensus protocol for the assessment of cerebral amyloid angiopathy in post-mortem brain tissue. *Am J Neurodegener Dis*. 2014;3(1):19-32.

95. Ruifrok AC, Johnston DA. Quantification of histochemical staining by color deconvolution. *Anal Quant Cytol Histol*. 2001;23(4):291-299.

96. Deerinck TJ, Bushong EA, Thor A, Ellisman MH. NCMIR methods for 3D EM: A new protocol for preparation of biological specimens for serial block face scanning electron microscopy. :6-8.

97. Kim KY, Rios LC, Le H, et al. Synaptic Specializations of Melanopsin-Retinal Ganglion Cells in Multiple Brain Regions Revealed by Genetic Label for Light and Electron Microscopy. *Cell Rep*. 2019;29(3):628-644.e6. doi:10.1016/j.celrep.2019.09.006

98. Kremer JR, Mastronarde DN, McIntosh JR. Computer visualization of three-dimensional image data using IMOD. *J Struct Biol*. 1996;116(1):71-76. doi:10.1006/jsbi.1996.0013

99. Gendusa R, Scalia CR, Buscone S, Cattoretti G. Elution of High-affinity (>10 $^{-9}$ K_D) Antibodies from Tissue Sections: Clues to the Molecular Mechanism and Use in Sequential Immunostaining. *J Histochem Cytochem*. 2014;62(7):519-531. doi:10.1369/0022155414536732

100. Rappsilber J, Mann M, Ishihama Y. Protocol for micro-purification, enrichment, pre-fractionation and storage of peptides for proteomics using StageTips. *Nat Protoc*. 2007;2(8):1896-1906. doi:10.1038/nprot.2007.261

101. Quast JP, Schuster D, Picotti P. protti: an R package for comprehensive data analysis of peptide- and protein-centric bottom-up proteomics data. Arighi C, ed. *Bioinforma Adv*. 2022;2(1):vbab041. doi:10.1093/bioadv/vbab041

102. Ritchie ME, Phipson B, Wu D, et al. limma powers differential expression analyses for RNA-sequencing and microarray studies. *Nucleic Acids Res*. 2015;43(7):e47-e47. doi:10.1093/nar/gkv007

103. Chen EY, Tan CM, Kou Y, et al. Enrichr: interactive and collaborative HTML5 gene list enrichment analysis tool. *BMC Bioinformatics*. 2013;14:128. doi:10.1186/1471-2105-14-128

104. Kuleshov MV, Jones MR, Rouillard AD, et al. Enrichr: a comprehensive gene set enrichment analysis web server 2016 update. *Nucleic Acids Res*. 2016;44(W1):W90-97. doi:10.1093/nar/gkw377

105. Xie Z, Bailey A, Kuleshov MV, et al. Gene Set Knowledge Discovery with Enrichr. *Curr Protoc*. 2021;1(3):e90. doi:10.1002/cpz1.90

106. Cox J, Mann M. MaxQuant enables high peptide identification rates, individualized p.p.b.-range mass accuracies and proteome-wide protein quantification. *Nat Biotechnol*. 2008;26(12):1367-1372. doi:10.1038/nbt.1511

107. Huang T, Choi M, Tzouros M, et al. MSstatsTMT: Statistical Detection of Differentially Abundant Proteins in Experiments with Isobaric Labeling and Multiple Mixtures. *Mol Cell Proteomics*. 2020;19(10):1706-1723. doi:10.1074/mcp.RA120.002105

108. Wu T, Hu E, Xu S, et al. clusterProfiler 4.0: A universal enrichment tool for interpreting omics data. *The Innovation*. 2021;2(3):100141. doi:10.1016/j.xinn.2021.100141

109. Langfelder P, Horvath S. WGCNA: an R package for weighted correlation network analysis. *BMC Bioinformatics*. 2008;9:559. doi:10.1186/1471-2105-9-559

110. Kolde R. Pheatmap: pretty heatmaps. R Package Version 1.0.12. Published online January 4, 2019. https://cran.r-project.org/web/packages/pheatmap/pheatmap.pdf

111. HarmonizR. https://github.com/SimonSchlumbohm/HarmonizR

112. Voß H, Schlumbohm S, Barwikowski P, et al. HarmonizR enables data harmonization across independent proteomic datasets with appropriate handling of missing values. *Nat Commun*. 2022;13(1):3523. doi:10.1038/s41467-022-31007-x

113. Wickham H. Data Analysis. In: *Ggplot2*. Use R! Springer International Publishing; 2016:189-201. doi:10.1007/978-3-319-24277-4_9

114. Kim HJ, Kim T, Hoffman NJ, et al. PhosR enables processing and functional analysis of phosphoproteomic data. *Cell Rep*. 2021;34(8):108771. doi:10.1016/j.celrep.2021.108771

115. Feng L, Wang G, Song Q, et al. Proteomics revealed an association between ribosome-associated proteins and amyloid beta deposition in Alzheimer's disease. *Metab Brain Dis*. 2024;39(2):263-282. doi:10.1007/s11011-023-01330-3

116. Rørvig S, Honore C, Larsson LI, et al. Ficolin-1 is present in a highly mobilizable subset of human neutrophil granules and associates with the cell surface after stimulation with fMLP. *J Leukoc Biol*. 2009;86(6):1439-1449. doi:10.1189/jlb.1008606

117. Camero S, Ayuso JM, Barrantes A, Benítez MJ, Jiménez JS. Specific binding of DNA to aggregated forms of Alzheimer's disease amyloid peptides. *Int J Biol Macromol*. 2013;55:201-206. doi:10.1016/j.ijbiomac.2013.01.007

118. Ferdosh S, Banerjee S, Barat C. Amplification of Amyloid Protein-induced Aggregation of the Eukaryotic Ribosome. *Protein Pept Lett*. 2022;29(11):993-1005. doi:10.2174/0929866529666220905112156

119. Bai B, Wang X, Li Y, et al. Deep Multilayer Brain Proteomics Identifies Molecular Networks in Alzheimer's Disease Progression. *Neuron*. 2020;105(6):975-991.e7. doi:10.1016/j.neuron.2019.12.015

120. Drummond E, Kavanagh T, Pires G, et al. The amyloid plaque proteome in early onset Alzheimer's disease and Down syndrome. *Acta Neuropathol Commun*. 2022;10(1):53. doi:10.1186/s40478-022-01356-1

121. Awwad K, Hu J, Shi L, et al. Role of secreted modular calcium-binding protein 1 (SMOC1) in transforming growth factor β signalling and angiogenesis. *Cardiovasc Res*. 2015;106(2):284-294. doi:10.1093/cvr/cvv098

122. Tewari BP, Chaunsali L, Prim CE, Sontheimer H. A glial perspective on the extracellular matrix and perineuronal net remodeling in the central nervous system. *Front Cell Neurosci*. 2022;16:1022754. doi:10.3389/fncel.2022.1022754

123. Sepulveda-Falla D, Sanchez JS, Almeida MC, et al. Distinct tau neuropathology and cellular profiles of an APOE3 Christchurch homozygote protected against autosomal dominant Alzheimer's dementia. *Acta Neuropathol (Berl)*. 2022;144(3):589-601. doi:10.1007/s00401-022-02467-8

124. Lopera F, Marino C, Chandrahas AS, et al. Resilience to autosomal dominant Alzheimer's disease in a Reelin-COLBOS heterozygous man. *Nat Med*. 2023;29(5):1243-1252. doi:10.1038/s41591-023-02318-3

125. Joseph-Mathurin N, Feldman RL, Lu R, et al. Presenilin-1 mutation position influences amyloidosis, small vessel disease, and dementia with disease stage. *Alzheimers Dement*. 2024;20(4):2680-2697. doi:10.1002/alz.13729

126. Camacho PA, Gomez-Arbelaez D, Molina DI, et al. Social disparities explain differences in hypertension prevalence, detection and control in Colombia. *J Hypertens*. 2016;34(12):2344-2352. doi:10.1097/HJH.0000000000001115

127. Zurique Sánchez MS, Zurique Sánchez CP, Camacho López PA, Sanchez Sanabria M, Hernández Hernández SC. Prevalencia de hipertensión arterial en Colombia: Revisión sistemática y meta-análisis. *Acta Médica Colomb*. 2019;44(4). doi:10.36104/amc.2019.1293

128. Barrera L, Oviedo D, Silva A, Tovar D, Méndez F. Continuity of Care and the Control of High Blood Pressure at Colombian Primary Care Services. *Inq J Health Care Organ Provis Financ*. 2021;58:004695802110470. doi:10.1177/00469580211047043

129. Shen T, Shi J, Zhao X, et al. Presenilin 1 Is a Therapeutic Target in Pulmonary Hypertension and Promotes Vascular Remodeling. *Am J Respir Cell Mol Biol*. Published online February 21, 2024. doi:10.1165/rcmb.2022-0426OC

130. Lewczuk P, Wiltfang J, Kornhuber J, Verhasselt A. Distributions of Aβ42 and Aβ42/40 in the Cerebrospinal Fluid in View of the Probability Theory. *Diagnostics*. 2021;11(12):2372. doi:10.3390/diagnostics11122372

131. Oshina I, Spigulis J. Beer-Lambert law for optical tissue diagnostics: current state of the art and the main limitations. *J Biomed Opt*. 2021;26(10):100901. doi:10.1117/1.JBO.26.10.100901

132. Morris AWJ, Carare RO, Schreiber S, Hawkes CA. The Cerebrovascular Basement Membrane: Role in the Clearance of β-amyloid and Cerebral Amyloid Angiopathy. *Front Aging Neurosci*. 2014;6:251. doi:10.3389/fnagi.2014.00251

133. Whelan CD, Mattsson N, Nagle MW, et al. Multiplex proteomics identifies novel CSF and plasma biomarkers of early Alzheimer's disease. *Acta Neuropathol Commun*. 2019;7(1):169. doi:10.1186/s40478-019-0795-2

134. Higginbotham L, Ping L, Dammer EB, et al. Integrated proteomics reveals brain-based cerebrospinal fluid biomarkers in asymptomatic and symptomatic Alzheimer's disease. *Sci Adv*. 2020;6(43):eaaz9360. doi:10.1126/sciadv.aaz9360

135. Weiner S, Blennow K, Zetterberg H, Gobom J. Next-generation proteomics technologies in Alzheimer's disease: from clinical research to routine diagnostics. *Expert Rev Proteomics*. 2023;20(7-9):143-150. doi:10.1080/14789450.2023.2255752

136. Seyfried NT, Dammer EB, Swarup V, et al. A Multi-network Approach Identifies Protein-Specific Co-expression in Asymptomatic and Symptomatic Alzheimer's Disease. *Cell Syst*. 2017;4(1):60-72.e4. doi:10.1016/j.cels.2016.11.006

137. Sharma K, Schmitt S, Bergner CG, et al. Cell type- and brain region-resolved mouse brain proteome. *Nat Neurosci*. 2015;18(12):1819-1831. doi:10.1038/nn.4160

138. Xiong F, Ge W, Ma C. Quantitative proteomics reveals distinct composition of amyloid plaques in Alzheimer's disease. *Alzheimers Dement J Alzheimers Assoc*. 2019;15(3):429-440. doi:10.1016/j.jalz.2018.10.006

139. Salas I, Paumier A, Switzler C, Allen N. Astrocyte Gpc5 overexpression prevents hippocampal synaptic hyperexcitability in APP/PS1 mouse. *Alzheimers Dement*. 2023;19(S13):e076867. doi:10.1002/alz.076867

140. Crapser JD, Spangenberg EE, Barahona RA, Arreola MA, Hohsfield LA, Green KN. Microglia facilitate loss of perineuronal nets in the Alzheimer's disease brain. *EBioMedicine*. 2020;58:102919. doi:10.1016/j.ebiom.2020.102919

141. Scarlett JM, Hu SJ, Alonge KM. The "Loss" of Perineuronal Nets in Alzheimer's Disease: Missing or Hiding in Plain Sight? *Front Integr Neurosci*. 2022;16:896400. doi:10.3389/fnint.2022.896400

142. Ito S, Yagi R, Ogata S, et al. Proteomic alterations in the brain and blood-brain barrier during brain Aβ accumulation in an APP knock-in mouse model of Alzheimer's disease. *Fluids Barriers CNS*. 2023;20(1):66. doi:10.1186/s12987-023-00466-9

143. Lau SF, Cao H, Fu AKY, Ip NY. Single-nucleus transcriptome analysis reveals dysregulation of angiogenic endothelial cells and neuroprotective glia in Alzheimer's disease. *Proc Natl Acad Sci U S A*. 2020;117(41):25800-25809. doi:10.1073/pnas.2008762117

144. Ting KK, Coleman P, Kim HJ, et al. Vascular senescence and leak are features of the early breakdown of the blood-brain barrier in Alzheimer's disease models. *GeroScience*. 2023;45(6):3307-3331. doi:10.1007/s11357-023-00927-x

145. Munk AS, Wang W, Bèchet NB, et al. PDGF-B Is Required for Development of the Glymphatic System. *Cell Rep*. 2019;26(11):2955-2969.e3. doi:10.1016/j.celrep.2019.02.050

146. Sengillo JD, Winkler EA, Walker CT, Sullivan JS, Johnson M, Zlokovic BV. Deficiency in Mural Vascular Cells Coincides with Blood–Brain Barrier Disruption in A lzheimer's Disease. *Brain Pathol*. 2013;23(3):303-310. doi:10.1111/bpa.12004

147. Fernandez-Klett F, Brandt L, Fernández-Zapata C, et al. Denser brain capillary network with preserved pericytes in Alzheimer's disease. *Brain Pathol*. 2020;30(6):1071-1086. doi:10.1111/bpa.12897

148. Sun N, Akay LA, Murdock MH, et al. Single-nucleus multiregion transcriptomic analysis of brain vasculature in Alzheimer's disease. *Nat Neurosci*. 2023;26(6):970-982. doi:10.1038/s41593-023-01334-3

149. Yang AC, Vest RT, Kern F, et al. A human brain vascular atlas reveals diverse mediators of Alzheimer's risk. *Nature*. 2022;603(7903):885-892. doi:10.1038/s41586-021-04369-3

150. Fisher RA, Miners JS, Love S. Pathological changes within the cerebral vasculature in Alzheimer's disease: New perspectives. *Brain Pathol*. 2022;32(6):e13061. doi:10.1111/bpa.13061

151. Romay MC, Knutsen RH, Ma F, et al. Age-related loss of Notch3 underlies brain vascular contractility deficiencies, glymphatic dysfunction, and neurodegeneration in mice. *J Clin Invest*. 2024;134(2):e166134. doi:10.1172/JCI166134

152. Venkat P, Chopp M, Zacharek A, et al. White matter damage and glymphatic dysfunction in a model of vascular dementia in rats with no prior vascular pathologies. *Neurobiol Aging*. 2017;50:96-106. doi:10.1016/j.neurobiolaging.2016.11.002

153. Henao-Restrepo J, López-Murillo C, Valderrama-Carmona P, et al. Gliovascular alterations in sporadic and familial Alzheimer's disease: APOE3 Christchurch homozygote glioprotection. *Brain Pathol Zurich Switz*. 2023;33(2):e13119. doi:10.1111/bpa.13119

154. Almeida MC, Eger SJ, He C, et al. Single-nucleus RNA sequencing demonstrates an autosomal dominant Alzheimer's disease profile and possible mechanisms of disease protection. *Neuron*. Published online February 21, 2024:S0896-6273(24)00093-X. doi:10.1016/j.neuron.2024.02.009

155. Inestrosa NC, Varela-Nallar L. Wnt signaling in the nervous system and in Alzheimer's disease. *J Mol Cell Biol*. 2014;6(1):64-74. doi:10.1093/jmcb/mjt051

156. Toral-Rios D, Pichardo-Rojas PS, Alonso-Vanegas M, Campos-Peña V. GSK3β and Tau Protein in Alzheimer's Disease and Epilepsy. *Front Cell Neurosci*. 2020;14:19. doi:10.3389/fncel.2020.00019

157. Martin L, Latypova X, Wilson CM, et al. Tau protein kinases: involvement in Alzheimer's disease. *Ageing Res Rev*. 2013;12(1):289-309. doi:10.1016/j.arr.2012.06.003

158. Wang Y, Mandelkow E. Tau in physiology and pathology. *Nat Rev Neurosci*. 2016;17(1):5-21. doi:10.1038/nrn.2015.1

159. Lu PJ, Wulf G, Zhou XZ, Davies P, Lu KP. The prolyl isomerase Pin1 restores the function of Alzheimer-associated phosphorylated tau protein. *Nature*. 1999;399(6738):784-788. doi:10.1038/21650

160. Hanger DP, Anderton BH, Noble W. Tau phosphorylation: the therapeutic challenge for neurodegenerative disease. *Trends Mol Med*. 2009;15(3):112-119. doi:10.1016/j.molmed.2009.01.003

161. Dujardin S, Commins C, Lathuiliere A, et al. Tau molecular diversity contributes to clinical heterogeneity in Alzheimer's disease. *Nat Med*. 2020;26(8):1256-1263. doi:10.1038/s41591-020-0938-9

162. Bai B, Vanderwall D, Li Y, et al. Proteomic landscape of Alzheimer's Disease: novel insights into pathogenesis and biomarker discovery. *Mol Neurodegener*. 2021;16(1):55. doi:10.1186/s13024-021-00474-z

163. Wu D, Pan W. GSK3: a multifaceted kinase in Wnt signaling. *Trends Biochem Sci*. 2010;35(3):161-168. doi:10.1016/j.tibs.2009.10.002

164. Zhang Z, Hartmann H, Do VM, et al. Destabilization of beta-catenin by mutations in presenilin-1 potentiates neuronal apoptosis. *Nature*. 1998;395(6703):698-702. doi:10.1038/27208

165. Garwood CJ, Pooler AM, Atherton J, Hanger DP, Noble W. Astrocytes are important mediators of Aβ-induced neurotoxicity and tau phosphorylation in primary culture. *Cell Death Dis*. 2011;2(6):e167-e167. doi:10.1038/cddis.2011.50

166. Gama Sosa MA, Gasperi RD, Rocher AB, et al. Age-related vascular pathology in transgenic mice expressing presenilin 1-associated familial Alzheimer's disease mutations. *Am J Pathol*. 2010;176(1):353-368. doi:10.2353/ajpath.2010.090482

167. Kapoor A, Nation DA. Role of Notch signaling in neurovascular aging and Alzheimer's disease. *Semin Cell Dev Biol*. 2021;116:90-97. doi:10.1016/j.semcdb.2020.12.011

Eidesstattliche Versicherung - Declaration on oath

Hiermit erkläre ich an Eides statt, dass ich die vorliegende Dissertationsschrift selbst verfasst und keine anderen als die angegebenen Quellen und Hilfsmittel benutzt habe.

I hereby declare, on oath, that I have written the present dissertation by my own and have not used other than the acknowledged resources and aids.

Hamburg, den 8.5.2024 Unterschrift J. Gise Lifter